



<b>Publication Year</b>	2015
<b>Acceptance in OA</b>	2020-03-24T16:18:30Z
<b>Title</b>	Infrared emission of young HII regions: a Herschel/Hi-GAL study
<b>Authors</b>	CESARONI, Riccardo, Pestalozzi, M., BELTRAN SOROLLA, MARIA TERESA, Hoare, M. G., MOLINARI, Sergio, OLMI, LUCA, Smith, M. D., Stringfellow, G. S., TESTI, Leonardo, Thompson, M. A.
<b>Publisher's version (DOI)</b>	10.1051/0004-6361/201525953
<b>Handle</b>	<a href="http://hdl.handle.net/20.500.12386/23512">http://hdl.handle.net/20.500.12386/23512</a>
<b>Journal</b>	ASTRONOMY & ASTROPHYSICS
<b>Volume</b>	579

## Infrared emission of young HII regions: a *Herschel*/Hi-GAL study<sup>★,★★</sup>

R. Cesaroni<sup>1</sup>, M. Pestalozzi<sup>2</sup>, M. T. Beltrán<sup>1</sup>, M. G. Hoare<sup>3</sup>, S. Molinari<sup>2</sup>, L. Olmi<sup>1,4</sup>, M. D. Smith<sup>5</sup>,  
G. S. Stringfellow<sup>6</sup>, L. Testi<sup>7,1</sup>, and M. A. Thompson<sup>8</sup>

<sup>1</sup> INAF, Osservatorio Astrofisico di Arcetri, Largo E. Fermi 5, 50125 Firenze, Italy  
e-mail: cesa@arcetri.astro.it

<sup>2</sup> INAF, Istituto di Astrofisica e Planetologia Spaziale, via Fosso del Cavaliere 100, 00133 Roma, Italy  
e-mail: sergio.molinari@iaps.inaf.it

<sup>3</sup> School of Physics and Astrophysics, University of Leeds, Leeds LS2 9JT, UK

<sup>4</sup> University of Puerto Rico, Rio Piedras Campus, Physics Dept., Box 23343, UPR station, San Juan, Puerto Rico, USA

<sup>5</sup> Centre for Astrophysics and Planetary Science, University of Kent, Canterbury CT2 7NH, UK

<sup>6</sup> Center for Astrophysics and Space Astronomy, University of Colorado, UCB 389, Boulder, CO 80309, USA

<sup>7</sup> European Southern Observatory, Karl-Schwarzschild-Str. 2, 85748 Garching, Germany

<sup>8</sup> Centre for Astrophysics Research, University of Hertfordshire, College Lane, Hatfield, AL10 9AB, UK

Received 24 February 2015 / Accepted 20 April 2015

### ABSTRACT

**Context.** Investigating the relationship between radio and infrared emission of HII regions may help shed light on the nature of the ionizing stars and the formation mechanism of early-type stars in general.

**Aims.** We have taken advantage of recent unbiased surveys of the Galactic plane such as *Herschel*/Hi-GAL and VLA/CORNISH to study a bona fide sample of young HII regions located in the Galactic longitude range 10°–65° by comparing the mid- and far-IR continuum emission to the radio free-free emission at 5 GHz.

**Methods.** We have identified the Hi-GAL counterparts of 230 CORNISH HII regions and reconstructed the spectral energy distributions of 204 of these by complementing the Hi-GAL fluxes with ancillary data at longer and shorter wavelengths. Using literature data, we obtained a kinematical distance estimate for 200 HII regions with Hi-GAL counterparts and determined their luminosities by integrating the emission of the corresponding spectral energy distributions. We have also estimated the mass of the associated molecular clumps from the (sub)millimeter flux densities.

**Results.** Our main finding is that for ~1/3 of the HII regions the Lyman continuum luminosity appears to be greater than the value expected for a zero-age main-sequence star with the same bolometric luminosity. This result indicates that a considerable fraction of young, embedded early-type stars presents a “Lyman excess” possibly due to UV photons emitted from shocked material infalling onto the star itself and/or a circumstellar disk. Finally, by comparing the bolometric and Lyman continuum luminosities with the mass of the associated clump, we derive a star formation efficiency of 5%.

**Conclusions.** The results obtained suggest that accretion may still be present during the early stages of the evolution of HII regions, with important effects on the production of ionizing photons and thus on the circumstellar environment. More reliable numerical models describing the accretion process onto massive stars are required to shed light on the origin of the observed Lyman excess.

**Key words.** stars: early-type – stars: formation – HII regions

\* *Herschel* is an ESA space observatory with science instruments provided by European-led Principal Investigator consortia and with important participation from NASA. PACS has been developed by a consortium of institutes led by MPE (Germany) and including UVIE (Austria); KUL, CSL, IMEC (Belgium); CEA, OAM P (France); MPIA (Germany); IAPS, OAP/OAT, OAA/CAISMI, LENS, SISSA (Italy); IAC (Spain). This development has been supported by the funding agencies BMVIT (Austria), ESA-PRODEX (Belgium), CEA/CNES (France), DLR (Germany), ASI (Italy), and CICYT/MCYT (Spain). SPIRE has been developed by a consortium of institutes led by Cardiff Univ. (UK) and including Univ. Lethbridge (Canada); NAOC (China); CEA, LAM (France); IAPS, Univ. Padua (Italy); IAC (Spain); Stockholm Observatory (Sweden); Imperial College London, RAL, UCL-MSSL, UKATC, Univ. Sussex (UK); Caltech, JPL, NHSC, Univ. Colorado (USA). This development has been supported by national funding agencies: CSA (Canada); NA OC (China); CEA, CNES, CNRS (France); ASI (Italy); MCINN (Spain); Stockholm Observatory (Sweden); STFC (UK); and NASA (USA).

\*\* Appendix A is available in electronic form at

<http://www.aanda.org>

## 1. Introduction

High-mass stars are characterized by luminosities in excess of  $\sim 10^3 L_{\odot}$  and powerful Lyman continuum emission. The latter is bound to create an ionized region around the star, which is detected through its free-free emission. Such an HII region expands and eventually disperses, although the details of this process and the corresponding time scale are still matters of debate as they also depend on the density distribution and velocity field of the dense gas enshrouding the newly born star. The early evolution of an HII region is closely related to the formation process of an OB-type star, and is hence of great interest for studies of massive star formation. As a matter of fact, HII regions are conventionally classified as hypercompact, ultracompact (UC), compact, and extended, in order of increasing size and, presumably, age. The last class is clearly associated with more evolved objects and possibly multiple OB stars, while sources belonging to the first class are very small and faint, especially below 5 GHz owing to their spectra rising with frequency. This explains why

they are difficult to detect and resolve, even with sensitive radio interferometers (see Kurtz 2005 for a review on hypercompact HII regions). Consequently, much attention has been devoted to UC and compact HII regions.

One of the problems in the study of HII regions is stellar multiplicity. The ideal template of a single star ionizing a spherical HII region is inadequate to describe the real world where massive stars form in rich stellar clusters. A viable way to shed light on this issue is to compare the radio luminosity to the bolometric luminosity of these objects. The former is sensitive only to the most massive star(s), whereas all cluster members contribute to the latter. However, a problem with measuring the bolometric luminosity is that the major contribution comes from reprocessed radiation from dust emitted at far-IR wavelengths, heavily absorbed by the Earth’s atmosphere and thus impossible to observe from the ground. Moreover, the comparison between radio and far-IR emission was hindered by the dramatic difference in angular resolution between surveys conducted in the two wavelength regimes. While radio interferometers have been able to attain subarcsecond resolutions for many decades, until recently the best data available for a large number of HII regions at  $\sim 100 \mu\text{m}$  were those of the IRAS mission with an angular resolution of only  $\sim 2'$ . As a consequence, the luminosity measurements based mostly on IRAS data were to be taken as upper limits, as unrelated objects falling in the large beam could contribute to the estimate.

This situation has now dramatically changed and pioneering studies such as that by Wood & Churchwell (1989) can be significantly improved on. On one hand, the ESA *Herschel* Space Observatory (Pilbratt et al. 2010) provides us with a tool to improve the angular resolution in the far-IR by a factor of  $\sim 10$  with respect to IRAS. On the other hand, the completion of the CORNISH survey (Hoare et al. 2012; Purcell et al. 2013) of a large portion of the Galactic plane at 5 GHz with  $\sim 1''.5$  resolution has made it possible to obtain an unbiased census of UC and compact HII regions. These radio maps are perfectly complementary to the far-IR images obtained in the context of the Hi-GAL project (Molinari et al. 2010), which covers a stripe  $2^\circ$  wide in latitude and  $360^\circ$  in longitude, following the warp of the Galactic plane, at five far-IR continuum bands. We thus decided to take advantage of the Hi-GAL and CORNISH databases to perform a systematic study of the radio and IR emission of young HII regions located in the Galactic longitude range  $10^\circ$ – $65^\circ$ .

The present article is organized as follows. In Sects. 2 and 3.1 we describe the sample of HII regions selected from the CORNISH catalogue and illustrate the method adopted to identify the corresponding Hi-GAL counterparts. In Sects. 3.2 to 3.4 source parameters such as the distance, luminosity, and mass are estimated, while in Sect. 4 we discuss the main results obtained. Finally, in Sect. 5 the conclusions are drawn.

## 2. The sample

Since the main scope of our study is to investigate the IR and radio properties of young massive stars, we have selected the sources classified as “ultracompact” and “compact” HII regions in the CORNISH catalogue. This a classification was obtained after visual inspection also using the *Spitzer* IRAC and MIPS GAL images (more details on the method are given in Purcell et al. 2013 and will not be repeated here). Since the distinction between these two types was based on the angular size and as such does not necessarily mirror an intrinsic physical and

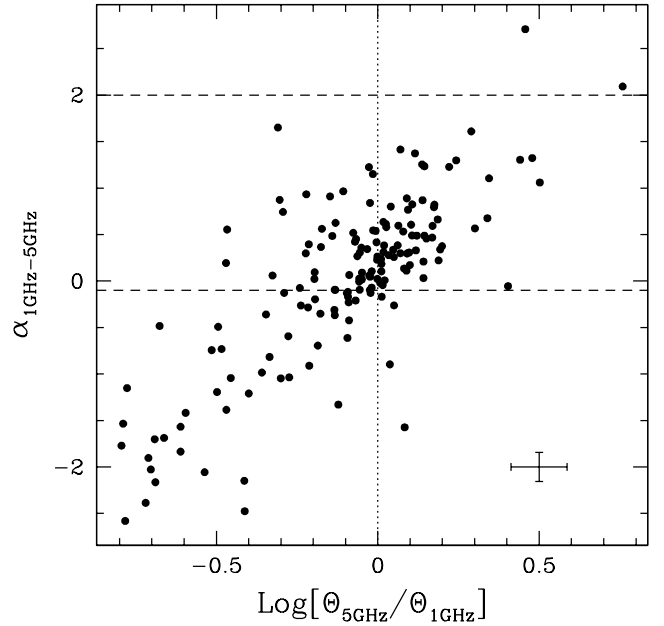


**Fig. 1.** Spectral index between 1.4 GHz and 5 GHz of our sample of HII regions versus the ratio between the corresponding angular sizes. The horizontal dashed lines bracket the range of spectral indices expected for free-free continuum emission, while the dotted vertical line corresponds to equal angular sizes at the two frequencies. The cross in the *bottom right* indicates the typical error bars assuming an uncertainty of 10% at both frequencies, for both the flux density and the size.

evolutionary difference, for the sake of simplicity in the following we will refer to all of our sources simply as “HII regions”.

Our sample consists of 281 bona fide HII regions. In order to further characterize them, we searched for possible counterparts at 1.4 GHz in the MAGPIS survey by White et al. (2005), whose angular resolution is  $\sim 6''$ . Although this resolution is  $\sim 4$  times worse than the resolution of the CORNISH survey ( $\sim 1''.5$ ), a comparison between the two surveys is feasible. For this purpose we selected the closest MAGPIS source within a conservative circle with  $20''$  radius, taking into account that 99% of the HII regions in the CORNISH catalogue have sizes below this value. We find 170 targets detected at both frequencies. In Fig. 1, we plot the spectral index (defined as  $\alpha = \log_{10}(S_{5\text{GHz}}/S_{1.4\text{GHz}})/\log_{10}(5/1.4)$ ) as a function of the ratio between the angular diameters,  $\Theta$ , at the two frequencies. Although most HII regions have a spectral index between  $-0.1$  and  $+2$ , as expected for free-free emission,  $\sim 1/4$  of the objects have  $\alpha < -0.1$ , which appears inconsistent with thermal emission. However, one sees that basically all of these points have a size ratio below unity and it is therefore very likely that the steep negative spectral index is the result of part of the flux at the highest frequency being filtered out by the interferometer. We conclude that the comparison between the 5 GHz and 1.4 GHz continuum confirms the nature of our HII region sample.

## 3. Analysis

### 3.1. IR and (sub)mm counterparts of the HII regions

Our first goal is to identify the IR counterparts of the HII regions in the Hi-GAL images at five different bands (70, 160, 250, 350, and  $500 \mu\text{m}$ ). The angular resolution of *Herschel* ( $\geq 9''$ ) does not permit us to resolve some of the CORNISH HII regions that lie too close to each other. We thus decided to consider as distinct

**Table 1.** Steps of the source selection process.

CORNISH HIIs		HIIs separation <11''5		With Hi-GAL counterparts		Hi-GAL counterparts with $\geq 3$ fluxes		CORNISH-HiGAL <11''5		With distance estimate
281	→	244	→	230	→	217	→	204	→	200

objects only those targets whose separation from any other target is greater than the *Herschel* half-power beam width (HPBW) at  $160 \mu\text{m}$  (i.e.,  $>11''5$ ). The HII regions below this limit were artificially merged into a single target whose flux density is the sum of the individual flux densities and whose size is the largest of the sizes. In this way, we reduced the sample to 244 objects. For each of these, we searched for compact IR emission in the five Hi-GAL images, inside a circle of  $15''$  radius, centered on the HII region itself. To identify the IR source(s) and measure their flux densities, we used the CuTE<sub>x</sub> algorithm described in Molinari et al. (2011). This may result in multiple counterparts and we decided to choose the closest of these that is detected in the largest number of Hi-GAL bands. In the few cases where the emission was saturated, the flagged pixels were assigned the maximum flux of the closest pixels to the saturated region. Consequently, the corresponding luminosity is to be taken as a lower limit. However, one must keep in mind that saturation usually occurs at  $250 \mu\text{m}$  or  $350 \mu\text{m}$ , while the peak of the continuum emission lies at  $70 \mu\text{m}$  (see Sect. 3.1), which implies that saturation should not affect our luminosity estimates significantly.

With the previous method we were able to identify 230 Hi-GAL counterparts out of 244 targets. In practice, in order to obtain a reliable estimate of the luminosity, from our analysis we excluded all sources that were detected in less than three Hi-GAL bands. This reduces the usable targets to 217. Finally, we rejected all counterparts whose separation from the CORNISH HII region was  $>11''5$  (the *Herschel* HPBW at  $160 \mu\text{m}$  – see above). The final number of targets with a Hi-GAL counterpart is 204. The corresponding Hi-GAL images are shown in Figs. A.2–A.5 where we split the sources into four groups depending on their Lyman continuum properties (as discussed in Sect. 4.1), and in Fig. A.6 where we show the four sources without distance estimates (see Sect. 3.2). The selection process is summarized in Table 1.

Since HII regions are known to be prominent mid-IR emitters, we also included the MSX (Price et al. 1999)  $21 \mu\text{m}$  and WISE (Wright et al. 2010)  $22 \mu\text{m}$  fluxes from the corresponding point-source catalogues, which will provide us with better sampled spectral energy distributions (SEDs) and thus more reliable luminosity estimates. We note that the MSX and WISE fluxes were obtained by summing the fluxes of all the point sources falling inside the full width at half power of the Hi-GAL  $250 \mu\text{m}$  source. We decided not to consider the MIPS GAL  $24 \mu\text{m}$  fluxes because in most of our objects these happen to be heavily saturated. For the sake of completeness, we also included the ATLASGAL<sup>1</sup> (Schuller et al. 2009; Contreras et al. 2013)  $870 \mu\text{m}$  and BGPS v2 (Ginsburg et al. 2013)  $1.1 \text{ mm}$  fluxes. The resulting SEDs from  $21 \mu\text{m}$  to  $1.1 \text{ mm}$  are shown in Fig. A.1. In Table A.1 we give the names and positions of the CORNISH HII regions, the corresponding integrated flux density at  $5 \text{ GHz}$  ( $S_{5 \text{ GHz}}$ ) from the CORNISH catalogue, the

coordinates of the Hi-GAL counterpart, and the values of the flux densities from  $21 \mu\text{m}$  to  $1.1 \text{ mm}$ .

While a limited number of the SEDs may look questionable, possibly owing to faint emission and/or confusion with nearby sources, most of them appear very reasonable. In the following the SEDs will be used to obtain an estimate of both the source luminosity and mass of the associated molecular clump.

### 3.2. Distance estimates

A crucial parameter for our purposes is the source distance. A kinematic distance estimate can be obtained if a velocity measurement is available. Since the Hi-GAL data convey information only on the continuum emission, we investigated the literature to search for molecular or recombination line observations of the 204 usable targets. In particular, we refer to the following articles: Urquhart et al. (2013b; hereafter URQ13), Anderson et al. (2009, 2012), Beuther et al. (2002), Shirley et al. (2013), Bronfman et al. (1996), Jones et al. (2012), Kolpak et al. (2003), Pandian et al. (2008), Sewilo et al. (2004), Watson et al. (2003), Wienen et al. (2012), and the red MSX source (RMS) database<sup>2</sup> (Lumsden et al. 2013). We were able to assign an LSR velocity to all but four (G011.9786-00.0973, G026.0083+00.1369, G026.8304-00.2067, and G065.2462+00.3505) of the 204 sources.

The kinematic distance was computed for our final sample of 200 objects using the Galaxy rotation curve by Brand & Blitz (1993), which resulted in 17 cases without kinematic distance ambiguity (KDA), 172 with KDA, and 11 with velocity inconsistent with the assumed rotation curve. In the last case we assumed the distance to the tangent point. Only for source G10.62–0.38 did we replace our estimate with  $4.2 \text{ kpc}$  (Urquhart, pers. comm.). To solve the KDA we searched the literature for studies where different methods were employed to discriminate the near from the far distance, and we eventually used the following references: URQ13, Anderson & Bania (2009), Anderson et al. (2012), Jones & Dickey (2012), Kolpak et al. (2003), Pandian et al. (2008), Sewilo et al. (2004), and Watson et al. (2003). In this way, we assigned the near distance to 50 targets and the far to 107, while four targets were close to the tangent point. We note that the larger number of sources at the far distance is not surprising as the area of the Galactic plane sampled by CORNISH beyond the tangent point is  $>3.4$  times that inside the tangent point<sup>3</sup>. For the remaining 11 targets we were unable to solve the KDA and we decided to adopt the far distance. This is a conservative approach that will be justified in Sect. 4.1; in all cases, an incorrect choice for these 11 objects is bound to have negligible effects on the results obtained in the present study. The distance estimates are given in Table A.2.

<sup>2</sup> [http://rms.leeds.ac.uk/cgi-bin/public/RMS\\_DATABASE.cgi](http://rms.leeds.ac.uk/cgi-bin/public/RMS_DATABASE.cgi)

<sup>3</sup> This estimate assumes that the maximum distance at which an HII region can be detected by CORNISH is  $>14 \text{ kpc}$ , a reasonable assumption for optically thin HII regions associated with stars earlier than B0.5.

<sup>1</sup> The ATLASGAL project is a collaboration between the Max-Planck-Gesellschaft, the European Southern Observatory (ESO), and the Universidad de Chile.

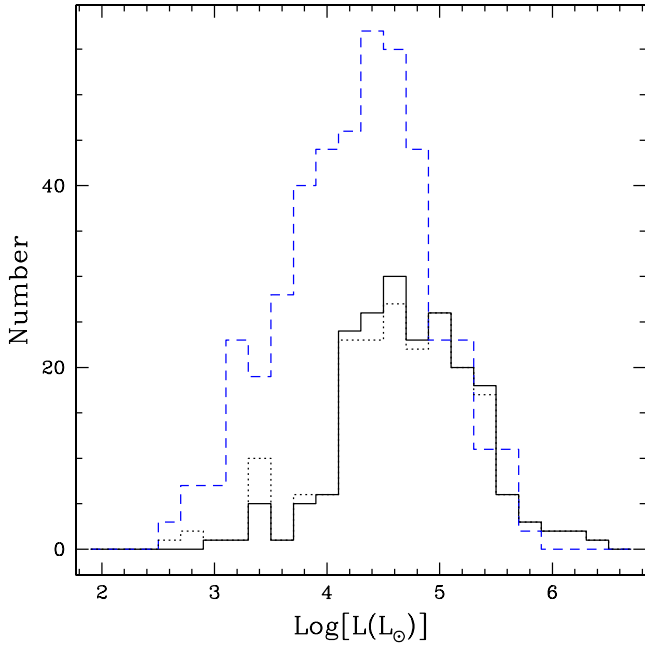


**Fig. 2.** Distribution of the luminosities of CORNISH HII regions. The solid and dotted histograms are obtained by choosing, respectively, the far and near distances for the 11 targets for which the KDA could not be solved. For the sake of comparison, the distribution of the HII regions from the rms survey taken from Fig. 1 in Mottram et al. (2011) is also shown (blue dashed histogram).

### 3.3. Luminosity estimates

The simplest way to obtain an estimate of the luminosity of our sources is to integrate the corresponding continuum spectra by linearly interpolating between the fluxes of the SEDs in Fig. A.1. We prefer this approach to fitting a modified black-body because the SED of HII regions is known to be made of at least two components, a relatively cold one peaking in the far-IR and a hot one peaking at shorter wavelengths. Therefore, a single fit from  $21 \mu\text{m}$  to  $1.1 \text{ mm}$  is unlikely to give reliable results. More complex models such as the one developed by Robitaille et al. (2007) can provide us with satisfactory fits, but the results may significantly depend on the source geometry and orientation, which are difficult to establish. For example, the correction to the luminosity due to the flash-light effect may be important in these models, but it is unclear whether such an effect is indeed at work in our sources.

We obtained the value of the luminosity (listed in Table A.2) for all of the 200 sources with a distance estimate. In Fig. 2 the distribution of these luminosities is shown. The dotted histogram shows how the distribution would change if we chose the near distance for the 11 sources for which the KDA could not be solved (our choice is the far distance, see above). Clearly the near/far ambiguity has little impact on the global sample. One can conclude that most of our objects are characterized by luminosities above  $10^4 L_{\odot}$ , with a handful of sources as weak as  $\geq 10^3 L_{\odot}$ . This finding is in good agreement with the nature of our sample consisting of stars earlier than B3. In the same figure we also plot the luminosity distribution obtained by Mottram et al. (2011; see their Fig. 1) for the rms sample. This distribution appears to be consistent with our sources at high luminosities, while the rms HII regions outnumber our CORNISH sample at lower luminosities. This is likely due to the CORNISH survey being less sensitive than the radio data acquired for the rms

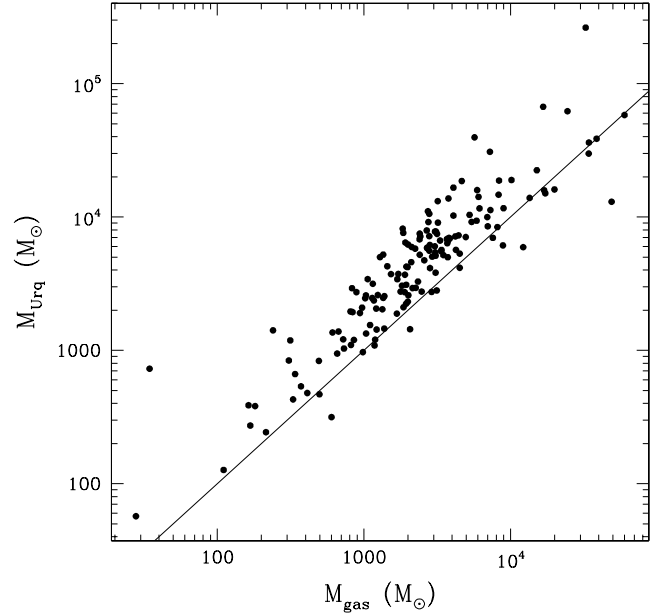


**Fig. 3.** Comparison between our estimate and that of URQ13 of the clump masses associated with CORNISH HII regions. The straight line corresponds to  $M_{\text{Urq}} = M_{\text{gas}}$ .

sample, part of which has been observed at 8.6 GHz, and is thus more complete.

### 3.4. Mass estimates

It is also interesting to estimate the mass of the parental clump where the HII region is embedded. For this purpose, we use the flux density at  $500 \mu\text{m}$  or, if this is not detected, at the longest available wavelength. In practice, the  $500 \mu\text{m}$  flux was used in 92% (188 out of 204) of the cases. Following URQ13, whose sample is very similar to ours, we assumed the same temperature of 20 K for all of the objects. We prefer this choice rather than deriving a temperature estimate from the SED for two reasons: we believe that the temperature obtained from the ammonia data (see URQ13) is more reliable than a value estimated from a model-dependent fit to the SED, and because the variation of temperature across the sample of URQ13 is quite limited, with most values in the range 15–30 K, which implies a maximum uncertainty of  $\sim 50\%$  on our mass estimates. The dust absorption coefficient at  $500 \mu\text{m}$  ( $5 \text{ cm}^2 \text{ g}^{-1}$ ) was taken from Col. 6 of Table 1 in Ossenkopf & Henning (1994). The dust absorption coefficient was assumed to vary as  $\nu^{1.9}$ , obtained by fitting the values quoted in the same table. The derived masses are given in Table A.2.

Figure 3 shows a comparison between our mass estimates and those by URQ13, for the 158 sources in common between the two studies. We note that, for the sake of consistency, URQ13’s masses were scaled to our distances when necessary. While the two masses appear quite consistent, the estimate of URQ13 is systematically greater (on average by a factor 1.7) than ours. This is due to the way the sub-mm flux density has been computed: in our case, the CuTEX algorithm basically performs a Gaussian fit to the image, whereas URQ13 integrated the flux inside a suitable polygon. It is clear that the latter method is bound to measure more flux than the former as it also takes into account extended emission lying above the wings of the Gaussian fit. While any choice has its shortcomings, in our

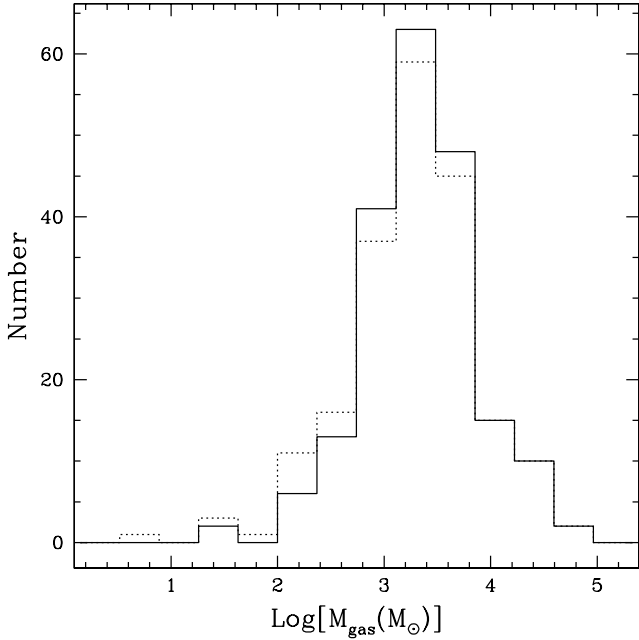


**Fig. 4.** Distribution of the clump mass associated with CORNISH HII regions. The solid and dotted histograms are obtained by choosing, respectively, the far and near distances for the 11 targets for which the KDA could not be solved.

approach we have arbitrarily decided to consider the compact emission because we believe it to be more tightly related to the embedded HII region.

The distribution of the clump masses, shown in Fig. 4, demonstrates that the vast majority of the clumps are above several  $100 M_{\odot}$ , as expected for high-mass star forming regions. It is thus very likely that our measurements refer to rich stellar clusters, tightly associated with the early-type stars ionizing the CORNISH HII regions.

## 4. Discussion

### 4.1. Lyman continuum excess

The large luminosities and masses of the objects under study are strongly suggestive of the presence of multiple stars. In order to establish the contribution of low-mass stars and investigate the properties of the early-type stars, we have estimated their Lyman continuum emission,  $N_{\text{Ly}}$ , assuming the free-free emission to be optically thin. We used the expression

$$N_{\text{Ly}}(\text{s}^{-1}) = 9.9 \times 10^{43} S_{5 \text{ GHz}}(\text{mJy}) d^2(\text{kpc}), \quad (1)$$

where  $S_{5 \text{ GHz}}$  is the integrated flux density at 5 GHz,  $d$  is the source distance, and the electron temperature has been taken equal to 8000 K (a mean value for Galactic HII regions; see, e.g., Quireza et al. 2006). In Fig. 5 we compare  $N_{\text{Ly}}$  to the bolometric luminosity,  $L$ , of the 200 HII regions for which a distance estimate was possible. When considering this plot, one should keep in mind that the Lyman continuum fluxes might be underestimated for three reasons: (i) the free-free emission could be optically thick; (ii) part of the ionizing photons could be absorbed by dust inside the HII region or leaking out of it; or (iii) the radio emission could be partly resolved out by the interferometer. The last problem indeed seems to occur for a limited number of cases, as discussed in Sect. 2, while the other two are difficult to quantify. Therefore, a conservative approach is to consider the values of  $N_{\text{Ly}}$  as lower limits.

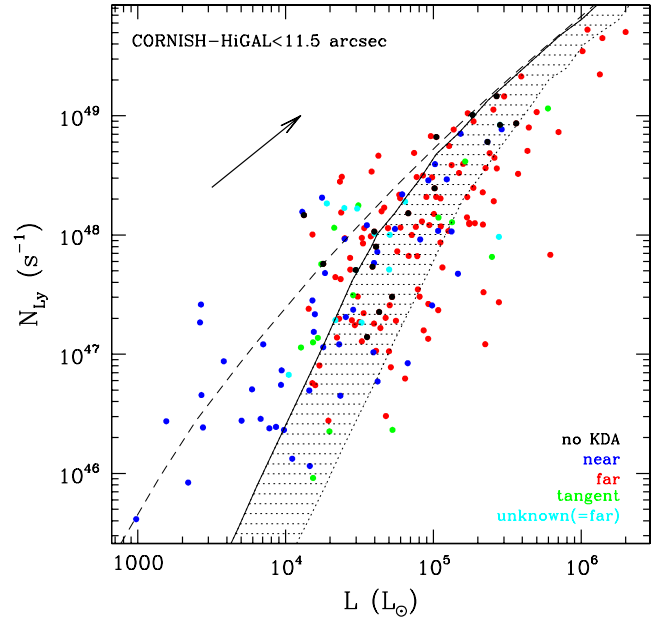


**Fig. 5.** Lyman continuum of the selected sample of CORNISH HII regions versus the corresponding bolometric luminosity obtained from the Hi-GAL data. The color of the symbols indicates the choice of the kinematic distance: blue for near, red for far, green for tangent point, cyan for unknown (in this case the far distance was assumed), and black for no KDA. The arrow indicates how much a point would move if its distance is increased by a factor of 2. The solid curve corresponds to the  $N_{\text{Ly}}-L$  relationship for a ZAMS star, while the hatched area is where 90% of the simulated stellar clusters should lie. We note the large number of sources in the forbidden region above the solid curve. The dashed curve is the  $N_{\text{Ly}}$  that a star would emit if it were a perfect blackbody.

For the sake of comparison, in the figure we also plot the expected relationship between  $N_{\text{Ly}}$  and  $L$  for a single zero-age main-sequence (ZAMS) star (solid curve) as well as the Lyman continuum emission of a blackbody with the same radius and effective temperature as the ZAMS star (dashed curve). The properties of ZAMS stars have been obtained from Panagia (1973), Thompson (1984), Smith et al. (2002), and Martins et al. (2005). The solid curve is to be seen as an upper limit to the number of Lyman continuum photons per unit time that can be emitted by a ZAMS star of a given luminosity. As previously mentioned, it is very likely that the regions we studied are associated with stellar clusters rather than single early-type stars. In this case, the expected  $N_{\text{Ly}}$  must be less than that of a single star with the same luminosity and the hatched area in Fig. 5 is where 90% of the clusters should fall. This has been obtained by simulating a large number of clusters, up to a maximum stellar mass of  $120 M_{\odot}$ , adopting the initial mass function of Kroupa et al. (2009), as explained in Sánchez-Monge et al. (2013).

Although many sources (44.5%) lie in the cluster area, a significant fraction falls below (22%) and above it (33.5%). To some extent, a deficit in  $N_{\text{Ly}}$  is not surprising because of the various effects that may lead to its underestimation (see above). In addition, the sources that most suffer from such a deficit have been assigned the far kinematic distance; if this is replaced by the near distance, the corresponding points below the hatched region move toward the bottom left, parallel to the arrow in the figure, thus approaching the hatched area. A more physical explanation might be that the stars ionizing the HII regions are larger and cooler than on the ZAMS, possibly because of residual accretion onto the stellar surface (see Hosokawa & Omukai 2009),

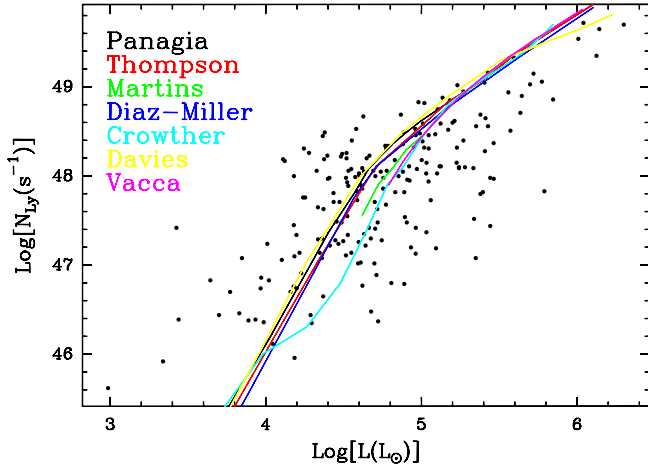


**Fig. 6.** Same as Fig. 5, where the relationships between  $N_{\text{Ly}}$  and  $L$  for a single ZAMS star obtained by various authors (Panagia 1973; Thompson 1984; Martins et al. 2005; Diaz-Miller et al. 1998; Davies et al. 2011; Vacca et al. 1996; Crowther 2005) are plotted. Clearly, in all cases the number of sources lying in the forbidden region above these curves is large.

which implies a significant decrease of the Lyman continuum photon rate. Finally, it is also possible that we are dealing with clusters overabundant in low-mass stars, which would cause a smaller  $N_{\text{Ly}}/L$  ratio than for a normal cluster.

To find an explanation for the 67 objects falling above the cluster region, is instead non-trivial (see the discussion by Sánchez-Monge et al. 2013). In the following we will refer to the region above the solid curve in Fig. 5 as the “forbidden” region. We note that we have adopted the far distance for the sources for which the KDA could not be solved; this is a conservative choice, because assuming the near distance for these objects would increase the number of points falling in the forbidden region from 67 to 72. For the other points, mistaking the near with the far distance may indeed move some of them away from the forbidden region, but even assuming the far distance for *all* of the sources, only 17 out of 67 points would move to the right of the solid line in the figure. Moreover, one cannot appeal to an overestimate of the Lyman continuum flux, as previously explained. We have also verified the reliability of the  $N_{\text{Ly}}-L$  relationship that we adopted. For this purpose, we plot in Fig. 6 the same relationship based on the results of various studies available in the literature. As one can see, none of the  $N_{\text{Ly}}-L$  curves is consistent with all the points in the plot and some of them make the problem even worse.

Since it appears unlikely that we have overestimated the Lyman continuum flux, one may wonder whether we have underestimated the bolometric luminosity. An increase in  $L$  by a factor of 8 or less, would move all the points to the right out of the forbidden region. To test this possibility, we have recomputed the bolometric luminosity using the flux densities of the IRAS Point Source Catalogue counterparts of our sources. These counterparts have been selected by choosing the closest IRAS point source (if any) within  $60''$  from the HII region. Given the large IRAS HPBW at  $100\ \mu\text{m}$  ( $2'$ ), the corresponding luminosity estimate is to be considered a conservative upper limit. However, ten sources still lie in the forbidden region, as demonstrated by Fig. 7. It is also worth noting that the number of points below the cluster region has dramatically increased with respect to Fig. 5, consistent with the idea that IRAS-based luminosities

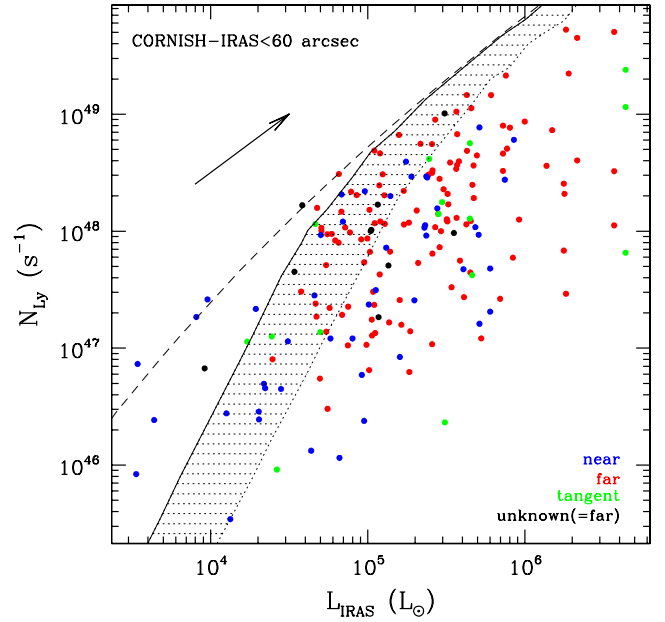


**Fig. 7.** Analogous to Fig. 5, where the bolometric luminosity computed from the Hi-GAL data has been replaced by that estimated from the IRAS fluxes.

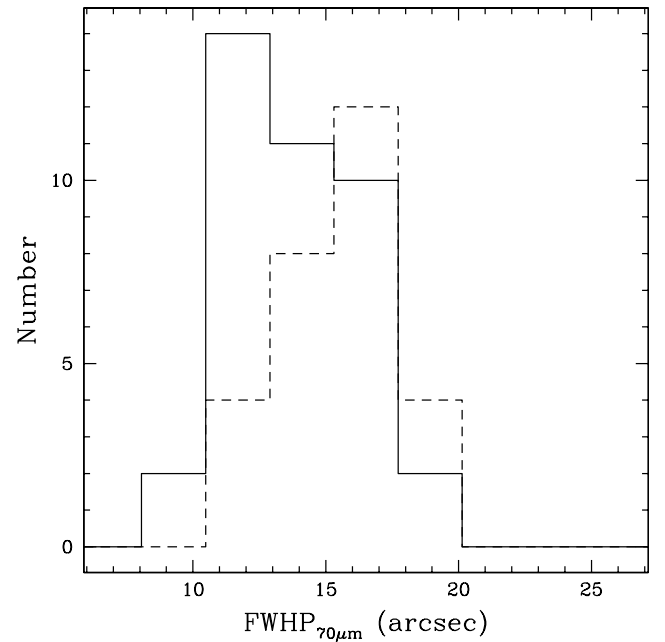


**Fig. 8.** Distributions of the angular size (FWHP) at  $70\ \mu\text{m}$  for sources in the forbidden region of Fig. 5, lying above (dashed histogram) and below (solid) the blackbody curve.

are by far too large. For these reasons, we consider Fig. 5 more reliable and will discuss this in the following.

Of course, we cannot rule out the possibility that a few objects in the forbidden zone are affected by an inappropriate estimate of  $L$ . In particular, some of the sources above the blackbody curve appear too extreme not to be misplaced. In Fig. 8 we compare the full width at half power (FWHP) at  $70\ \mu\text{m}$  of these sources with that of the other objects in the forbidden region lying below the blackbody curve. Clearly, the former are more extended than the latter and this could make it more difficult to estimate their integrated flux with CuTex (see Sect. 3.1), which

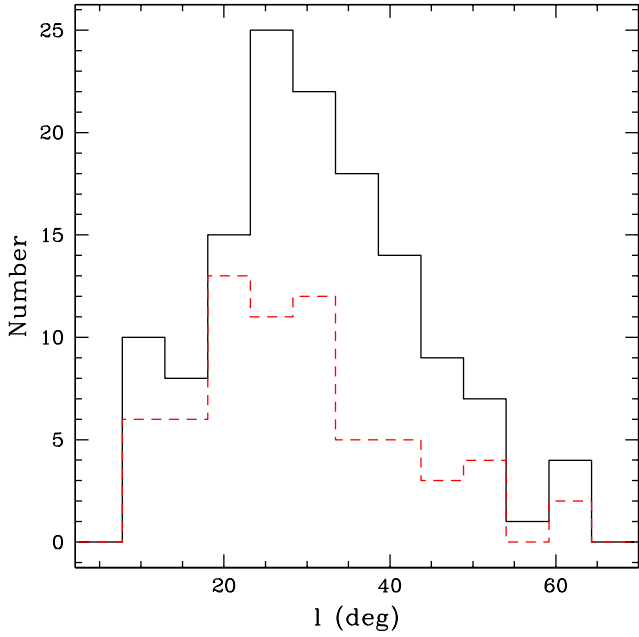


**Fig. 9.** Distributions of the Galactic longitude for sources with Lyman excess (dashed histogram, numbers on right axis) and without (solid histogram, numbers on left axis).

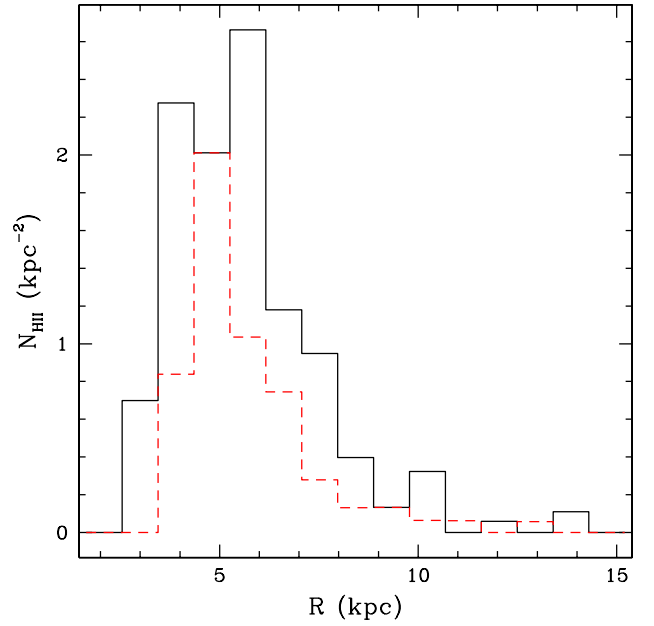


**Fig. 10.** Number of HII regions per unit surface as a function of Galactocentric distance for sources with Lyman excess (dashed histogram, numbers on right axis) and without (solid histogram, numbers on left axis).

was conceived to identify compact sources. Consequently, it is plausible that the luminosity might have been underestimated for some of these sources.

In conclusion, we believe that Fig. 5 proves that the CORNISH sample of HII regions contains a number of objects that really produce many more Lyman continuum photons than those emitted by a ZAMS star with the same bolometric luminosity. In the following, we will refer to this phenomenon as “Lyman excess”.

In Figs. 9 and 10, we compare the distributions in Galactic longitude and Galactocentric distance of the HII regions with Lyman excess to those of sources without Lyman excess. No significant difference can be seen between the two types in Fig. 9, while Fig. 10 seems to suggest that Lyman-excess sources are perhaps more concentrated in the 5 kpc ring than the others, although the difference is only marginally significant.

#### 4.2. Nature of the Lyman-excess sources

The existence of HII regions with an excess of Lyman continuum emission was noted by Sánchez-Monge et al. (2013) and confirmed by Lumsden et al. (2013) and URQ13. These results, however, were obtained from low-resolution radio images and/or luminosity estimates based on IRAS data, whose limitations have already been discussed. Even when the 70  $\mu\text{m}$  MIPS GAL fluxes were available, the angular resolution was still a factor of  $\sim 2$  lower than in the *Herschel* images. The availability of the Hi-GAL and CORNISH unbiased surveys permits a more complete and systematic reconstruction of the SED of the HII regions at far-IR wavelengths, which is crucial for an accurate estimate of the luminosity.

An important step towards a better understanding of the Lyman excess is to discover the nature of the sources with this peculiarity. In Fig. 11 we compare the distribution of  $L/M_{\text{gas}}$  of the Lyman-excess sources with that of the others. This comparison suggests that the Lyman-excess sources are less luminous

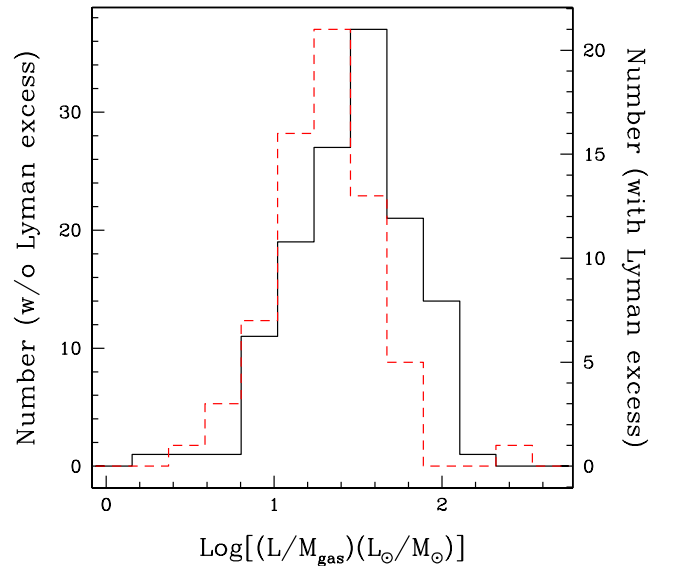


**Fig. 11.** Distributions of the luminosity-to-mass ratio for sources with Lyman excess (dashed histogram, numbers on right axis) and without (solid histogram, numbers on left axis).

than the rest of the sample for the same mass of the associated clumps. The Kolmogorov-Smirnov (hereafter K-S) statistical test gives a null probability ( $7.4 \times 10^{-5}$ ) that the two subsamples in the figure have the same distribution, confirming the existence of a substantial difference between them. A possible interpretation is that the Lyman-excess sources are on average more deeply embedded and younger. Alternatively, the clumps might contain less massive stars, which – for the same star formation efficiency – would produce less luminosity. However, the second explanation seems inconsistent with the fact that the Lyman-excess sources are also those with the largest  $N_{\text{Ly}}/L$  ratio, as shown in Fig. 12, where according to the K-S test the

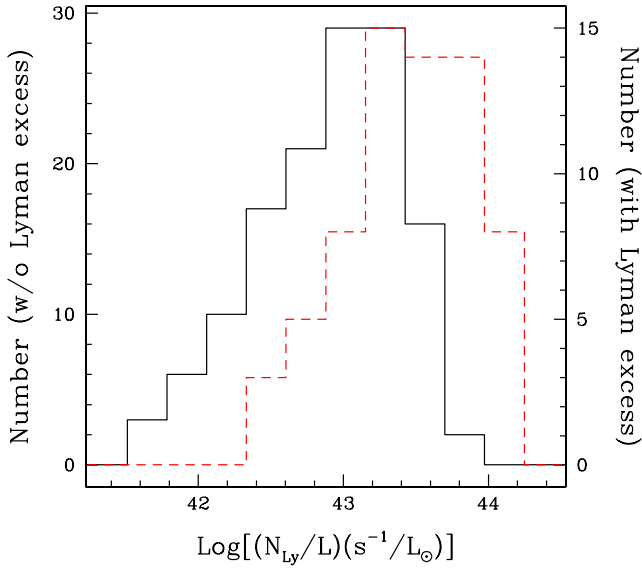


**Fig. 12.** Distributions of the ratio between Lyman continuum flux and bolometric luminosity for sources with Lyman excess (dashed histogram, numbers on right axis) and without (solid histogram, numbers on left axis).

probability that the two distributions are equivalent is basically zero ( $1.1 \times 10^{-8}$ ).

The possibility that these peculiar objects could be in an early, embedded evolutionary phase is also supported by other findings. In Fig. 13 we plot the  $[250-70]$  color<sup>4</sup> versus a quantity representing the amount of Lyman excess. The latter is defined by the expression

$$\Delta_{\text{ex}} = \Delta(\log_{10} N_{\text{Ly}}) \frac{|\Delta(\log_{10} L)|}{\sqrt{[\Delta(\log_{10} N_{\text{Ly}})]^2 + [\Delta(\log_{10} L)]^2}}, \quad (2)$$

where  $\Delta(\log_{10} N_{\text{Ly}})$  and  $\Delta(\log_{10} L)$  are, respectively, the separations measured along the  $\log_{10} N_{\text{Ly}}$  and  $\log_{10} L$  axes between a given point in Fig. 5 and the solid curve delimiting the forbidden region. In practice this expression gives the approximate distance of the point from that curve, assumed negative to the right of the curve.

The line in Fig. 13 is obtained after rebinning the points on a number of intervals and shows some increase with increasing Lyman excess. This means that the Lyman-excess sources may have lower color temperatures than the rest of the sample, consistent with the hypothesis that these sources are younger and more deeply embedded inside cold dusty envelopes. This result is confirmed by the distributions of the color indices of the two samples, with and without Lyman excess (see Fig. 14), which have a probability of  $2.9 \times 10^{-4}$  of being intrinsically identical according to the K-S statistical test. Clearly, the sources with Lyman excess are on average “colder”, in terms of  $[250-70]$ , than those without, in agreement with the finding by Sánchez-Monge et al. (2013) that most of the sources with Lyman excess belong to their “type 2” class, consisting of embedded young massive stars still undergoing accretion.

Based on all of the above, we can speculate that the HII regions with Lyman excess could be ionized by young, mostly B-type stars still undergoing accretion. As discussed by Lumsden et al. (2013), our knowledge of early-type stars is

<sup>4</sup> Defined as the ratio between the  $250 \mu\text{m}$  and  $70 \mu\text{m}$  flux densities:  $[250-70] = \log_{10}(S_{250 \mu\text{m}}/S_{70 \mu\text{m}})$ .

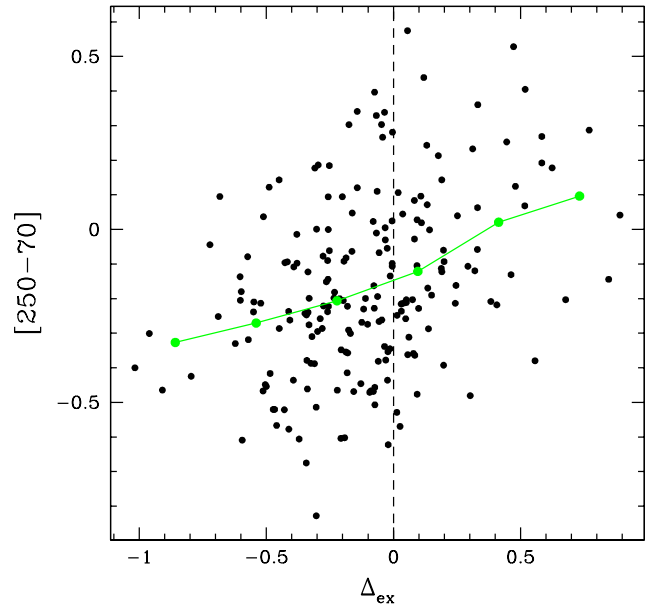


**Fig. 13.** Color index between  $250 \mu\text{m}$  and  $70 \mu\text{m}$  versus the parameter  $\Delta_{\text{ex}}$  measuring the Lyman excess, defined in Eq. (2). The vertical dashed line marks the separation between sources with Lyman excess (i.e., with  $\Delta_{\text{ex}} > 0$ ) and those without. The solid line connects points obtained after rebinning the data.

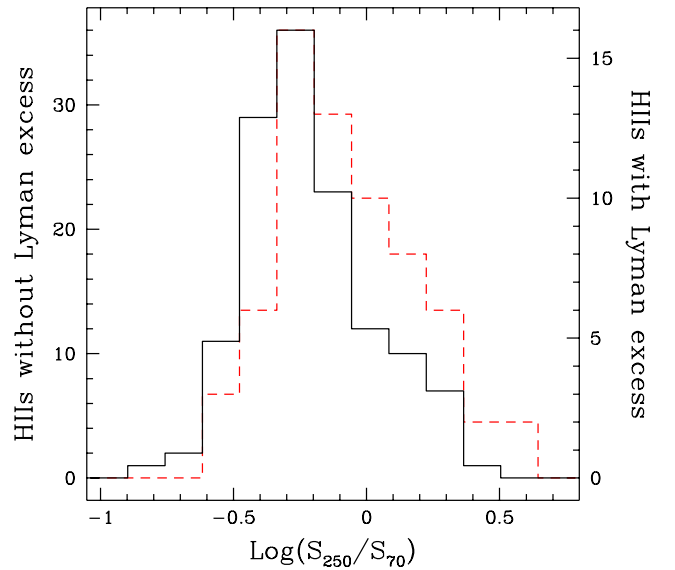


**Fig. 14.** Distribution of the color index between  $250 \mu\text{m}$  and  $70 \mu\text{m}$  for the sources with Lyman excess (dashed histogram, labels on right axis) and without (solid histogram, labels on left axis). We note how the latter is skewed towards lower color indices with respect to the former.

based on visible stars, namely main-sequence stars that have dispersed their parental cocoons, but their properties might significantly differ from those of the young high-mass stars that we are considering in our study. Moreover, one cannot exclude that a significant fraction of the Lyman continuum luminosity could originate from the accretion shock onto a circumstellar disk. Indeed, the model calculations by Hosokawa & Omukai (2009) appear to predict Lyman continuum fluxes comparable to or even greater than those of the star itself (Hosokawa, pers. comm.), possibly sufficient to explain the observed excess.

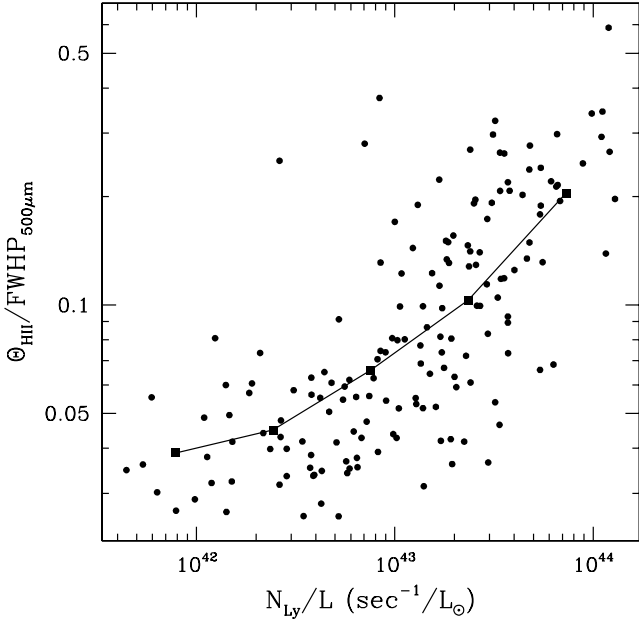


**Fig. 15.** Ratio between the HII region size (from the CORNISH catalogue) and the FWHP at  $500 \mu\text{m}$  of the Hi-GAL counterpart, versus the ratio between the Lyman continuum photon rate and the bolometric luminosity. The solid curve was obtained by rebinning the data points.

Also the model by Smith (2014) provides us with a possible explanation of the Lyman excess. In this model the protostar predominantly accumulates low entropy material via cold accretion, but then accretes onto hot spots covering a small fraction of the protostellar surface. The cold accretion assures that the young star is relatively compact, which generates high free-fall speeds, while the free-fall onto the limited area significantly raises the temperature and hence the Lyman flux. In fact, a comparison between Figs. 15 and 16 of Smith (2014) and our Fig. 5 demonstrates the ability of the model to explain most of the Lyman-excess sources.

More detailed numerical calculations are needed in order to come to a firm conclusion on this issue, since a substantial improvement is necessary to predict the exact amount of Lyman continuum photons emitted in the accretion process.

### 4.3. Star formation efficiency

Our objects are bona fide young HII regions (see Sect. 2), and it is thus reasonable to assume that all sources are in a similar evolutionary phase, with the caveat that those with Lyman-excess might be slightly younger than the others (see Sect. 4.2). That our sample of HII regions spans a small range of ages can be verified by studying the size of the HII region as a function of stellar mass, which should depend on the mass of the star ionizing it. In this case one should find a correlation between HII region size and stellar mass. If, instead, the HII regions are in different evolutionary stages, no correlation should be found because the size of the HII region would depend not only on the stellar mass but also on the phase of expansion. In Fig. 15, we plot the ratio between the angular size of the HII region ( $\Theta_{\text{HII}}$ , provided by the CORNISH catalogue; see Purcell et al. 2013) and the FWHP at  $500 \mu\text{m}$  of the Hi-GAL counterpart as a function of the ratio  $N_{\text{Ly}}/L$ . We prefer to use ratios to get rid of any error related to the distance estimates. The ratio  $N_{\text{Ly}}/L$  increases with stellar mass, while  $\Theta_{\text{HII}}/\text{FWHP}_{500 \mu\text{m}}$  basically depends only on  $\Theta_{\text{HII}}$  because the clump radius is only weakly dependent on the clump

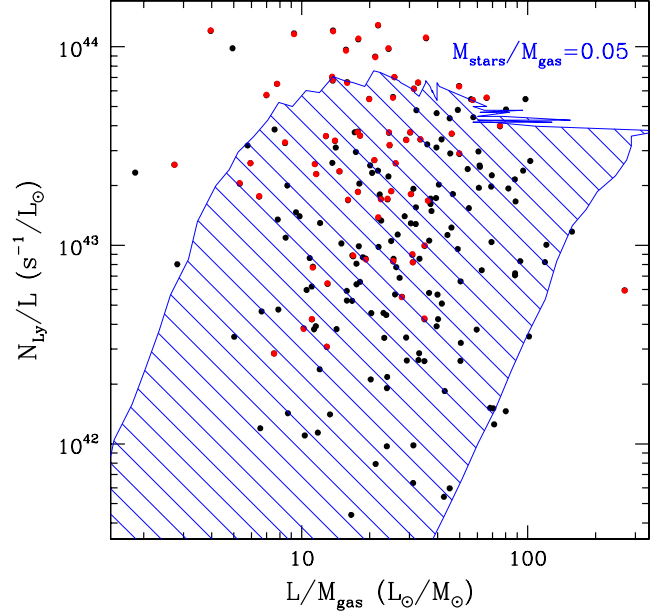


**Fig. 16.** Ratio between the Lyman continuum photon rate and the bolometric luminosity, versus the ratio between the luminosity and the clump mass for the CORNISH HII regions. The red points indicate simulated sources with Lyman excess. The hatched area contains 90% of the simulated clusters assuming a star formation efficiency of 5%.

mass. Figure 15 shows a correlation between the two quantities (Spearman correlation coefficient 0.72), although with some spread, and confirms that all the regions are roughly coeval.

If our sample is indeed homogeneous, the observed distributions of mass, luminosity, and Lyman continuum emission should mirror the variation of the stellar cluster characteristics rather than a large spread in age. This can be verified by studying the ratios  $L/M_{\text{gas}}$  and  $N_{\text{Ly}}/L$ . Both should increase with time during the process of high-mass star formation because stars gain mass to the detriment of the surrounding envelope and thus increase their luminosities and Lyman continuum fluxes. Consequently, if our sources spanned a large age interval, one should observe a correlation between  $N_{\text{Ly}}/L$  and  $L/M_{\text{gas}}$ .

In Fig. 16 we plot these two ratios against each other for all of the 204 objects of our sample. We note that we have also included the four sources without  $V_{\text{LSR}}$  information because the  $L/M_{\text{gas}}$  and  $N_{\text{Ly}}/L$  do not depend on the distance. This feature makes the plot totally unaffected by the error on the distance. One does not see any significant correlation, consistent with the homogeneity of the sample. This allows us to obtain an estimate of the star formation efficiency. Using the same cluster simulations as in Sect. 4.1, we show in Fig. 16 the area over which 90% of the clusters should distribute, under the assumption that only 5% of the clump mass is converted into stars. The match between this region and the data points is very satisfactory, with the only exception being a handful of sources with the highest values of  $N_{\text{Ly}}/L$ . In the light of Sect. 4.1, this anomaly is not surprising, since these objects are the HII regions with the most prominent Lyman excess.

We note that a star formation efficiency of  $\sim 5\%$  is in reasonable agreement with the value of 10% found by URQ13 for the same type of objects. These authors compared the clump mass with the luminosity and Lyman continuum emission, instead of their ratios (as we did in Fig. 16). Using the same approach (see Fig. 17), we confirm the existence of a correlation between  $L$  and  $M_{\text{gas}}$ , and  $N_{\text{Ly}}$  and  $M_{\text{gas}}$ . Following URQ13, we verified that

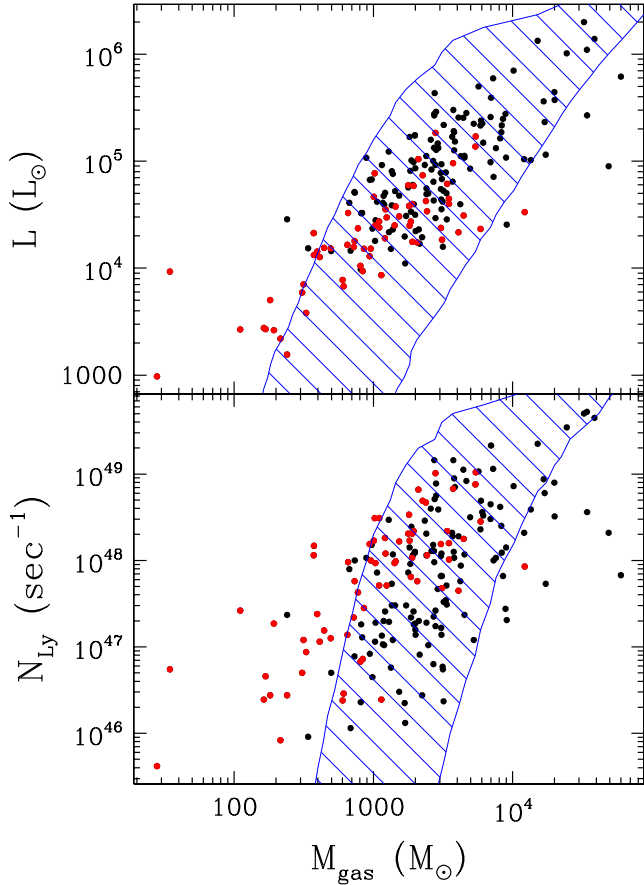


**Fig. 17.** *Top:* bolometric luminosity versus clump mass for the CORNISH HII regions with estimated distance. The red points indicate sources with Lyman excess. The hatched area corresponds to 90% of the simulated clusters assuming a star formation efficiency of 5%. *Bottom:* same as top panel for the Lyman continuum photon rate.

such correlations were not due to the fact that all these quantities ( $L$ ,  $N_{\text{Ly}}$ , and  $M_{\text{gas}}$ ) scale like  $d^2$ . For this purpose we performed a partial Spearman correlation test (see also Urquhart et al. 2013a and references therein), which gives correlation coefficients of 0.72 for  $L$ ,  $M_{\text{gas}}$ , and  $d$ , and 0.54 for  $N_{\text{Ly}}$ ,  $M_{\text{gas}}$ , and  $d$ . For 197 degrees of freedom, these values correspond to a null probability that the correlations  $L$  vs.  $M_{\text{gas}}$  and  $N_{\text{Ly}}$  vs.  $M_{\text{gas}}$  are *not* significant. Comparison with cluster simulations (shaded blue region in Fig. 16) confirm a star formation efficiency of 5%, independent of mass and luminosity of the cluster. This is interpreted by URQ13 as evidence that more massive clumps form more massive stars.

#### 4.4. Clump stability

We have also investigated whether the clumps associated with the selected HII regions are in virial equilibrium. To compute the virial mass,  $M_{\text{vir}}$ , one needs an estimate of the velocity dispersion in the molecular clumps, namely of the FWHM of a molecular line. This information is obviously missing in our continuum data, but we were able to recover it from the literature. Many of our targets have also been studied by URQ13, who estimated the corresponding  $M_{\text{vir}}$  using both new line observations and data from the literature. For the sake of comparison with our clump mass estimates, we scaled URQ13 virial masses to the distances and radii that we adopted. Moreover, we took the ammonia line

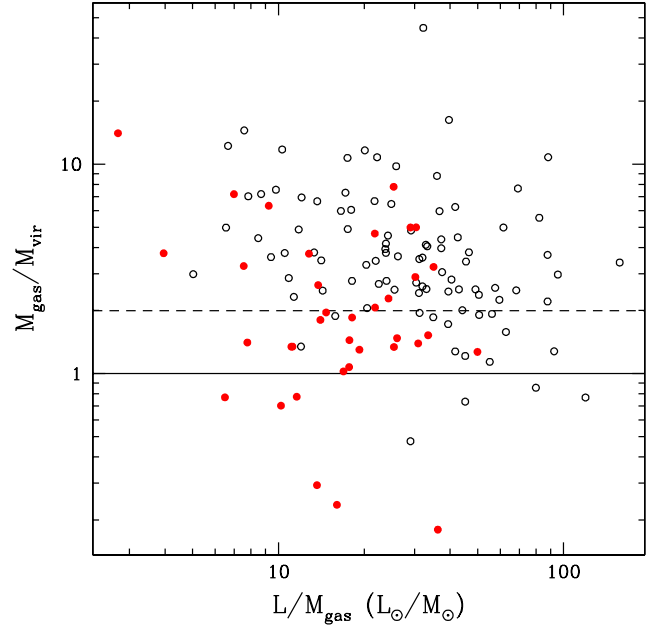


**Fig. 18.** Virial ratio as a function of the luminosity-to-mass ratio for all the sources for which a measurement of the line FWHM in a high density tracer is available. The solid points denote the sources with Lyman excess. The continuous line marks the equilibrium condition  $M_{\text{gas}}/M_{\text{vir}} = 1$  if only gravitation and turbulent motions are considered, while the dashed line corresponds to virial equilibrium when equipartition between kinetic and magnetic energy is assumed (see URQ13).

widths from Wielen et al. (2012) and Urquhart et al. (2011) to calculate  $M_{\text{vir}}$  for some of the sources not in URQ13. For the sake of consistency with these authors, we used their Eqs. (3) and (5) with the same assumptions.

In Fig. 18, we plot the virial ratio as a function of the ratio  $L/M_{\text{gas}}$ . If the clump stability changed during the evolution, one should find a correlation between the two quantities, as  $L/M_{\text{gas}}$  is expected to increase during star formation. No such trend is visible in the figure, and this is consistent with the previous conclusion that our sample spans a relatively narrow range of ages. The plot confirms the findings of URQ13, namely that almost all of the sources are supervirial. This is in agreement also with other studies (e.g., Fontani et al. 2002; Kauffmann et al. 2013) and supports the idea that clumps above  $\sim 10^3 M_{\odot}$  in high-mass star forming regions are unstable against gravitational collapse.

In the same figure, we also make a distinction between sources with Lyman excess (red solid points) and those without (black empty points). Interestingly, the distribution of the former appears skewed to the bottom left of the plot. This is confirmed by the mean values of the logarithms of the two ratios, which are  $\langle \log_{10}(M_{\text{gas}}/M_{\text{vir}}) \rangle = 0.26$  for the Lyman-excess sources and 0.55 for the others, and  $\langle \log_{10}(L/M_{\text{gas}}) \rangle = 1.2$  for the Lyman-excess sources and 1.4 for the others. According to the K-S test, the probability that sources with and without Lyman-excess have the same distribution is  $3 \times 10^{-4}$  for  $\log_{10}(L/M_{\text{gas}})$  and  $5 \times 10^{-5}$  for  $\log_{10}(M_{\text{gas}}/M_{\text{vir}})$ , which supports the existence of a real difference between the two samples. These findings hint at slightly different evolutionary phases for the two types of objects, with the Lyman-excess sources being embedded in clumps closer to virial equilibrium and thus at the beginning of the collapse phase. In particular, it is worth noting that only 42% of the Lyman-excess sources have  $M_{\text{gas}}/M_{\text{vir}} > 2$  (the critical value for

clumps in virial equilibrium assuming equipartition between kinetic and magnetic energy; see URQ13), as opposed to 83% of the other xxx sources.

## 5. Summary and conclusions

We have identified the *Herschel*/Hi-GAL IR counterparts of the young HII regions detected in the CORNISH survey, with the aim of studying the properties of the associated early-type stars and possibly of drawing some conclusion on the star formation process. Out of 281 HII regions, we were able to reconstruct the SED for 204 objects. We determined the bolometric and Lyman continuum luminosity for 200 of these because it was not possible to obtain a kinematic distance estimate for four HII regions in the sample. We also estimated the masses of the associated molecular clumps from the (sub)millimeter flux densities.

We find that 67 objects present a “Lyman excess”, as the Lyman continuum emission exceeds the maximum value expected for the same bolometric luminosity. No definitive explanation can be identified for this effect. We propose that infall onto the star and/or an associated accretion disk might cause the shocked material to emit additional UV photons that add up to the normal Lyman continuum of the OB star. While some models appear to support this interpretation, significant progress in the numerical calculations is still needed to prove our hypothesis and demonstrate that HII regions are undergoing accretion during a considerable fraction of their lives.

We construct a distance-independent plot of the ratio between the Lyman continuum and bolometric luminosity versus the ratio between the bolometric luminosity and corresponding clump mass, and use cluster simulations to fit the observed distribution in this plot. The result is that a good match is found if only 5% of the clump mass is converted into stars, consistent with previous estimates of the star formation efficiency in similar objects.

Finally, we find that the majority of clumps associated with all HII regions of our sample are supervirial and hence unstable against gravitational collapse. However, those associated with Lyman-excess sources are on average closer to equilibrium, hinting at these objects being in a slightly earlier evolutionary phase.

*Acknowledgements.* G.S.S. acknowledges support received through grants awarded by NASA. *Herschel* Hi-GAL data processing, maps production and source catalogue generation have been possible thanks to Contracts I/038/080/0 and I/0 29/12/0 from ASI, Agenzia Spaziale Italiana. This paper made use of information from the Red MSX Source survey database at [http://rms.leeds.ac.uk/cgi-bin/public/RMS\\_DATABASE.cgi](http://rms.leeds.ac.uk/cgi-bin/public/RMS_DATABASE.cgi) which was constructed with support from the Science and Technology Facilities Council of the UK. This publication also makes use of data products from the Wide-field Infrared Survey Explorer, which is a joint project of the University of California, Los Angeles, and the Jet Propulsion Laboratory/California Institute of Technology, funded by the National Aeronautics and Space Administration. This research made use of data products from the Midcourse Space Experiment. Processing of the data was funded by the Ballistic Missile Defense Organization with additional support from NASA Office of Space Science. This research has also made use of the

NASA/IPAC Infrared Science Archive, which is operated by the Jet Propulsion Laboratory, California Institute of Technology, under contract with the National Aeronautics and Space Administration.

## References

- Anderson, L. D., & Bania, T. M. 2009, *ApJ*, **690**, 706  
 Anderson, L. D., Bania, T. M., Balsaer, D. S., & Rood, R. T. 2012, *ApJ*, **754**, 62  
 Beuther, H., Schilke, P., Menten, K. M., et al. 2002, *ApJ*, **566**, 945  
 Brand, J., & Blitz, L. 1993, *A&A*, **275**, 67  
 Bronfman, L., Casassus, S., May, J., & Nyman, L.-Å. 1996, *A&AS*, **115**, 81  
 Contreras, Y., Schuller, F., Urquhart, J. S., et al. 2013, *A&A*, **549**, A45  
 Crowther, P. A. 2005, in *Massive Star Birth: a Crossroads of Astrophysics*, eds. R. Cesaroni, M. Felli, E. Churchwell, & M. Walmsley (Cambridge University Press), *IAU Symp.*, **227**, 389  
 Davies, B., Hoare, M. G., Lumsden, S. L., et al. 2011, *MNRAS*, **416**, 972  
 Diaz-Miller, R. I., Franco, J., & Shore, S. N. 1998, *ApJ*, **501**, 192  
 Fontani, F., Cesaroni, R., Caselli, P., & Olmi, L. 2002, *A&A*, **389**, 603  
 Ginsburg, A., Glenn, J., Rosolowsky, E., et al. 2013, *ApJS*, **208**, 14  
 Hoare, M. G., Purcell, C. R., Churchwell, E. B., et al. 2012, *PASP*, **124**, 939  
 Hosokawa, T., & Omukai, K. 2009, *ApJ*, **691**, 823  
 Jones, C., & Dickey, J. M. 2012, *ApJ*, **753**, 62  
 Kauffmann, J., Pillai, T., & Goldsmith, P. F. 2013, *ApJ*, **779**, 185  
 Kolpak, M. A., Jackson, J. M., Bania, T. M., Clemens, D. P., & Dickey, J. M. 2003, *ApJ*, **582**, 756  
 Kroupa, P., Tout, C. A., & Gilmore, G. 1993, *MNRAS*, **262**, 545  
 Kurtz, S. 2005, in *Massive Star Birth: a Crossroads of Astrophysics*, eds. R. Cesaroni, M. Felli, E. Churchwell, & M. Walmsley (Cambridge University Press), *IAU Symp.*, **227**, 111  
 Lumsden, S. L., Hoare, M. G., Urquhart, J. S., et al. 2013, *ApJS*, **208**, 11  
 Martins, F., Schaerer, D., & Hillier, D. J. 2005, *A&A*, **436**, 1049  
 Molinari, S., Swinyard, B., Bally, J., et al. 2010, *PASP*, **122**, 314  
 Molinari, S., Schisano, E., Faustini, F., et al. 2011, *A&A*, **530**, A133  
 Mottram, L., Hoare, M. G., Davies, B., et al. 2011, *ApJ*, **730**, L33  
 Ossenkopf, V., & Henning, Th. 1994, *A&A*, **291**, 943  
 Panagia, N. 1973, *AJ*, **78**, 929  
 Pandian, J. D., Momjian, E., & Goldsmith, P. F. 2008, *A&A*, **486**, 191  
 Pilbratt, G. L., Riedinger, J. R., Passvogel, T., et al. 2010, *A&A*, **518**, L1  
 Price, S. D., Egan, M. P., & Shipman, R. F. 1999, *Astrophysics with Infrared Surveys: A prelude to SIRTf*, eds. M. D. Bica, R. M. Cutri, & B. F. Madore, *ASP Conf. Ser.*, **177**, 394  
 Purcell, C. R., Hoare, M. G., Cotton, W. D., et al. 2013, *ApJS*, **205**, 1  
 Quireza, C., Rood, R. T., Bania, T. M., Balsaer, D. S., & Maciel, W. J. 2006, *ApJ*, **653**, 1226  
 Robitaille, T. P., Whitney, B. A., Indebetouw, R., & Wood, K. 2007, *ApJS*, **169**, 328  
 Sánchez-Monge, Á., Beltrán, M. T., Cesaroni, R., et al. 2013, *A&A*, **550**, A21  
 Shirley, Y. L., Ellsworth-Bowers, T. P., Svoboda, B., et al. 2013, *ApJS*, **209**, 2  
 Schuller, F., Menten, K. M., Contreras, Y., et al. 2009, *A&A*, **504**, 415  
 Sewilo, M., Watson, C., Araya, E., et al. 2004, *ApJS*, **154**, 553  
 Smith, M. D. 2014, *MNRAS*, **438**, 1051  
 Smith, L. J., Norris, R. P. F., & Crowther, P. A. 2002, *MNRAS*, **337**, 1309  
 Thompson, R. I. 1984, *ApJ*, **283**, 165  
 Urquhart, J. S., Morgan, L. K., Figura, C. C., et al. 2011, *MNRAS*, **418**, 1689  
 Urquhart, J. S., Moore, T. J. T., Schuller, F., et al. 2013a, *MNRAS*, **431**, 1752  
 Urquhart, J. S., Thompson, M. A., Moore, T. J. T., et al. 2013b, *MNRAS*, **435**, 400 (URQ13)  
 Vacca, W. D., Garmany, C. D., & Shull, M. 1996, *ApJ*, **460**, 914  
 Watson, C., Araya, E., Sewilo, M., et al. 2003, *ApJ*, **587**, 714  
 White, R. L., Becker, R. H., & Helfand, D. J. 2005, *AJ*, **130**, 586  
 Wienen, M., Wyrowski, F., Schuller, F., et al. 2012, *A&A*, **544**, A146  
 Wood, D. O. S., & Churchwell, E. 1989, *ApJ*, **340**, 265  
 Wright, E. L., Eisenhardt, P. R. M., Mainzer, A. K., et al. 2010, *AJ*, **140**, 1868

## Appendix A

Table A.1. Flux densities of the HII regions classified as “ultracompact” and “compact” in the CORNISH catalogue.

#	CORNISH name	$\alpha^{\text{CORNISH}}$ (deg)	$\delta^{\text{CORNISH}}$ (deg)	$S_5$ GHz (mJy)	$\alpha^{\text{Hi-GAL}}$ (deg)	$\delta^{\text{Hi-GAL}}$ (deg)	$S_{21}$ $\mu\text{m}$ (Jy)	$S_{22}$ $\mu\text{m}$ (Jy)	$S_{70}$ $\mu\text{m}$ (Jy)	$S_{160}$ $\mu\text{m}$ (Jy)	$S_{250}$ $\mu\text{m}$ (Jy)	$S_{350}$ $\mu\text{m}$ (Jy)	$S_{500}$ $\mu\text{m}$ (Jy)	$S_{870}$ $\mu\text{m}$ (Jy)	$S_{1100}$ $\mu\text{m}$ (Jy)
1	G010.3204-00.2328	272.3230	-20.1231	32.4	272.3233	-20.1228	8.75	11.58	178.50	154.10	147.70	55.09	21.61	5.21	2.02
2	G010.3204-00.2586	272.3470	-20.1353	18.2	272.3474	-20.1350	–	1.31	232.30	391.20	379.60	131.40	39.59	14.93	4.56
3	G010.4724+00.0275	272.1591	-19.8638	57.7	272.1593	-19.8636	22.48	53.14	4032.00	2895.00	1605.00	499.40	518.10	88.12	39.52
4	G010.6234-00.3837	272.6196	-19.9303	2544.3	272.6188	-19.9299	54.24	95.10	7843.00	5540.00	1952.00	540.00	730.90	116.90	42.63
5	G010.9584+00.0221	272.4141	-19.4411	196.0	272.4138	-19.4411	15.17	19.08	897.90	594.60	439.80	121.30	33.27	13.55	4.48
6	G010.9656+00.0089	272.4294	-19.4413	51.8	272.4289	-19.4405	13.70	21.18	145.30	99.85	218.90	61.71	19.52	5.40	–
7	G011.0328+00.0274	272.4473	-19.3734	5.7	272.4468	-19.3734	3.23	3.90	82.37	69.59	51.60	13.76	3.92	1.39	0.62
8	G011.0339+00.0616	272.4154	-19.3552	103.4	272.4158	-19.3555	23.09	31.73	510.90	384.30	289.20	68.30	18.65	6.05	2.98
9	G011.1104-00.3985	272.8833	-19.5116	305.4	272.8823	-19.5109	82.28	116.40	534.40	513.60	534.00	193.20	60.27	–	14.90
10	G011.1712-00.0662	272.6046	-19.2965	102.2	272.6037	-19.2964	4.69	6.20	110.10	93.84	75.83	24.37	9.59	1.43	0.38
11	G011.9032-00.1407	273.0469	-18.6919	42.4	273.0473	-18.6912	–	2.89	320.30	417.50	445.50	140.00	49.45	20.03	6.46
12	G011.9446-00.0369	272.9719	-18.6049	943.6	272.9715	-18.6052	138.60	330.40	708.80	436.40	294.70	88.58	24.83	7.62	4.02
13	G011.9786-00.0973	273.0449	-18.6049	4.5	273.0450	-18.6049	–	2.82	59.53	51.18	41.98	12.25	4.34	–	–
14	G012.1988-00.0345	273.0984	-18.3816	62.7	273.0976	-18.3812	9.39	13.18	511.40	494.90	398.40	111.00	31.46	7.42	3.56
15	G012.2081-00.1019	273.1654	-18.4059	207.9	273.1655	-18.4052	–	9.16	947.90	1196.00	917.20	397.00	200.90	37.39	12.88
16	G012.4294-00.0479	273.2274	-18.1857	45.2	273.2279	-18.1858	4.05	5.17	105.70	99.80	51.57	25.50	–	5.71	4.84
17	G012.4317-01.1112	274.2134	-18.6912	69.0	274.2140	-18.6920	77.31	166.00	–	–	885.60	260.30	80.21	–	–
18	G012.9995-00.3583	273.8008	-17.8335	20.1	273.8008	-17.8337	3.86	6.03	254.80	433.50	456.10	157.60	52.79	9.86	3.88
19	G013.2099-00.1428	273.7084	-17.5457	946.8	273.7084	-17.5447	22.75	43.08	253.40	675.20	643.90	207.70	89.49	30.64	10.36
20	G013.3850+00.0684	273.6025	-17.2923	603.9	273.6046	-17.2909	36.06	72.05	224.50	248.40	247.00	76.32	26.07	5.45	2.56
21	G013.8726+00.2818	273.6492	-16.7603	1447.6	273.6511	-16.7614	254.80	718.20	1597.00	1385.00	1368.00	396.90	120.30	29.72	11.46
22	G014.1741+00.0245	274.0352	-16.6183	47.7	274.0346	-16.6176	4.97	8.14	93.61	86.33	119.60	43.63	16.59	3.02	0.94
23	G014.4894+00.0194	274.1954	-16.3436	36.6	274.1960	-16.3436	4.22	7.55	84.18	138.60	163.00	86.75	32.77	–	2.94
24	G014.7785-00.3328	274.6612	-16.2562	18.2	274.6611	-16.2562	5.08	7.24	93.90	101.00	99.00	32.00	10.51	4.02	0.94
25	G016.1448+00.0088	275.0192	-14.8905	14.8	275.0190	-14.8906	–	5.48	135.20	124.10	116.80	37.12	12.70	2.51	0.67
26	G016.3913-00.1383	275.2729	-14.7424	124.3	275.2734	-14.7425	–	2.48	80.70	73.32	59.69	21.80	–	4.08	0.61
27	G016.9445-00.0738	275.4834	-14.2239	519.3	275.4831	-14.2239	34.16	45.44	636.50	313.00	151.80	34.84	9.94	–	3.14
28	G017.0299-00.0696	275.5210	-14.1466	5.4	275.5210	-14.1468	–	1.18	69.37	125.30	128.10	39.90	12.83	3.42	1.21
29	G017.1141-00.1124	275.6008	-14.0924	17.2	275.6008	-14.0924	9.64	12.32	186.50	131.60	95.43	26.95	7.79	–	–
30	G017.5549+00.1654	275.5616	-13.5728	7.1	275.5620	-13.5730	–	2.50	60.84	74.21	78.38	28.31	10.59	2.38	–
31	G017.9850+00.1266	275.8042	-13.2112	10.4	275.8033	-13.2111	–	2.38	73.75	64.62	57.68	20.86	7.13	1.27	–
32	G018.1460-00.2839	276.2532	-13.2576	856.2	276.2532	-13.2588	56.99	–	247.90	407.30	385.90	118.50	52.51	–	–
33	G018.3024-00.3910	276.4262	-13.1719	1277.9	276.4248	-13.1748	318.00	1058.00	783.50	726.20	977.60	381.00	132.30	28.31	8.78
34	G018.4433-00.0056	276.1444	-12.8682	81.3	276.1442	-12.8680	–	3.59	139.20	171.60	145.50	35.06	17.61	9.18	–
35	G018.4614-00.0038	276.1514	-12.8513	342.1	276.1511	-12.8514	21.34	34.60	1166.00	862.20	603.10	148.30	42.68	20.38	9.93
36	G018.6738-00.2363	276.4643	-12.7724	109.4	276.4615	-12.7726	9.71	14.51	70.88	51.27	81.94	32.00	12.05	4.11	–
37	G018.7106+00.0002	276.2672	-12.6292	107.5	276.2667	-12.6289	11.29	12.38	224.00	153.50	164.30	56.43	21.39	6.34	3.00
38	G018.7612+00.2630	276.0536	-12.4616	51.4	276.0531	-12.4618	–	6.26	194.30	259.80	241.50	96.31	38.26	10.44	3.18
39	G018.8250-00.4675	276.7460	-12.7462	11.4	276.7456	-12.7459	18.76	25.67	165.30	163.80	176.20	79.63	29.30	2.65	–
40	G018.8338-00.3002	276.5984	-12.6613	131.4	276.5979	-12.6604	15.09	19.51	503.30	314.60	225.80	55.51	15.86	7.99	2.41
41	G019.0035+00.1280	276.2917	-12.3105	6.4	276.2915	-12.3106	–	1.34	60.86	116.00	132.70	50.99	17.50	4.15	1.34
42	G019.0754-00.2874	276.7018	-12.4411	510.2	276.7025	-12.4399	67.32	47.58	1579.00	1476.00	934.30	432.60	141.40	41.64	16.15
43	G019.4912+00.1352	276.5180	-11.8764	415.1	276.5178	-11.8765	49.35	87.06	336.10	170.20	206.20	49.35	–	–	2.19

Notes. The flux densities were obtained from the Hi-GAL images and ancillary data (see Sect. 3.1). <sup>(c)</sup> The peak coordinates could not be determined because some of the Hi-GAL images are saturated.

Table A.1. continued.

#	CORNISH name	$\alpha_{\text{CORNISH}}$ (deg)	$\delta_{\text{CORNISH}}$ (deg)	$S_{5\text{ GHz}}$ (mJy)	$\alpha_{\text{HI-GAL}}$ (deg)	$\delta_{\text{HI-GAL}}$ (deg)	$S_{21\text{ }\mu\text{m}}$ (Jy)	$S_{22\text{ }\mu\text{m}}$ (Jy)	$S_{70\text{ }\mu\text{m}}$ (Jy)	$S_{160\text{ }\mu\text{m}}$ (Jy)	$S_{250\text{ }\mu\text{m}}$ (Jy)	$S_{350\text{ }\mu\text{m}}$ (Jy)	$S_{500\text{ }\mu\text{m}}$ (Jy)	$S_{870\text{ }\mu\text{m}}$ (Jy)	$S_{1100\text{ }\mu\text{m}}$ (Jy)
44	G019.6062-00.9018	277.5116	-12.2561	78.0	277.5114	-12.2550	33.36	53.14	220.50	158.10	137.30	39.06	15.99	6.76	—
45	G019.6087-00.2351	276.9095	-11.9434	2900.9	276.9089	-11.9440	262.90	1160.00	3733.00	2721.00	1280.00	584.70	255.30	44.85	18.70
46	G019.6781-00.1318	276.8480	-11.8337	122.8	276.8503	-11.8337	32.42	59.41	109.90	80.69	103.10	20.18	—	—	—
47	G019.7281-00.1135	276.8557	-11.7823	26.2	276.8549	-11.7825	5.64	7.20	188.90	164.70	143.40	45.70	16.26	7.61	2.44
48	G019.7407-00.0281	276.5063	-11.5864	239.0	276.5043	-11.5878	7.13	11.16	112.60	102.10	98.55	34.81	12.57	—	0.88
49	G019.7549-00.1282	276.8817	-11.7652	36.5	276.8812	-11.7654	59.08	71.75	512.20	325.80	264.80	58.48	16.64	11.23	4.26
50	G020.0809-00.1362	277.0434	-11.4802	512.3	277.0428	-11.4802	—	56.40	1998.00	1454.00	835.70	302.80	130.80	18.43	10.03
51	G020.3633-00.0136	277.0667	-11.1734	55.1	277.0663	-11.1731	3.28	2.85	112.50	207.40	208.90	66.55	21.19	4.84	1.63
52	G020.4319+00.3572	276.7650	-10.9401	10.1	276.7646	-10.9397	7.41	9.81	96.86	71.31	53.46	15.46	4.88	1.66	0.43
53	G020.7619-00.0646	277.3015	-10.8440	10.0	277.3006	-10.8432	25.73	40.53	387.20	263.90	181.10	41.59	8.75	—	0.90
54	G020.9636-00.0744	277.4055	-10.6698	11.3	277.4051	-10.6703	—	2.74	112.50	89.57	71.05	19.23	6.18	1.40	0.83
55	G021.3571-00.1766	277.6831	-10.3685	24.9	277.6830	-10.3682	—	37.20	257.30	172.30	130.40	41.54	11.99	—	0.85
56	G021.3855-00.2541	277.7663	-10.3792	113.9	277.7662	-10.3789	32.59	36.74	653.10	517.60	412.90	139.30	44.41	—	2.93
57	G021.4257-00.5417	278.0439	-10.4762	94.8	278.0430	-10.4788	38.57	82.29	410.00	463.70	242.40	80.33	27.88	—	6.49
58	G021.6034-00.1685	277.7917	-10.1463	19.8	277.7912	-10.1461	3.39	3.26	78.79	50.19	44.46	13.43	—	—	—
59	G021.8751+00.0075	277.7603	-9.8252	566.7	277.7602	-9.8247	30.42	47.10	525.20	374.90	289.80	91.74	29.94	—	3.29
60	G023.1974-00.0006	278.3871	-8.6551	10.0	278.3873	-8.6524	13.33	17.04	92.74	326.50	348.20	124.00	47.51	—	10.72
61	G023.2654+00.0765	278.3496	-8.5596	88.6	278.3493	-8.5597	12.09	12.79	351.80	461.40	350.70	96.14	30.19	—	2.89
62	G023.4553-00.2010	278.6872	-8.5186	14.4	278.6870	-8.5185	—	2.16	162.80	183.70	105.10	3.64	0.92	—	—
63	G023.4835+00.0964	278.4335	-8.3565	8.2	278.4332	-8.3564	—	3.62	161.10	310.00	307.70	89.86	29.44	—	6.27
64	G023.7110+00.1705	278.4728	-8.1205	208.5	278.4724	-8.1205	104.20	257.70	658.80	658.70	465.00	135.30	42.72	—	9.52
65	G023.8618-00.1250	278.8081	-8.1231	39.2	278.8082	-8.1228	—	8.07	95.30	63.60	261.90	99.84	—	—	—
66	G023.8985+00.0647	278.6552	-8.0029	43.4	278.6551	-8.0026	9.54	10.89	250.20	273.60	217.20	66.95	20.62	—	3.68
67	G023.9564+00.1493	278.6050	-7.9127	1161.2	278.6065	-7.9127	376.70	1284.00	1237.00	883.90	420.30	147.90	52.19	—	12.66
68	G024.1839+00.1199	278.7384	-7.7241	3.8	278.7378	-7.7242	6.75	9.54	155.90	223.70	239.40	84.32	28.83	—	1.79
69	G024.4721+00.4877	278.5430	-7.2989	55.2	278.5444	-7.2991	—	—	772.80	589.90	494.40	148.80	—	—	18.25
70	G024.4736+00.4950	278.5370	-7.2948	128.9	278.5390	-7.2934	—	—	416.10	576.80	335.80	137.50	85.58	—	—
71	G024.4921-00.0386	279.0237	-7.5231	140.1	279.0229	-7.5232	—	17.30	372.00	860.70	927.50	328.70	103.30	—	12.73
72	G024.5065-00.2224	279.1950	-7.5947	205.6	279.1940	-7.5947	55.80	132.90	524.60	351.40	284.20	81.03	30.86	—	4.97
73	G024.8497+00.0881	279.0758	-7.1476	19.9	279.0767	-7.1475	64.40	561.60	279.30	239.80	232.90	72.84	22.81	—	1.63
74	G024.9237+00.0777	279.1180	-7.0865	172.5	279.1190	-7.0859	3.47	4.32	155.70	150.50	111.70	49.88	—	—	—
75	G025.3055+00.5305	278.8912	-6.5391	50.7	278.8911	-6.5389	9.17	11.42	154.80	118.60	48.16	11.45	3.79	—	—
76	G025.3824-00.1812	279.5636	-6.7979	661.0	279.5640	-6.7976	1357.00	—	2038.00	1156.00	704.60	175.50	55.37	—	11.70
77	G025.3948+00.0332	279.3774	-6.6888	296.9	279.3763	-6.6880	20.43	33.19	677.20	412.40	260.70	66.42	16.85	—	2.77
78	G025.3970+00.5614	278.9060	-6.4440	173.1	278.9059	-6.4436	13.73	15.76	482.40	446.70	390.20	106.90	32.84	—	2.18
79	G025.3981-00.1411	279.5345	-6.7662	2132.2	279.5348	-6.7656	283.50	—	2628.00	1390.00	1187.00	339.60	118.70	—	20.37
80	G025.7157+00.0487	279.5117	-6.3964	20.8	279.5115	-6.3961	40.43	56.58	183.00	158.60	131.30	—	—	—	—
81	G025.8011-00.1568	279.7348	-6.4148	32.0	279.7348	-6.4146	79.90	87.06	619.80	440.90	356.90	97.43	37.53	—	2.34
82	G026.0083+00.1369	279.5678	-6.0960	6.6	279.5677	-6.0962	—	0.30	3.00	4.24	7.92	—	—	—	—
83	G026.0916-00.0565	279.7791	-6.1107	11.6	279.7788	-6.1109	6.34	9.11	205.30	175.70	164.00	46.69	14.92	—	1.95
84	G026.1094-00.0937	279.8205	-6.1119	4.7	279.8203	-6.1121	5.91	6.92	233.70	132.90	89.58	18.67	4.53	—	0.57
85	G026.5444+00.4169	279.5674	-5.4922	413.4	279.5657	-5.4910	120.00	345.60	557.90	223.70	245.20	81.13	27.57	—	4.29
86	G026.5976-00.0236	279.9828	-5.6460	69.9	279.9831	-5.6459	13.03	18.43	352.30	217.40	203.60	57.92	18.16	—	2.34
87	G026.6089-00.2121	280.1563	-5.7222	201.4	280.1564	-5.7223	—	22.03	244.50	96.52	80.85	21.36	6.66	—	—
88	G026.8304-00.2067	280.2535	-5.5228	12.3	280.2539	-5.5227	—	4.10	67.97	48.67	33.44	9.55	4.17	—	—
89	G027.1859-00.0816	280.3053	-5.1494	19.8	280.3054	-5.1500	18.96	27.47	985.00	553.90	370.50	85.71	19.50	—	3.34
90	G027.2800+00.1447	280.1465	-4.9627	428.0	280.1466	-4.9630	25.52	48.73	275.80	234.80	325.10	65.45	—	—	—

Table A.1. continued.

#	CORNISH name	$\alpha_{\text{CORNISH}}$ (deg)	$\delta_{\text{CORNISH}}$ (deg)	$S_5$ GHz (mJy)	$\alpha_{\text{HI-GAL}}$ (deg)	$\delta_{\text{HI-GAL}}$ (deg)	$S_{21\mu\text{m}}$ (Jy)	$S_{22\mu\text{m}}$ (Jy)	$S_{70\mu\text{m}}$ (Jy)	$S_{160\mu\text{m}}$ (Jy)	$S_{250\mu\text{m}}$ (Jy)	$S_{350\mu\text{m}}$ (Jy)	$S_{500\mu\text{m}}$ (Jy)	$S_{870\mu\text{m}}$ (Jy)	$S_{1100\mu\text{m}}$ (Jy)
91	G027.3644-00.1657	280.4624	-5.0292	60.1	280.4627	-5.0288	15.38	21.25	629.90	1033.00	834.30	387.70	198.80	-	12.44
92	G027.5637+00.0845	280.3308	-4.7391	162.5	280.3299	-4.7378	4.38	7.24	91.58	220.10	210.00	70.07	32.83	-	4.73
93	G027.9352+00.2056	280.3931	-4.3518	4.4	280.3931	-4.3520	7.63	8.56	290.20	261.70	211.80	67.58	19.57	-	4.63
94	G027.9782+00.0789	280.5270	-4.3721	124.0	280.5264	-4.3727	17.71	25.71	366.50	326.20	319.10	110.90	38.33	-	6.61
95	G028.2003-00.0494	280.7422	-4.2326	297.9	280.7422	-4.2325	65.37	122.50	2181.00	1911.00	1264.00	508.20	215.60	-	14.38
96	G028.2447+00.0131	280.7067	-4.1640	63.2	280.7067	-4.1614	19.81	29.53	158.00	157.10	69.20	32.14	11.71	-	2.92
97	G028.2879-00.3641	281.0629	-4.2989	552.8	281.0630	-4.2991	685.90	1208.00	1653.00	658.30	563.80	213.00	78.45	-	9.66
98	G028.4518+00.0027	280.8109	-3.9852	33.8	280.8110	-3.9851	-	2.95	137.00	107.80	84.79	22.63	8.96	-	4.23
99	G028.5816+00.1447	280.7436	-3.8048	40.0	280.7433	-3.8050	-	2.29	103.70	80.97	63.12	19.57	7.26	-	0.91
100	G028.6082+00.0185	280.8687	-3.8387	210.1	280.8685	-3.8384	33.96	60.40	815.90	633.30	516.70	152.50	38.34	-	18.07
101	G028.6523+00.0273	280.8809	-3.7959	228.9	280.8811	-3.7952	9.99	15.22	347.20	392.60	421.10	141.40	51.46	-	15.65
102	G028.6869+00.1770	280.7635	-3.6961	103.0	280.7633	-3.6958	9.34	12.93	228.60	156.70	98.92	24.01	7.30	-	0.68
103	G029.9559-00.0168	281.5174	-2.6559	3116.2	281.5158	-2.6558	1452.00	4376.00	5625.00	2785.00	1488.00	568.60	216.10	-	35.71
104	G030.0096-00.2734	281.7696	-2.7253	4.5	281.7695	-2.7253	-	2.21	200.50	208.00	249.10	87.74	37.43	-	8.45
105	G030.2527+00.0540	281.5892	-2.3598	96.8	281.5893	-2.3594	9.07	11.31	233.00	181.80	142.10	41.60	14.65	-	3.76
106	G030.5313+00.0205	281.7466	-2.1268	85.5	281.7472	-2.1237	-	8.72	834.40	507.10	305.80	85.72	30.69	-	4.28
107	G030.5353+00.0204	281.7473	-2.1235	710.4	281.7472	-2.1237	63.62	97.69	834.40	507.10	305.80	85.72	30.69	-	8.58
108	G030.5887+00.0428	281.8287	-2.1048	92.4	281.8286	-2.1046	8.54	11.83	1267.00	925.60	731.70	207.90	64.41	-	52.90
109	G030.7532-00.0511	281.9111	-1.9623	301.7	281.9103	-1.9624	-	-	1587.00	1022.00	933.80	229.00	-	-	5.68
110	G030.7579+00.2042	281.6855	-1.8413	26.2	281.6855	-1.8412	7.78	10.90	247.30	216.90	197.20	65.76	24.06	-	5.61
111	G030.8662+00.1143	281.8154	-1.7864	325.5	281.8157	-1.7862	60.80	70.31	1258.00	731.50	515.80	145.30	51.99	-	3.31
112	G030.9581+00.0869	281.8817	-1.7171	25.8	281.8827	-1.7165	13.77	19.73	331.90	292.60	267.40	79.53	24.95	-	-
113	G031.0495+00.4697	281.5827	-1.4610	13.6	281.5829	-1.4607	5.92	7.32	96.52	60.88	85.14	-	-	-	-
114	G031.0595+00.0922	281.9234	-1.6243	11.7	281.9231	-1.6241	5.01	6.85	190.50	131.00	77.96	18.53	7.01	-	0.49
115	G031.0709+00.0508	281.9657	-1.6343	248.6	281.9678	-1.6364	19.06	26.83	92.09	154.20	157.40	46.05	13.44	-	1.96
116	G031.1596+00.0448	282.0113	-1.5569	30.9	282.0100	-1.5568	6.93	10.02	179.10	224.70	209.60	63.70	21.20	-	4.84
117	G031.2435-00.1103	282.1877	-1.5529	686.7	282.1877	-1.5534	24.63	34.12	1175.00	646.80	410.60	100.10	27.56	-	6.19
118	G031.2801+00.0632	282.0492	-1.4419	268.9	282.0513	-1.4417	34.59	62.88	1138.00	1192.00	952.70	451.60	175.80	-	17.60
119	G031.3959-00.2570	282.3886	-1.4859	81.0	282.3877	-1.4841	109.20	285.40	1402.00	1163.00	865.00	233.40	62.58	-	6.73
120	G031.4130+00.3065	281.8929	-1.2124	954.8	281.8929	-1.2119	21.24	34.45	1414.00	1780.00	1319.00	693.80	335.40	-	28.09
121	G031.5815+00.0744	282.1774	-1.1679	14.5	282.1744	-1.1669	-	11.15	536.20	851.90	745.90	239.20	78.72	-	5.83
122	G032.0297+00.0491	282.4044	-0.7806	26.7	282.4045	-0.7803	20.41	25.34	170.40	112.40	74.02	-	-	-	-
123	G032.1502+00.1329	282.3856	-0.6349	533.6	282.3857	-0.6356	103.60	163.30	568.30	558.00	629.60	229.00	84.08	-	7.16
124	G032.2730+00.2258	282.7597	-0.6902	309.3	282.7597	-0.6898	19.03	29.20	252.90	184.70	130.50	41.60	14.62	-	1.64
125	G032.4727+00.2036	282.4690	-0.3158	97.4	282.4686	-0.3158	20.35	26.08	278.20	227.60	147.90	45.67	16.54	-	4.17
126	G032.7398+00.1940	282.5992	-0.0826	3.4	282.5987	-0.0825	2.72	2.14	46.16	55.59	98.53	46.26	19.86	-	3.19
127	G032.7492-00.0643	282.8334	-0.1919	13.1	282.8332	-0.1917	3.63	5.04	130.20	111.50	171.80	57.91	-	-	-
128	G032.7966+00.1909	282.6290	-0.0324	3123.4	282.6278	-0.0333	174.90	335.60	3870.00	2628.00	1308.00	509.40	206.60	-	13.90
129	G032.9273+00.6060	282.3179	0.2729	285.6	282.3178	0.2723	33.61	41.40	292.60	134.00	86.58	24.20	8.01	-	-
130	G033.1328-00.0923	283.0335	0.1368	378.6	283.0337	0.1370	-	8.98	618.50	752.90	654.40	197.00	60.68	-	5.58
131	G033.4163-00.0036	283.0846	0.4302	75.2	283.0840	0.4299	11.26	12.32	185.90	137.70	146.10	47.16	22.17	-	5.60
132	G033.8100-00.1864	283.4258	0.6964	107.6	283.4262	0.6967	67.28	85.55	933.70	454.20	281.70	65.58	17.24	-	3.95
133	G033.8113-00.1893	283.4292	0.6959	105.0	283.4262	0.6967	67.28	85.55	933.70	454.20	281.70	65.58	17.25	-	-
134	G033.9145+00.1105	283.2101	0.9246	842.2	283.2099	0.9249	193.90	244.00	1586.00	1418.00	951.00	484.80	169.40	-	13.27
135	G034.0901+00.4365	282.9990	1.2297	9.6	282.9989	1.2297	11.51	16.98	124.40	94.82	81.90	29.40	6.35	-	1.61

Table A.1. continued.

#	CORNISH name	$\alpha_{\text{CORNISH}}$ (deg)	$\delta_{\text{CORNISH}}$ (deg)	$S_{5 \text{ GHz}}$ (mJy)	$\theta_{\text{HI-GAL}}$ (deg)	$\delta_{\text{HI-GAL}}$ (deg)	$S_{21 \mu\text{m}}$ (Jy)	$S_{22 \mu\text{m}}$ (Jy)	$S_{70 \mu\text{m}}$ (Jy)	$S_{160 \mu\text{m}}$ (Jy)	$S_{250 \mu\text{m}}$ (Jy)	$S_{350 \mu\text{m}}$ (Jy)	$S_{500 \mu\text{m}}$ (Jy)	$S_{870 \mu\text{m}}$ (Jy)	$S_{1100 \mu\text{m}}$ (Jy)
136	G034.1324+00.4700	282.9882	1.2834	425.0	282.9881	1.2831	45.09	65.38	539.50	333.30	239.10	61.34	21.99	-	2.30
137	G034.1978-00.5912	283.9630	0.8570	10.5	283.9631	0.8557	10.59	15.63	282.10	278.10	226.10	74.75	25.21	-	-
138	G034.4032+00.2277	283.3278	1.4132	8.9	283.3273	1.4134	14.94	19.24	355.60	400.70	780.10	324.90	115.90	-	-
139	G034.5920+00.2434	283.3999	1.5884	20.2	283.3995	1.5883	3.09	3.75	88.92	77.18	61.14	17.93	5.16	-	1.09
140	G035.0242+00.3502	283.5020	2.0217	11.4	283.5020	2.0221	10.83	15.23	1665.00	1219.00	832.70	211.80	50.65	-	9.93
141	G035.0524-00.5177	284.2876	1.6508	67.8	284.2874	1.6516	29.98	39.42	269.80	195.10	135.00	40.69	16.89	-	2.80
142	G035.4570-00.1791	284.1710	2.1654	7.5	284.1703	2.1655	-	2.11	53.95	96.32	94.46	30.34	9.22	-	1.12
143	G035.4669+00.1394	283.8923	2.3196	317.6	283.8925	2.3198	185.30	296.90	1409.00	899.10	770.30	235.20	83.63	-	10.38
144	G035.5734+00.0679	284.0039	2.3816	285.2	284.0045	2.3819	32.82	56.95	430.40	422.80	420.20	150.50	66.25	-	21.09
145	G035.5781-00.0305	284.0940	2.3411	187.8	284.0940	2.3413	42.14	73.83	1812.00	957.10	644.90	156.00	40.80	-	7.94
146	G036.4057+00.0226	284.4249	3.1015	31.6	284.4254	3.1021	23.92	28.09	587.10	438.60	321.40	95.13	32.46	-	-
147	G037.5457-00.1120	285.0665	4.0536	406.5	285.0668	4.0542	66.85	119.40	678.30	494.40	365.50	103.20	31.45	-	3.25
148	G037.7347-00.1128	285.1541	4.2218	16.0	285.1536	4.2224	-	1.57	237.50	373.00	357.30	103.20	30.30	-	3.46
149	G037.7562+00.5605	284.5637	4.5489	35.7	284.5637	4.5487	3.80	4.79	122.30	97.08	75.16	23.94	7.81	-	-
150	G037.7633-00.2167	285.2588	4.1993	337.6	285.2572	4.2012	7.37	16.14	109.10	85.93	368.20	196.80	72.46	-	8.25
151	G037.8209+00.4125	284.7252	4.5385	46.2	284.7247	4.5375	5.83	8.66	312.60	374.50	313.20	76.89	21.64	-	3.04
152	G037.8683-00.6008	285.6507	4.1170	210.3	285.6505	4.1175	35.03	37.21	311.50	294.10	180.70	51.12	18.77	-	-
153	G037.8731-00.3996	285.4733	4.2144	2561.2	285.4730	4.2138	185.40	493.20	2226.00	1311.00	1021.00	281.50	85.51	-	8.90
154	G037.9723-00.0965	285.2486	4.4405	20.9	285.2483	4.4406	-	1.41	43.91	33.28	26.85	7.87	2.73	-	0.26
155	G038.6465-00.2260	285.6738	4.9806	11.5	285.6736	4.9806	4.94	6.10	122.70	113.60	95.99	24.70	7.69	-	0.75
156	G038.6529+00.0875	285.3969	5.1298	7.8	285.3965	5.1299	-	2.19	110.70	68.61	66.33	22.64	9.59	-	1.62
157	G038.6934-00.4524	285.8973	4.9186	19.9	285.8969	4.9186	6.81	9.12	179.20	206.80	199.90	64.69	21.75	-	1.73
158	G038.8756+00.3080	285.3022	5.4288	311.3	285.3021	5.4288	11.55	15.53	352.40	180.50	117.60	31.63	10.06	-	2.38
159	G039.1956+00.2255	285.5233	5.6755	62.3	285.5236	5.6755	13.47	15.21	171.70	89.86	58.39	14.78	4.06	-	0.62
160	G039.7277-00.3973	286.3246	5.8636	133.3	286.3249	5.8625	7.23	14.58	102.40	69.42	61.97	32.10	12.89	-	0.88
161	G039.8824-00.3460	286.3506	6.0241	276.9	286.3501	6.0241	25.58	29.23	443.60	339.90	277.80	85.42	25.28	-	2.56
162	G040.4251+00.7002	285.6650	6.9857	11.1	285.6649	6.9859	11.15	14.15	413.30	292.70	198.40	47.34	14.30	-	-
163	G041.7419+00.0973	286.8149	7.8788	227.4	286.8145	7.8791	27.05	33.44	338.50	212.40	91.23	23.94	7.73	-	0.99
164	G042.1090-00.4469	287.4731	7.9541	14.8	287.4728	7.9548	27.44	43.31	285.90	202.10	163.40	49.22	16.57	-	1.80
165	G042.4345-00.2605	287.4579	8.3289	83.7	287.4579	8.3297	81.81	123.00	469.60	230.10	160.30	45.57	8.69	-	4.86
166	G043.1489+00.0130	287.5460	9.0889	738.7	287.5456	9.0884	179.98	-	2304.00	791.50	705.40	173.70	39.91	-	11.38
167	G043.1651-00.0283	287.5917	9.0842	2714.3	287.5909	9.0844	519.00	-	4747.00	2065.00	1186.00	515.30	194.70	-	27.06
168	G043.1665+00.0106	287.5564	9.1035	3447.7	- <sup>a</sup>	- <sup>a</sup>	234.30	-	11000.00	5782.00	1635.00	652.60	227.20	-	146.40
169	G043.1706-00.0003	287.5682	9.1020	222.5	287.5683	9.1020	91.62	-	1445.00	1060.00	1572.00	419.50	139.80	-	-
170	G043.1763+00.0248	287.5481	9.1185	159.4	287.5489	9.1195	95.98	-	232.80	-	467.60	181.90	94.25	-	-
171	G043.1778-00.5181	288.0366	8.8683	181.6	288.0366	8.8687	-	23.93	398.60	531.70	403.20	114.70	39.07	-	6.73
172	G043.2371-00.0453	287.6396	9.1401	178.8	287.6397	9.1406	25.22	37.10	796.20	725.90	600.00	192.00	60.88	-	7.14
173	G043.3064-00.2114	287.8210	9.1247	20.1	287.8208	9.1250	60.78	39.39	581.10	538.90	472.50	143.10	45.04	-	2.34
174	G043.7954-00.1274	287.9751	9.5972	34.4	287.9750	9.5973	56.17	81.16	2497.00	1630.00	856.70	295.80	114.30	-	4.69
175	G043.8894-00.7840	288.6088	9.3764	528.2	288.6089	9.3764	106.50	124.90	651.00	517.60	502.10	181.20	60.10	-	-
176	G043.9675+00.9939	287.0460	10.2675	41.3	287.0458	10.2679	17.97	20.57	105.10	57.70	44.05	12.02	3.56	-	-
177	G044.3103+00.0410	288.0656	10.1315	5.5	288.0654	10.1319	15.29	18.82	561.90	456.80	350.50	93.51	28.23	-	5.01
178	G044.4228+00.5377	287.6708	10.4611	4.3	287.6705	10.4611	-	6.34	47.62	55.53	72.81	25.69	9.66	-	0.55
179	G045.0712+00.1321	288.3421	10.8480	192.8	288.3424	10.8486	323.20	-	3664.00	1935.00	901.10	306.60	120.50	-	8.39
180	G045.1223+00.1321	288.3665	10.8932	2984.3	288.3677	10.8947	1413.00	3847.00	2000.00	1737.00	1261.00	322.80	111.40	-	16.39

Table A.1. continued.

#	CORNISH name	$\alpha_{\text{CORNISH}}$ (deg)	$\delta_{\text{CORNISH}}$ (deg)	$S_5$ GHz (mJy)	$\alpha_{\text{HI-GAL}}$ (deg)	$\delta_{\text{HI-GAL}}$ (deg)	$S_{21\mu\text{m}}$ (Jy)	$S_{22\mu\text{m}}$ (Jy)	$S_{70\mu\text{m}}$ (Jy)	$S_{160\mu\text{m}}$ (Jy)	$S_{250\mu\text{m}}$ (Jy)	$S_{350\mu\text{m}}$ (Jy)	$S_{500\mu\text{m}}$ (Jy)	$S_{870\mu\text{m}}$ (Jy)	$S_{1100\mu\text{m}}$ (Jy)
181	G045.4545+00.0591	288.5888	11.1532	1081.0	288.5880	11.1542	497.60	3387.00	1738.00	808.60	471.30	174.90	59.89	—	14.29
182	G045.4656+00.0452	288.6070	11.1570	62.3	288.6066	11.1575	—	37.92	1468.00	1223.00	898.10	232.00	67.14	—	6.91
183	G045.4790+00.1294	288.5362	11.2066	504.2	288.5381	11.2076	172.70	—	240.70	219.10	263.60	—	—	—	9.46
184	G045.5431+00.0073	288.6906	11.2014	49.2	288.6906	11.2014	7.95	9.67	190.20	132.70	77.02	23.62	8.23	—	0.67
185	G048.6099+00.0270	290.1277	13.9284	131.2	290.1299	13.9239	31.11	—	1551.00	865.40	545.30	142.00	40.28	—	—
186	G048.9296+00.2793	290.5624	14.0669	185.4	290.5632	14.0676	34.85	—	294.90	235.20	—	56.37	68.47	—	—
187	G048.9901+00.2988	290.6088	14.1110	7.5	290.6094	14.1117	107.50	—	737.50	847.30	918.10	236.70	105.80	—	17.17
188	G049.2679+00.3374	290.7791	14.3377	102.6	290.7781	14.3369	4.94	9.91	432.60	804.40	869.70	310.90	112.80	—	11.08
189	G049.4891+00.3763	290.9227	14.5143	217.3	— <sup>a</sup>	— <sup>a</sup>	1658.00	—	1934.00	3583.00	1747.00	792.60	289.00	—	—
190	G049.4905+00.3688	290.9164	14.5193	3821.7	— <sup>a</sup>	— <sup>a</sup>	2687.90	—	8145.00	4770.00	1720.00	730.90	245.30	—	103.60
191	G050.2834+00.3904	291.3269	15.2078	156.8	291.3246	15.2071	60.79	94.40	1236.00	596.80	372.10	81.00	20.73	—	1.83
192	G050.3152+00.6762	290.3646	15.7392	154.6	290.3647	15.7389	38.42	54.81	581.40	394.50	257.10	60.28	18.63	—	—
193	G051.6785+00.7193	290.9951	16.9615	22.5	290.9949	16.9614	14.00	17.01	695.30	585.40	459.60	141.00	44.33	—	—
194	G052.7533+00.3340	291.8842	17.7241	386.0	291.8831	17.7228	18.78	26.63	97.21	213.40	129.50	38.40	14.10	—	1.04
195	G053.1865+00.2085	292.2180	18.0455	96.1	292.2177	18.0448	11.01	13.30	132.30	121.40	99.79	35.94	14.79	—	1.53
196	G053.9589+00.0320	292.7717	18.6380	46.0	292.7719	18.6380	31.88	36.66	248.40	215.60	168.10	51.48	16.97	—	1.34
197	G058.7739+00.6457	294.7027	23.1445	4.8	294.7031	23.1441	29.80	45.90	430.80	345.00	228.30	59.93	18.01	—	—
198	G059.6027+00.9118	294.8943	23.9970	68.8	294.8935	23.9968	8.34	10.04	589.30	493.90	369.20	89.41	27.51	—	—
199	G060.8838+00.1295	296.5866	24.5876	292.1	296.5833	24.5911	—	3269.00	1500.00	931.50	839.80	281.70	84.48	—	—
200	G060.8842+00.1286	296.5839	24.5915	18.7	296.5833	24.5912	286.60	45.02	1625.00	1122.00	976.50	315.20	113.20	—	18.59
201	G061.2875+00.3327	297.0004	24.8384	159.4	296.9973	24.8376	8.09	13.29	62.30	67.42	25.98	8.49	4.14	—	1.13
202	G061.4763+00.0892	296.7044	25.2122	785.6	296.7038	25.2138	589.50	—	4404.00	2758.00	1091.00	492.10	170.60	—	—
203	G061.7207+00.8630	296.0985	25.8121	101.3	296.0984	25.8119	19.44	23.72	253.30	141.30	90.73	24.83	7.87	—	—
204	G065.2462+00.3505	298.6068	28.5898	4.6	298.6053	28.5895	—	0.40	3.90	17.60	11.97	5.87	2.54	—	—

**Table A.2.** Distances, Lyman continuum photon rates, bolometric luminosities, and clump masses of the 200 HII regions of our sample for which a distance estimate was possible.

#	$d$ (kpc)	$\log_{10}N_{\text{Ly}}$ $\log_{10}(\text{s}^{-1})$	$\log_{10}L$ $\log_{10}(L_{\odot})$	$\log_{10}M_{\text{gas}}$ $\log_{10}(M_{\odot})$
1	12.6 <sup>a</sup>	47.71	4.70	3.53
2	4.0	46.46	3.83	2.79
3	10.9	47.83	5.79	4.78
4	4.9	48.78	5.37	4.23
5	13.7	48.56	5.35	3.78
6	3.0	46.66	3.43	2.22
7	2.7	45.62	2.99	1.45
8	14.3	48.32	5.23	3.57
9	16.9	48.94	5.56	4.22
10	12.8 <sup>a</sup>	48.22	4.48	3.18
11	4.2	46.86	3.97	2.92
12	12.5	49.16	5.48	3.57
14	11.8	47.94	5.05	3.63
15	13.3	48.56	5.43	4.53
16	13.8	47.93	4.52	4.09
17	4.2	47.08	4.36	3.14
18	2.0	45.92	3.34	2.33
19	4.7	48.31	4.25	3.28
20	2.1	47.42	3.43	2.04
21	4.5	48.46	4.97	3.37
22	14.7 <sup>a</sup>	48.01	4.60	3.54
23	2.8	46.44	3.19	2.38
24	13.0	47.48	4.49	3.23
25	12.3	47.34	4.53	3.27
26	12.2 <sup>a</sup>	48.26	4.28	3.08
27	16.9	49.16	5.43	3.44
28	10.4	46.76	4.18	3.13
29	10.4 <sup>a</sup>	47.26	4.51	2.91
30	14.0	47.14	4.35	3.30
31	13.7 <sup>a</sup>	47.29	4.34	3.11
32	4.3	48.19	4.11	2.97
33	3.1	48.08	4.55	3.09
34	11.9	48.06	4.53	3.38
35	12.0	48.69	5.38	3.77
36	12.5 <sup>a</sup>	48.23	4.40	3.26
37	13.4 <sup>a</sup>	48.28	4.81	3.57
38	14.0	48.00	4.85	3.86
39	4.6	46.38	3.89	2.78
40	12.5	48.31	5.05	3.38
41	11.3	46.91	4.23	3.33
42	4.7	48.05	4.74	3.48
43	13.7	48.88	5.14	3.73
44	13.0	48.11	4.92	3.42
45	12.5	49.65	6.14	4.59
46	11.8	48.23	4.67	3.00
47	4.4	46.70	3.77	2.49
48	14.0	48.67	4.63	3.38
49	9.2	47.48	4.91	3.13
50	12.6	48.90	5.65	4.30
51	4.0	46.94	3.58	2.52
52	17.4	47.48	4.72	3.16
53	11.6	47.13	4.96	3.06
54	13.1	47.28	4.45	3.02
55	10.2	47.41	4.70	3.08
56	10.2	48.07	5.05	3.65
57	4.1	47.19	4.19	2.65
58	16.1	47.71	4.47	3.10
59	13.7	49.02	5.23	3.73
60	5.0	46.39	3.93	3.06

**Notes.** The sequential number identifying each source is the same as in Table A.1. <sup>(a)</sup> KDA not solved: far kinematic distance adopted (see Sect. 3.2).

**Table A.2.** continued.

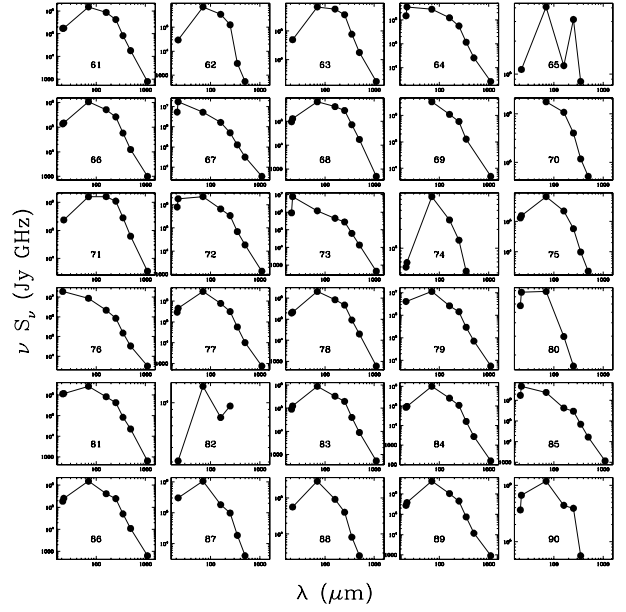
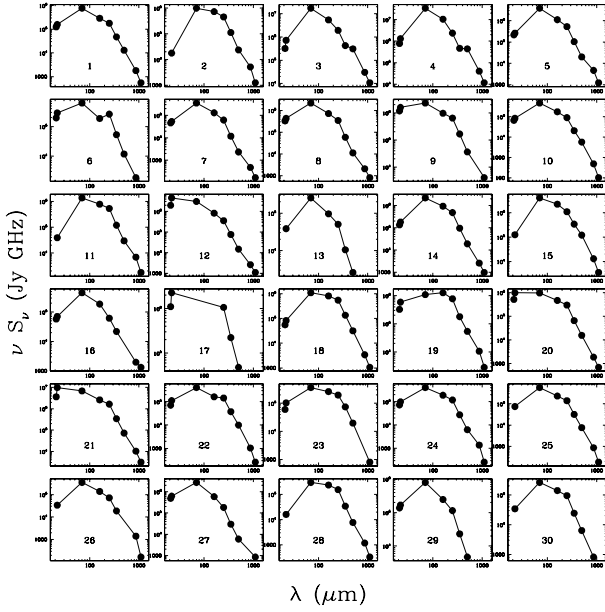
#	$d$ (kpc)	$\log_{10}N_{\text{Ly}}$ $\log_{10}(\text{s}^{-1})$	$\log_{10}L$ $\log_{10}(L_{\odot})$	$\log_{10}M_{\text{gas}}$ $\log_{10}(M_{\odot})$
61	5.0	47.34	4.20	2.86
62	6.2	46.74	3.97	1.54
63	5.3	46.36	3.99	2.91
64	6.7	47.96	4.91	3.27
65	10.7	47.65	4.34	3.61
66	12.5	47.82	4.83	3.49
67	5.1	48.47	5.09	3.11
68	7.8	46.35	4.30	3.22
69	6.1	47.31	4.41	3.96
70	6.1	47.68	4.27	3.49
71	6.5	47.76	4.60	3.62
72	6.0	47.86	4.62	3.03
73	6.5	46.92	4.83	2.97
74	3.3	47.27	3.42	2.29
75	14.1 <sup>a</sup>	48.00	4.70	2.87
76	4.1	48.03	5.03	2.95
77	16.9	48.92	5.45	3.67
78	13.9	48.52	5.17	3.79
79	5.8	48.85	5.18	3.59
80	9.4	47.26	4.60	3.29
81	5.7	47.02	4.59	3.08
83	12.9	47.28	4.75	3.38
84	12.9	46.89	4.71	2.86
85	9.8	48.60	5.20	3.41
86	13.2	48.08	4.97	3.49
87	7.6	48.06	4.33	2.57
89	13.0	47.52	5.34	3.51
90	12.6	48.83	4.98	3.57
91	9.5	47.73	5.06	4.24
92	9.8	48.19	4.38	3.48
93	11.9	46.80	4.81	3.43
94	4.8	47.45	4.18	2.93
95	6.0	48.03	5.12	3.88
96	8.3	47.63	4.37	2.89
97	11.6	48.86	5.85	4.01
98	6.0	47.08	3.85	2.50
99	16.4	48.03	4.60	3.28
100	8.5	48.18	5.00	3.43
101	8.4	48.20	4.65	3.54
102	9.6	47.98	4.52	2.82
103	8.5	49.35	6.13	4.18
104	7.9	46.44	4.29	3.35
105	10.1	47.99	4.58	3.16
106	11.3	48.03	5.10	3.58
107	11.3	48.95	5.27	3.58
108	11.6	48.09	5.34	3.92
109	8.4	48.32	4.95	4.69
110	6.6	47.06	4.26	3.01
111	11.8	48.65	5.41	3.84
112	11.7	47.54	4.89	3.52
113	12.1	47.30	4.36	3.33
114	13.2	47.30	4.68	3.07
115	11.8	48.53	4.58	3.26
116	2.8	46.39	3.44	2.21
117	12.9	49.05	5.41	3.65
118	7.3	48.15	5.03	3.95
119	5.7	47.41	4.99	3.29
120	6.4	48.59	5.01	4.13
121	6.4	46.77	4.62	3.50
122	7.2	47.14	4.22	2.81
123	6.4	48.34	4.79	3.53
124	12.6	48.69	4.87	3.35
125	10.9	48.06	4.78	3.28
126	12.8	46.74	4.20	3.50
127	11.6	47.24	4.47	3.45

Table A.2. continued.

#	$d$ (kpc)	$\log_{10}N_{\text{Ly}}$ $\log_{10}(\text{s}^{-1})$	$\log_{10}L$ $\log_{10}(L_{\odot})$	$\log_{10}M_{\text{gas}}$ $\log_{10}(M_{\odot})$
128	13.1	49.72	6.04	4.53
129	19.0	49.01	5.26	3.45
130	9.2	48.50	4.93	3.69
131	9.3	47.81	4.44	3.27
132	10.9	48.10	5.24	3.30
133	10.9	48.09	5.24	3.30
134	7.1	48.62	5.21	3.91
135	11.6	47.11	4.52	2.92
136	11.5	48.75	5.11	3.45
137	10.1	47.02	4.70	3.39
138	3.9	46.12	4.04	3.23
139	16.5	47.73	4.59	3.13
140	10.4	47.08	5.35	3.72
141	10.4	47.86	4.76	3.25
142	9.5 <sup>a</sup>	46.83	4.02	2.91
143	8.5	48.36	5.33	3.77
144	10.4	48.48	4.99	3.84
145	10.2	48.28	5.41	3.61
146	4.0	46.70	4.16	2.70
147	9.8	48.59	5.12	3.47
148	10.2	47.22	4.64	3.49
149	12.1	47.71	4.44	3.04
150	9.2	48.45	4.37	3.77
151	12.1	47.82	4.89	3.48
152	9.9	48.31	4.78	3.25
153	9.2	49.33	5.59	3.85
154	16.6	47.76	4.25	2.87
155	4.9	46.44	3.70	2.26
156	17.1	47.35	4.63	3.43
157	9.7	47.27	4.50	3.30
158	14.7	48.82	5.02	3.32
159	15.7	48.18	4.83	2.99
160	8.8	48.00	4.18	2.98
161	8.9	48.34	4.77	3.29
162	12.0	47.20	4.93	3.30
163	11.7	48.49	4.89	3.01
164	8.5	47.03	4.61	3.07
165	5.3	47.37	4.46	2.38
166	12.1	49.03	5.70	3.76
167	11.4	49.54	6.01	4.39
168	12.2	49.70	6.30	4.51
169	12.2	48.51	5.57	4.30
170	11.5	48.32	5.02	4.08
171	8.0	48.06	4.69	3.38
172	11.9	48.40	5.27	3.92
173	4.8	46.65	4.37	2.99
174	9.0	47.44	5.44	3.95
175	4.2	47.97	4.40	3.01
176	14.0	47.90	4.61	2.83
177	7.5	46.48	4.68	3.18
178	18.2	47.14	4.55	3.49
179	5.0	47.67	5.17	3.46
180	5.1	48.89	5.46	3.45
181	6.9	48.71	5.64	3.44
182	6.6	47.42	4.97	3.45
183	6.0	48.25	4.49	3.65
184	7.0	47.38	4.16	2.60
185	9.8	48.10	5.28	3.58

Table A.2. continued.

#	$d$ (kpc)	$\log_{10}N_{\text{Ly}}$ $\log_{10}(\text{s}^{-1})$	$\log_{10}L$ $\log_{10}(L_{\odot})$	$\log_{10}M_{\text{gas}}$ $\log_{10}(M_{\odot})$
186	5.6	47.76	4.24	3.32
187	5.6	46.37	4.72	3.50
188	5.6	47.49	4.46	3.53
189	5.5	47.82	5.40	3.93
190	5.5	49.06	5.78	3.86
191	9.5	48.15	5.23	3.26
192	8.8	48.07	4.88	3.14
193	10.2	47.37	5.03	3.65
194	9.0	48.49	4.38	3.04
195	9.9	47.97	4.40	3.15
196	5.0	47.06	4.10	2.61
197	4.4	45.96	4.19	2.53
198	4.3	47.10	4.18	2.69
199	5.8 <sup>a</sup>	47.98	5.44	3.44
200	2.5	46.06	4.16	2.84
201	9.6	48.17	4.12	2.57
202	4.1	48.11	5.13	3.43
203	15.7	48.39	5.01	3.27



**Fig. A.1.** Spectral energy distributions of the CORNISH HII regions with Hi-GAL counterparts of at least three bands. In addition to Hi-GAL, the MSX 21  $\mu\text{m}$ , WISE 22  $\mu\text{m}$ , ATLASGAL 870  $\mu\text{m}$ , and BGPS 1.1 mm flux densities have also been used. The number in each box identifies the source according to the numbering in Table A.1.

**Fig. A.1.** continued.

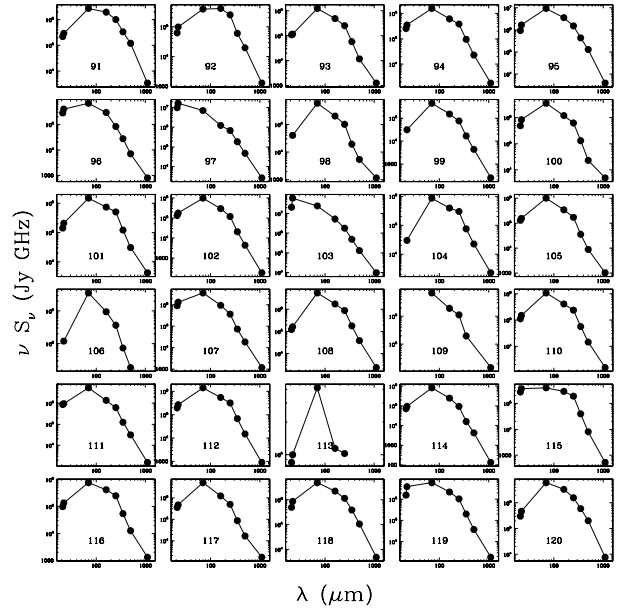
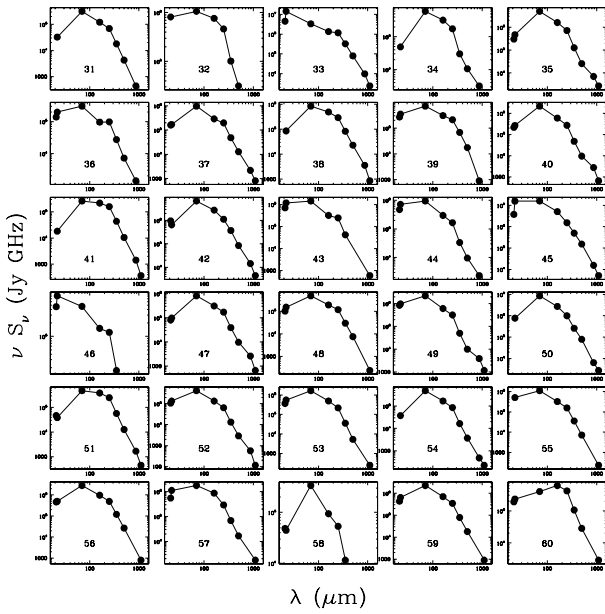


**Fig. A.1.** continued.

**Fig. A.1.** continued.

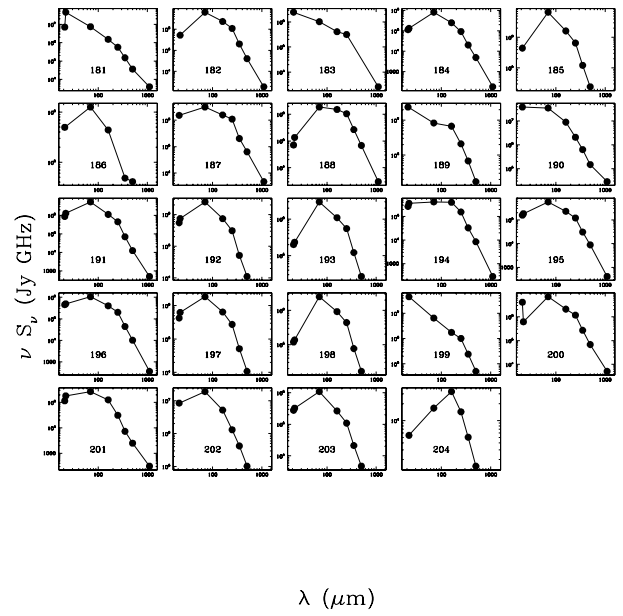
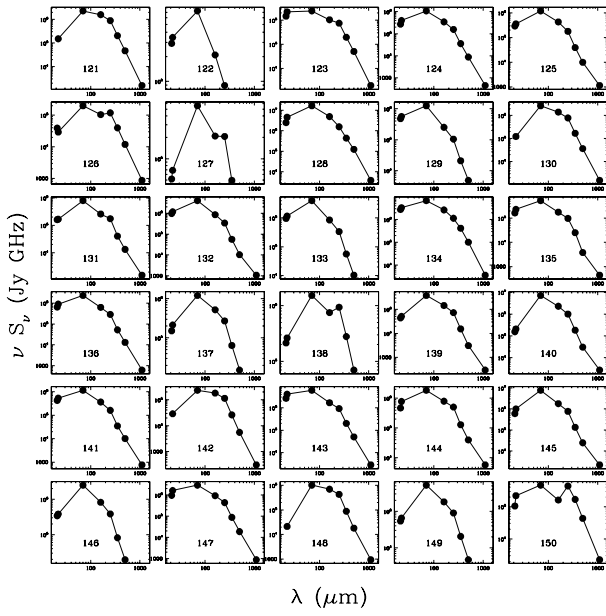


Fig. A.1. continued.

Fig. A.1. continued.

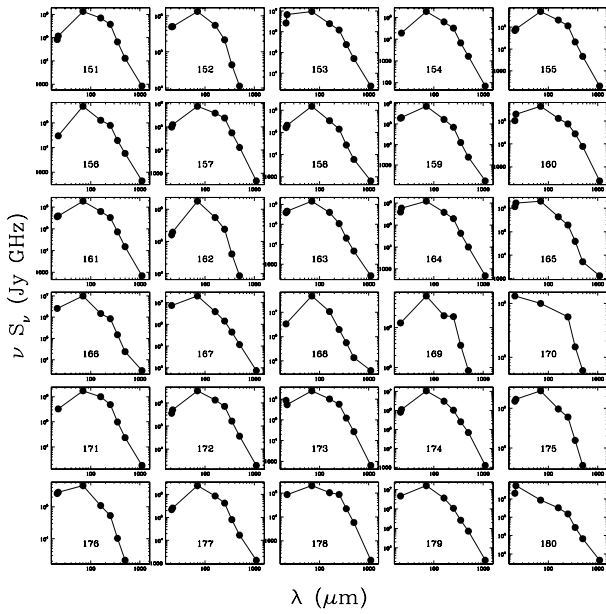
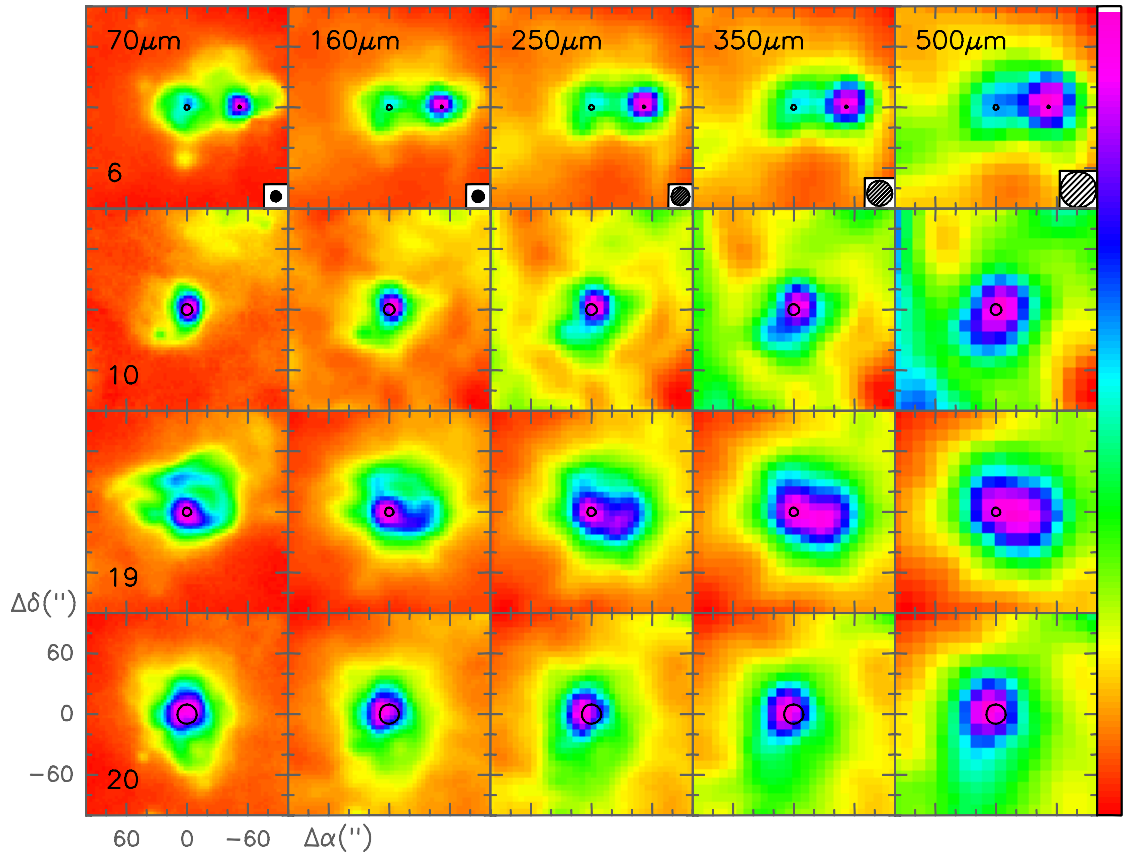
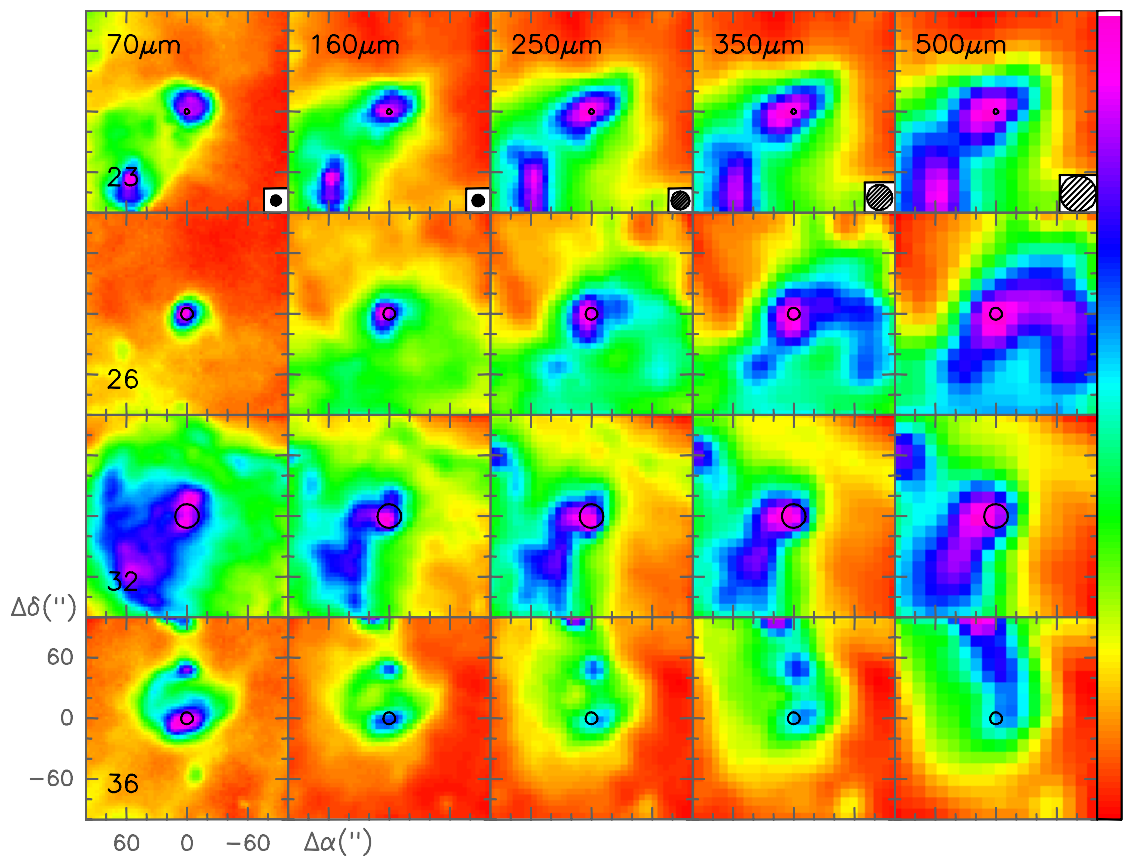


Fig. A.1. continued.



**Fig. A.2.** Hi-GAL images of the sources lying above the blackbody curve in Fig. 5. The sources are identified by the numbers in Col. 1 of Table A.1. The black circles represent the CORNISH HII regions in the field of view, with diameter equal to the angular size given in Col. 8 of Table 3 in Purcell et al. (2013). The HPBW at each wavelength is shown in the bottom right of the top panels.



**Fig. A.2.** continued.

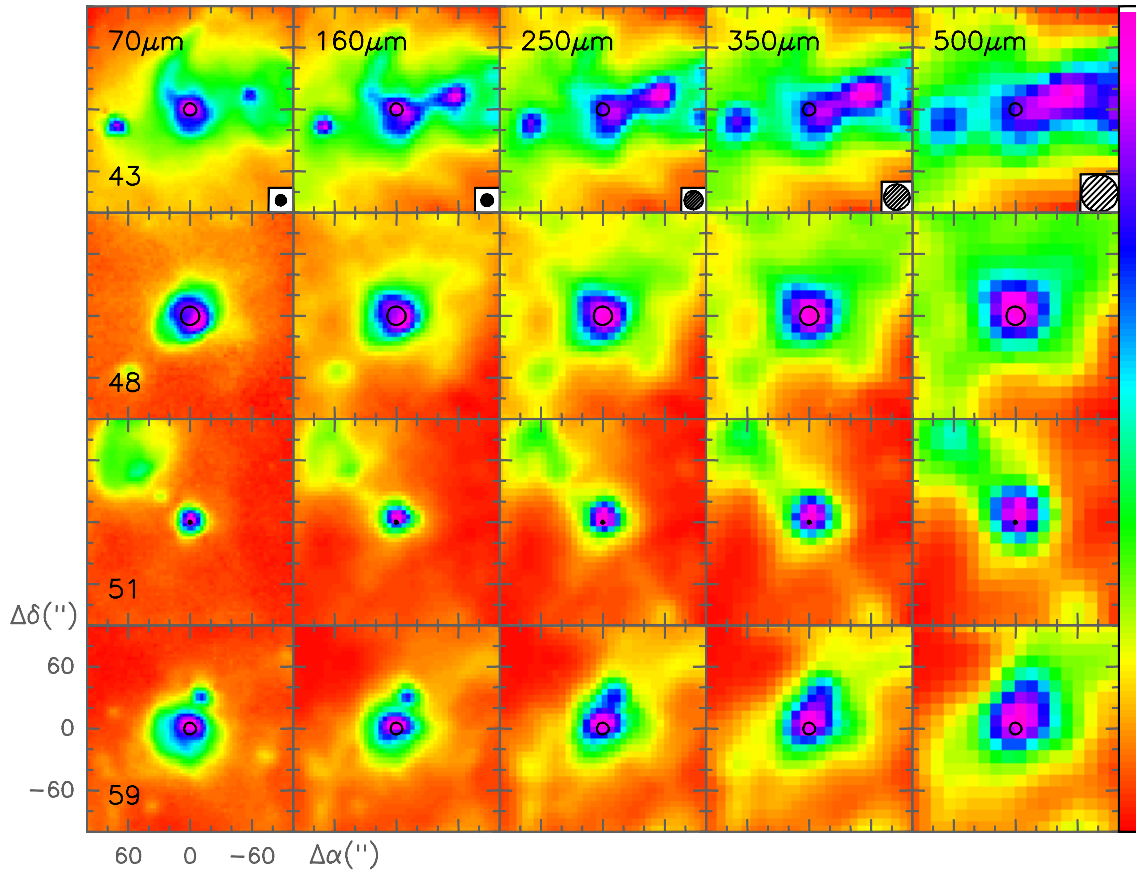


Fig. A.2. continued.

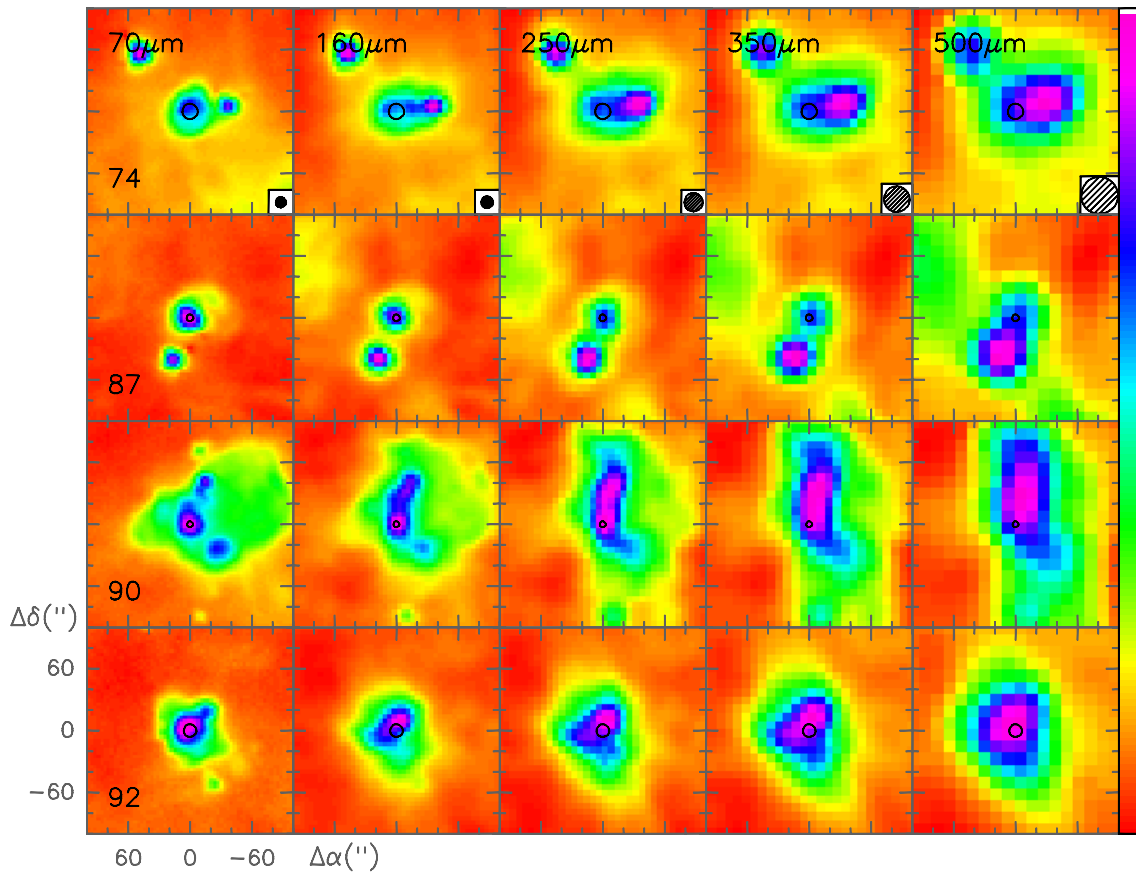


Fig. A.2. continued.

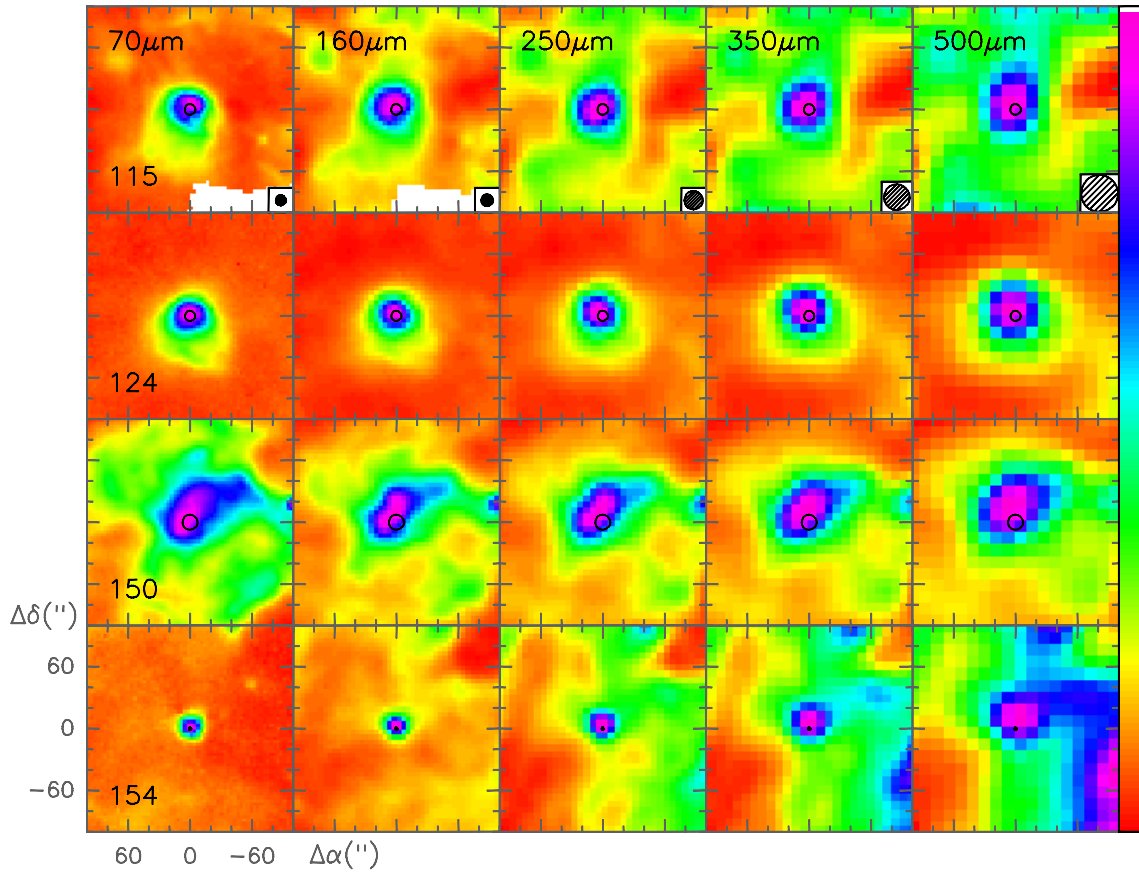


Fig. A.2. continued.

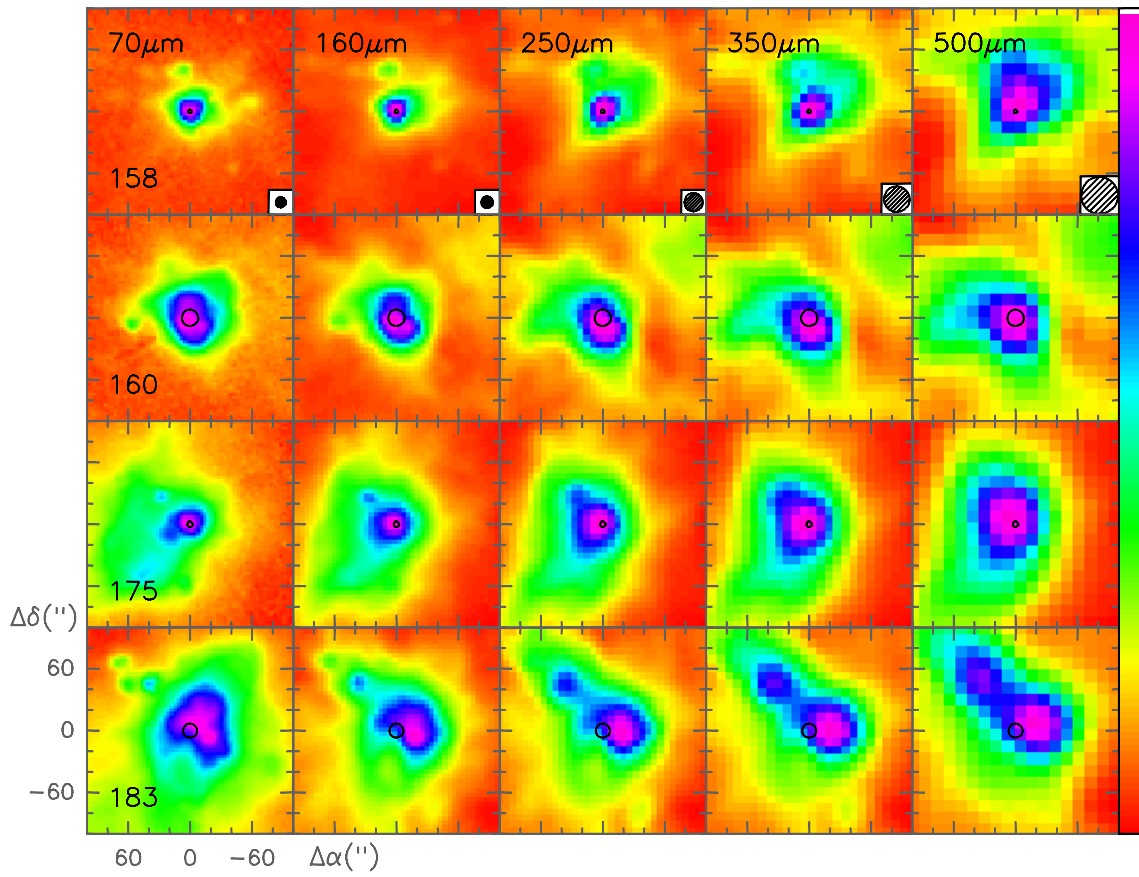


Fig. A.2. continued.

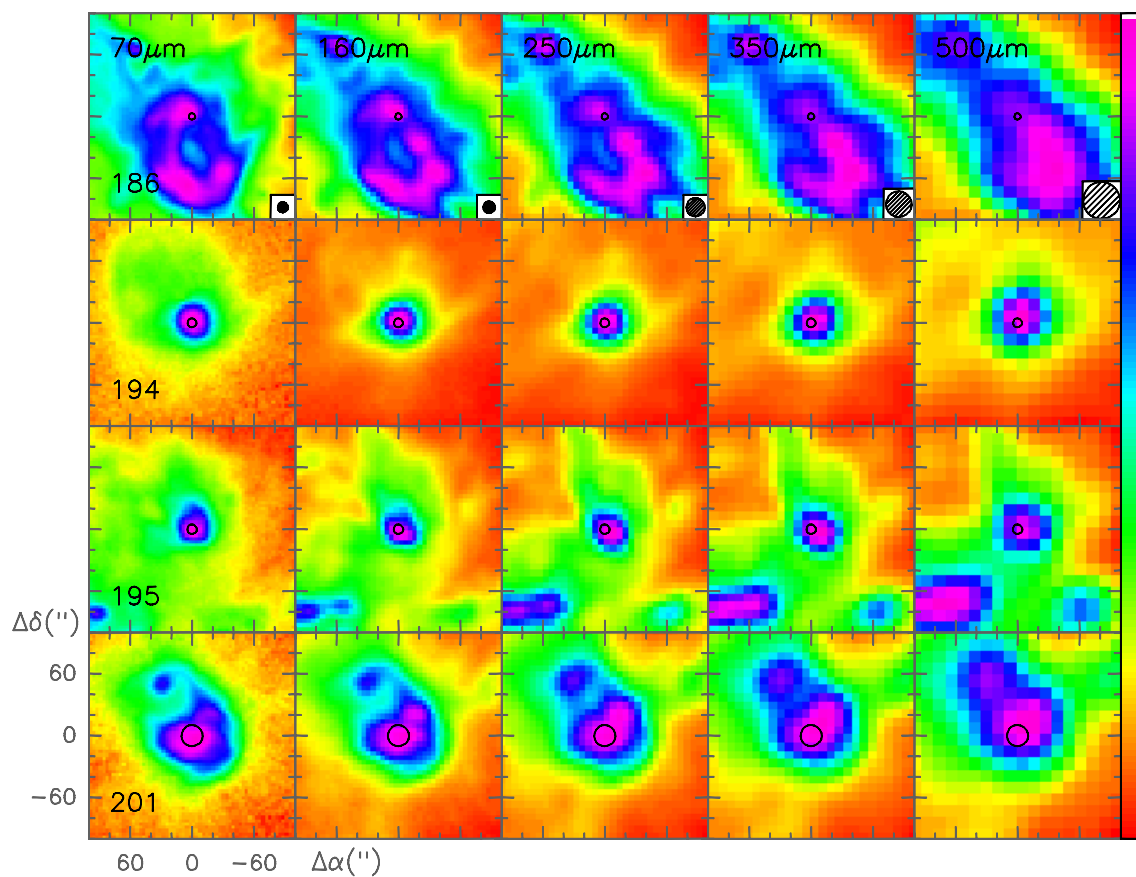


Fig. A.2. continued.

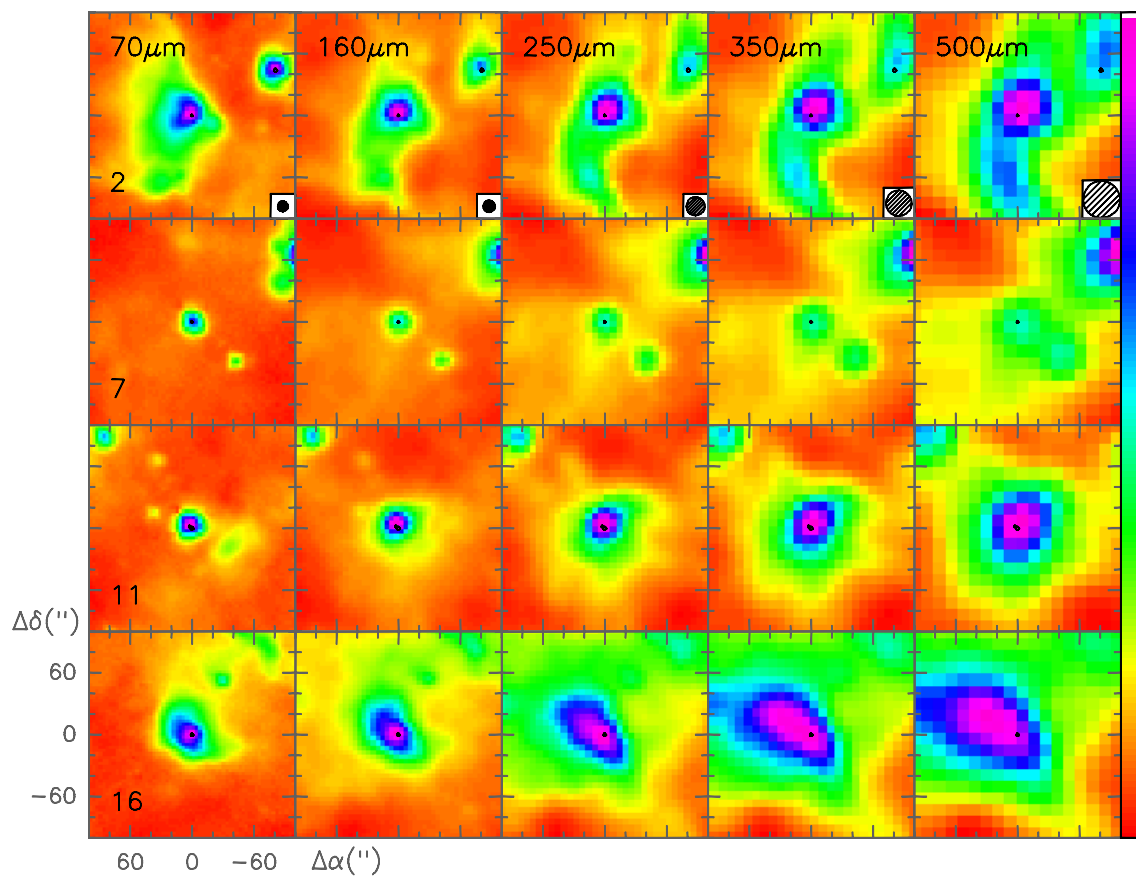


Fig. A.3. Same as Fig. A.2 for the sources lying between the blackbody curve (dashed line) and the single ZAMS star curve (solid line) in Fig. 5.

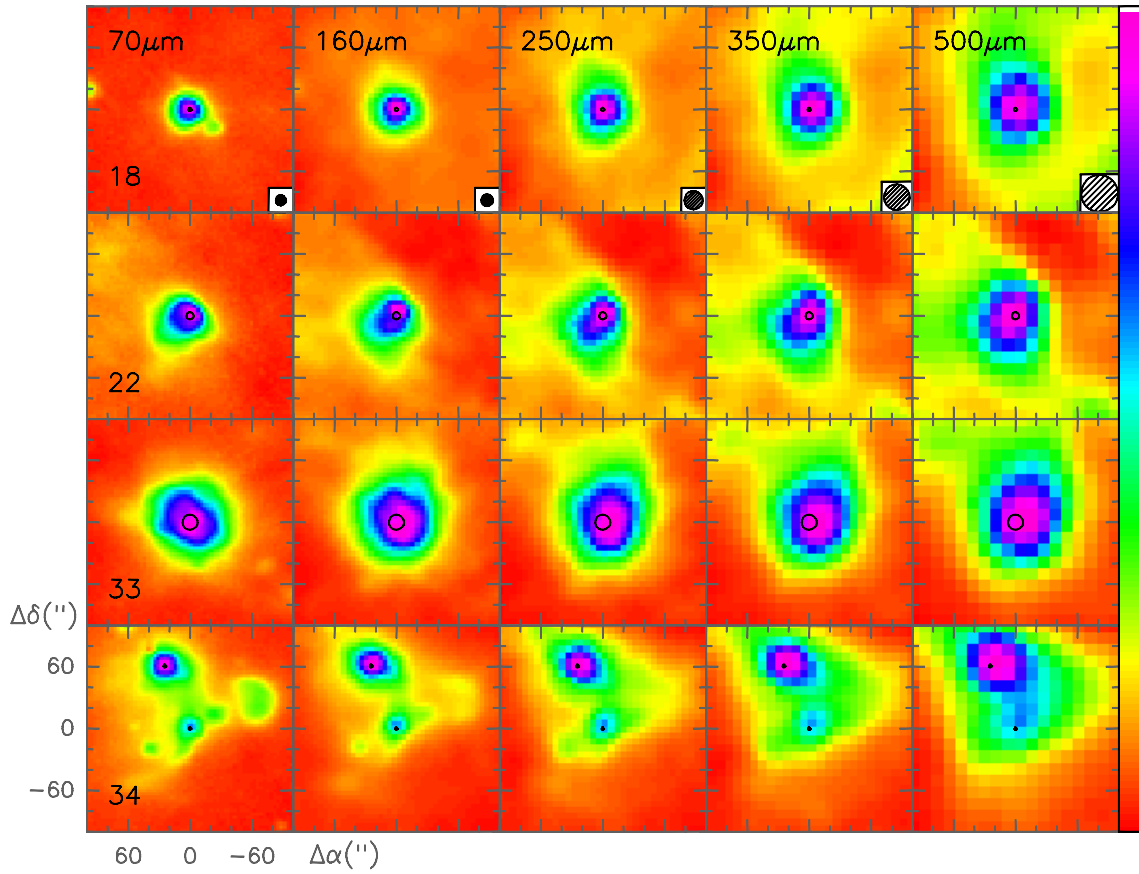


Fig. A.3. continued.

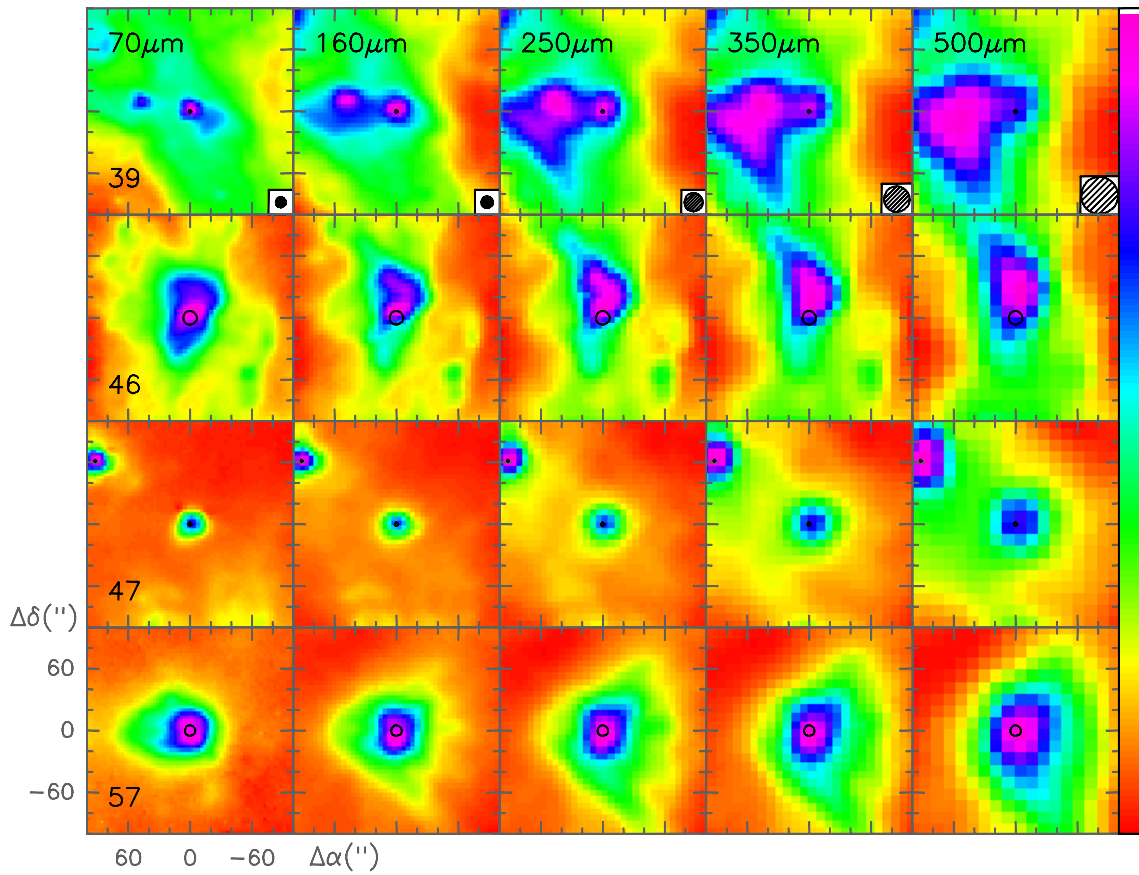


Fig. A.3. continued.

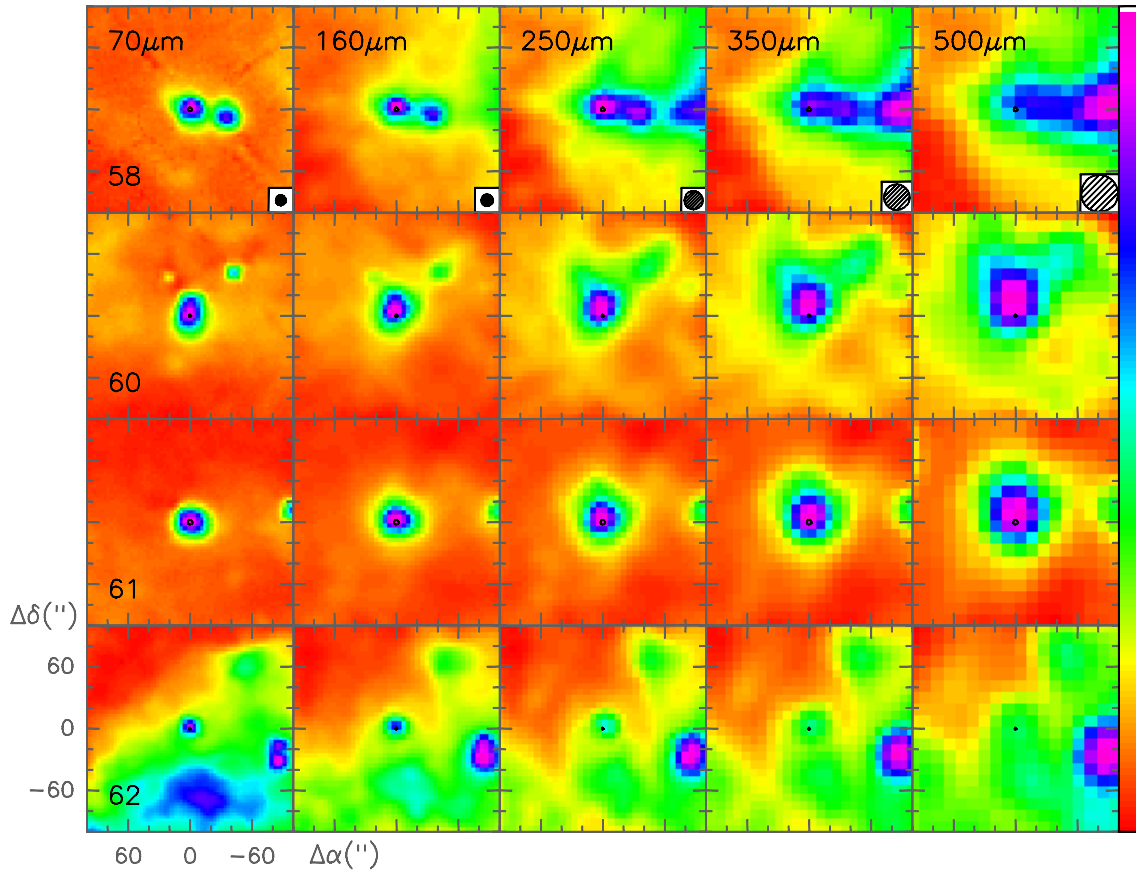


Fig. A.3. continued.

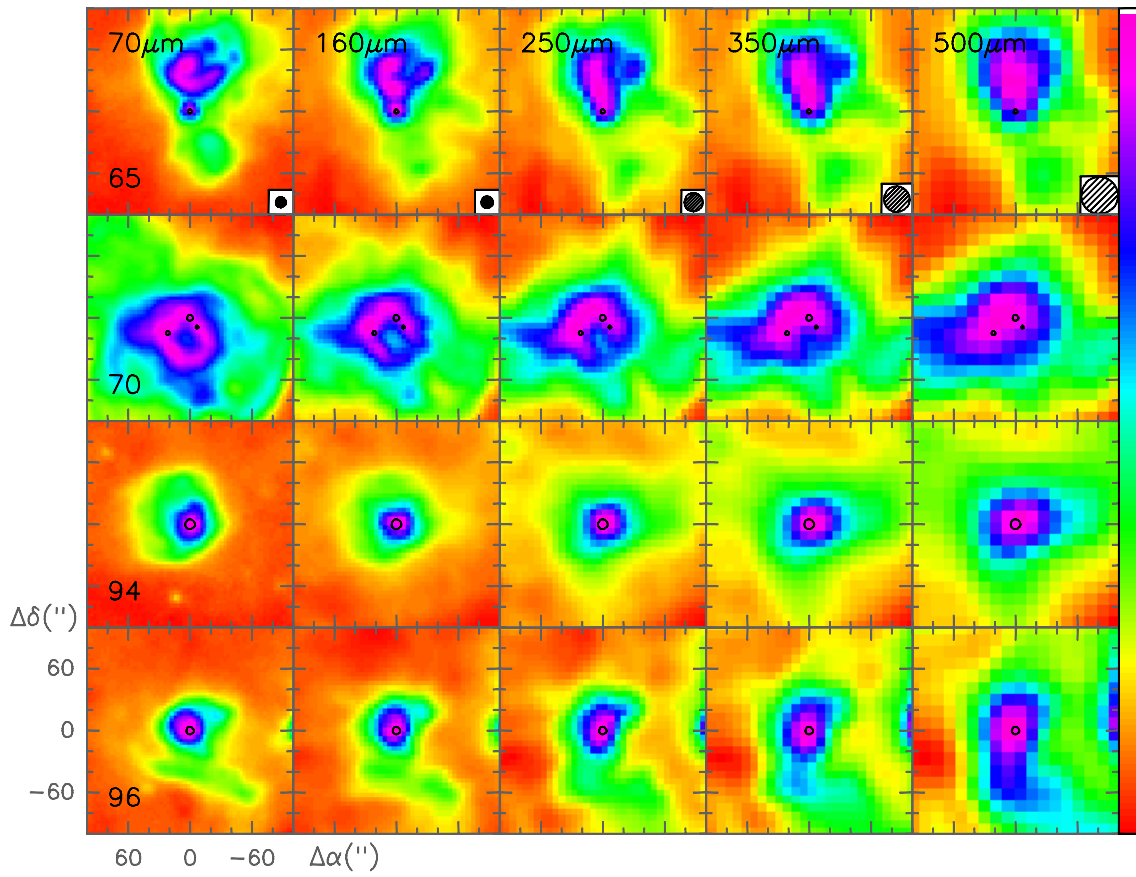


Fig. A.3. continued.

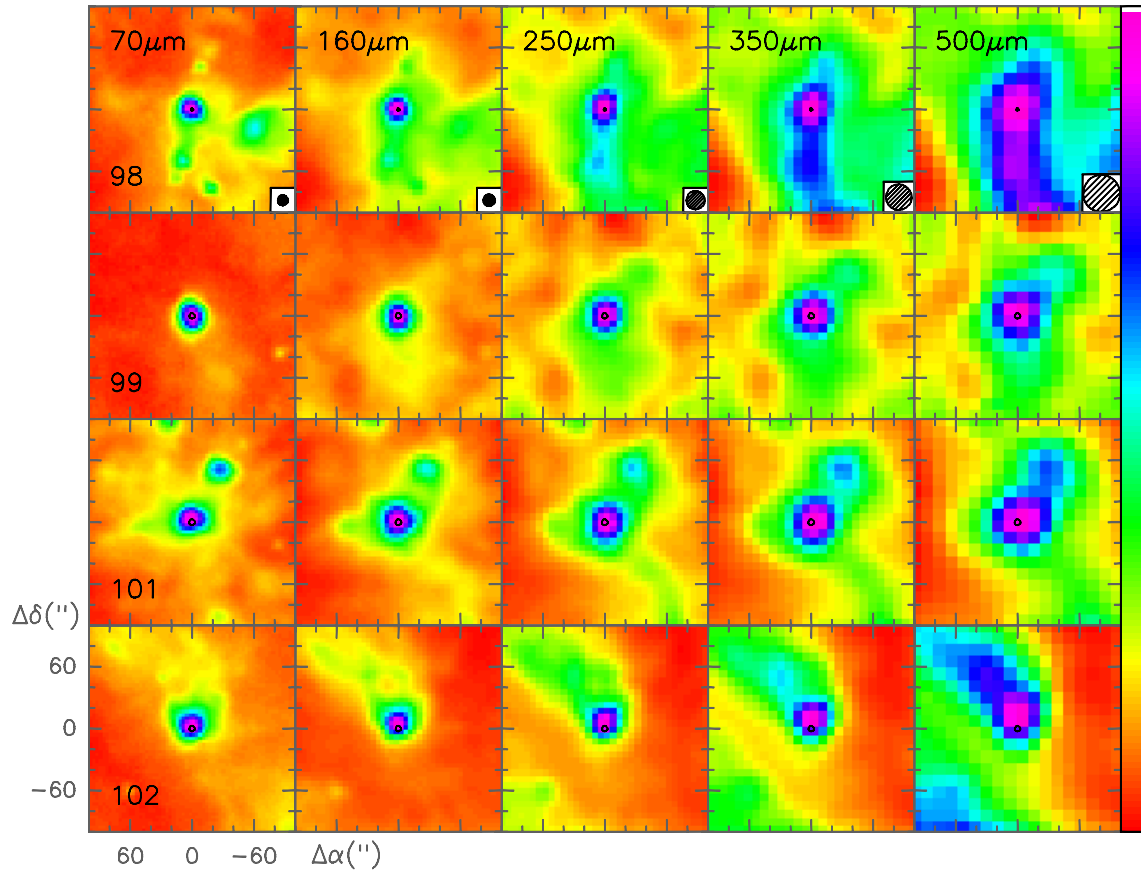


Fig. A.3. continued.

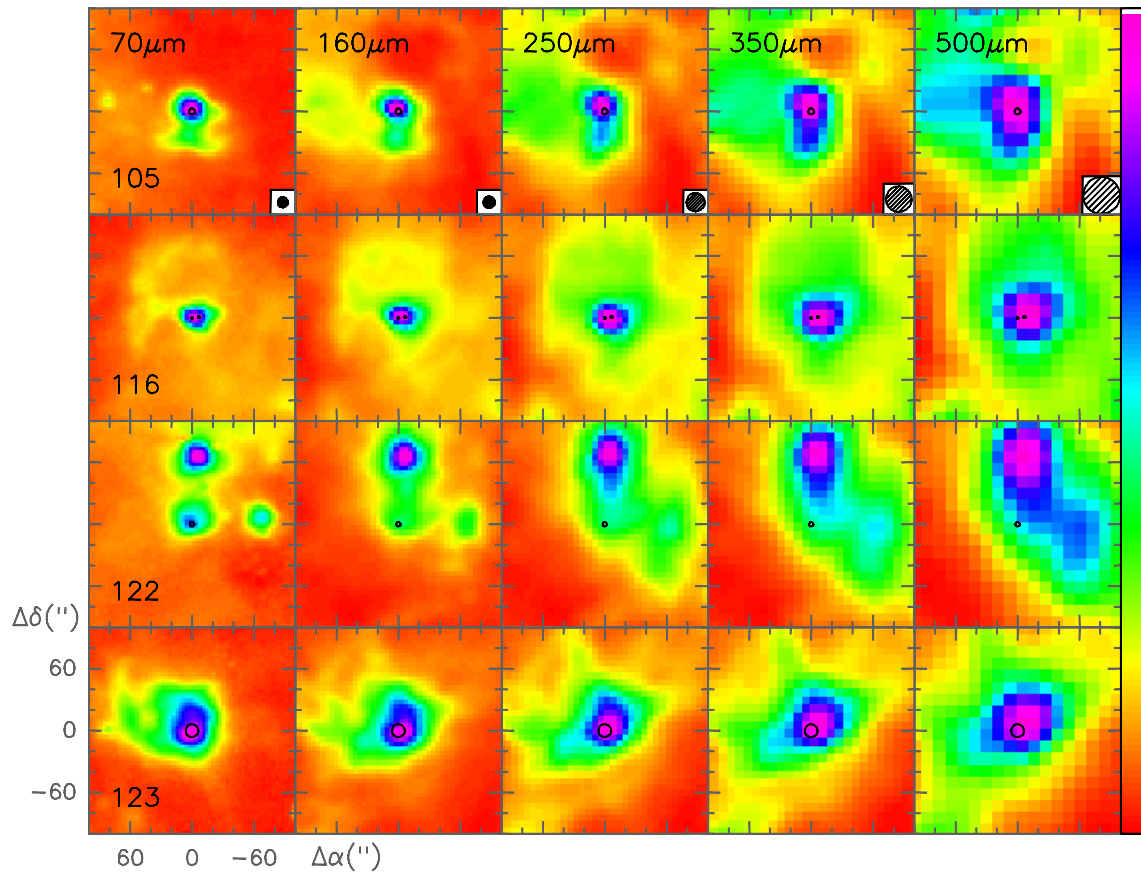


Fig. A.3. continued.

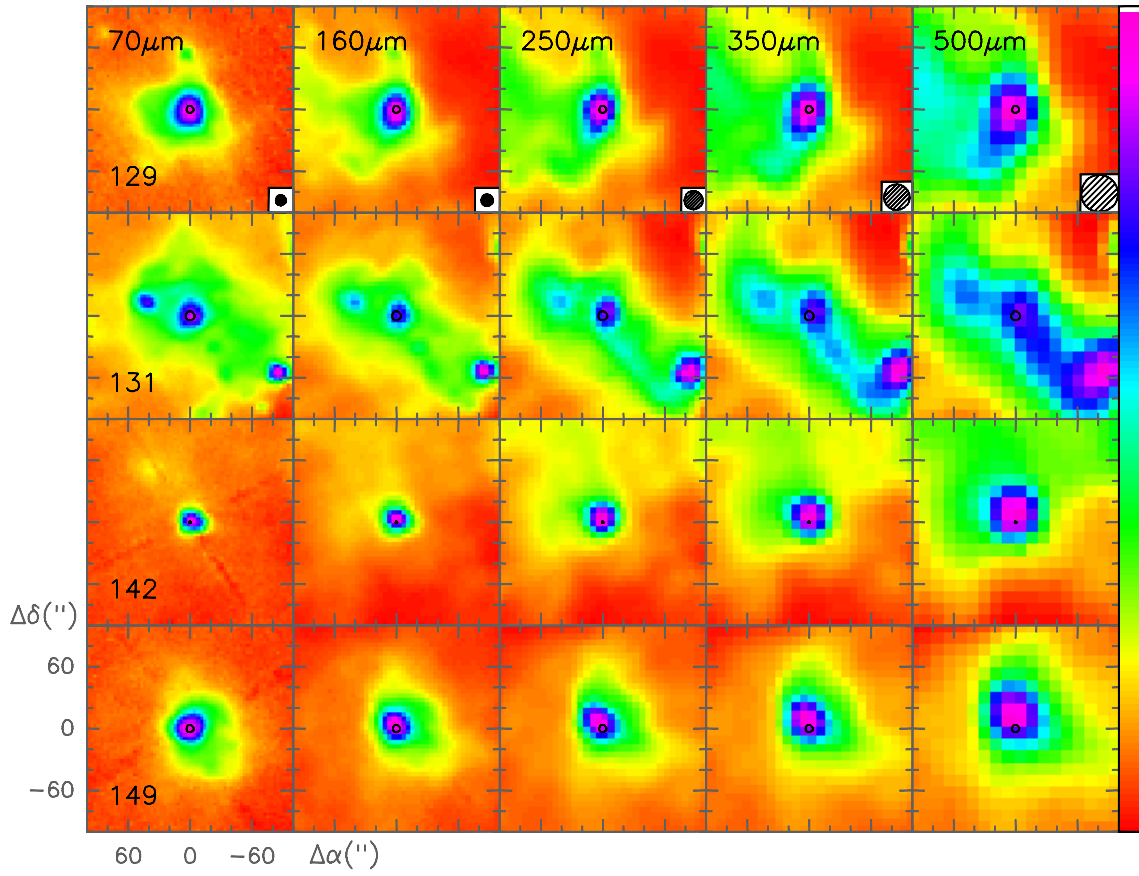


Fig. A.3. continued.

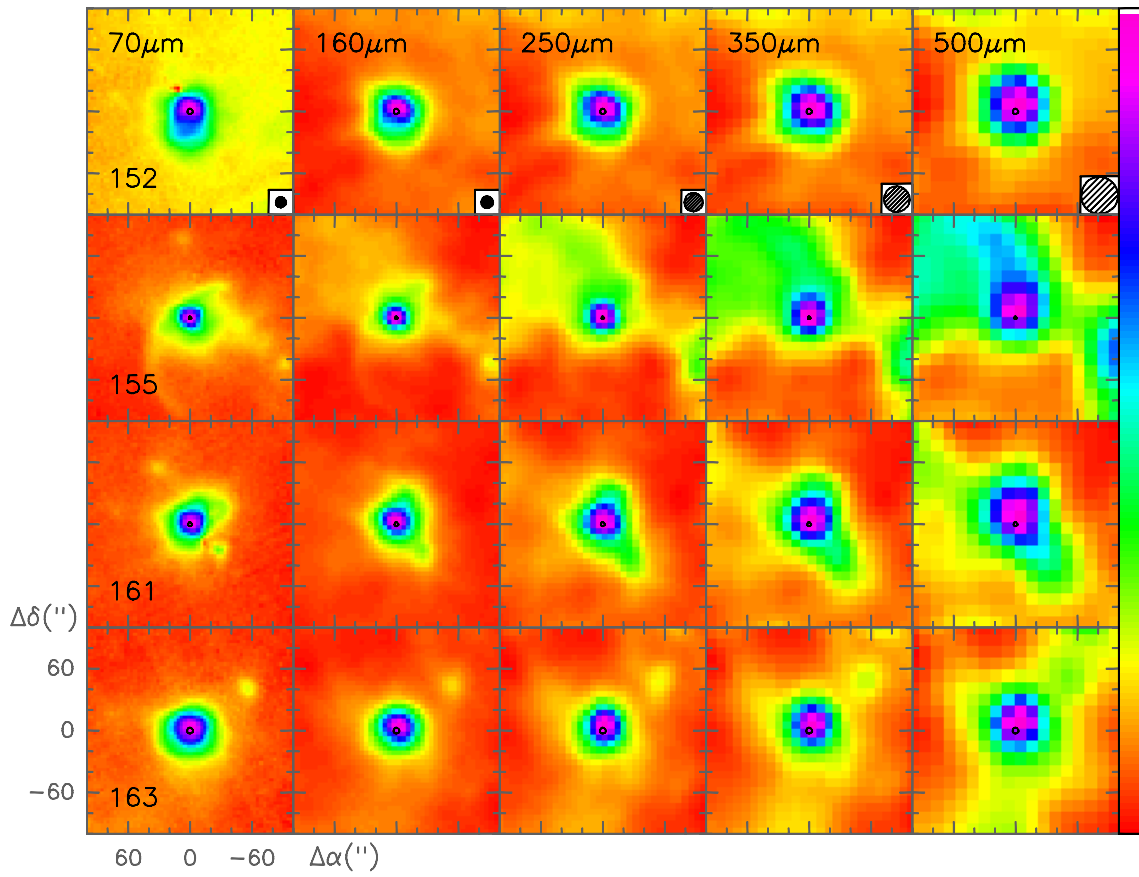


Fig. A.3. continued.

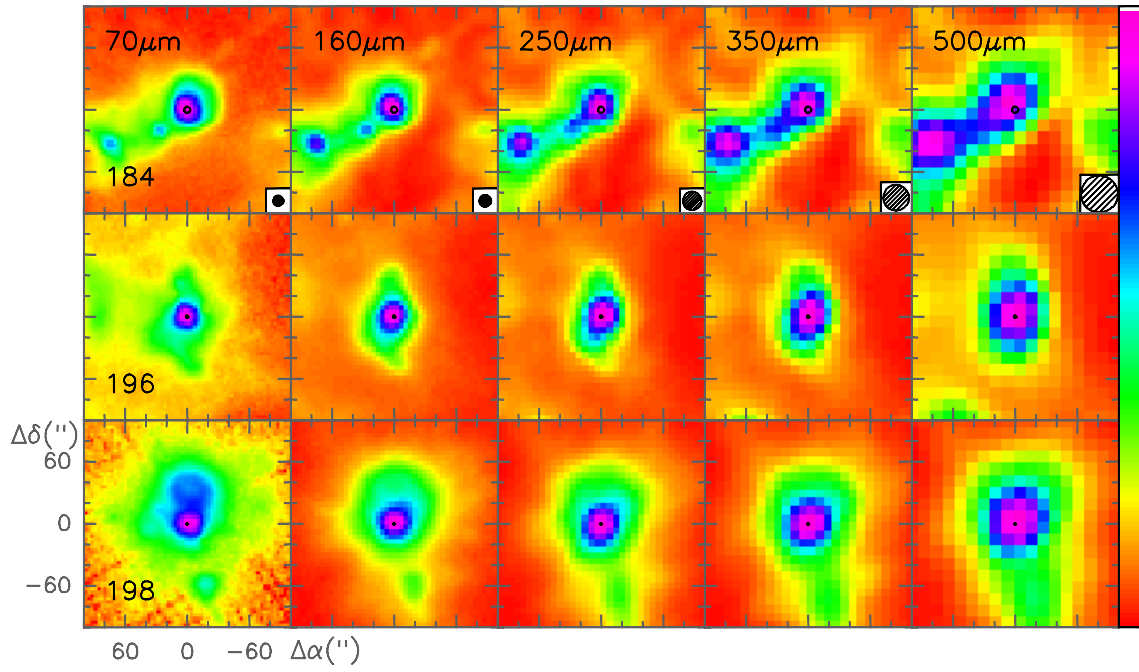


Fig. A.3. continued.

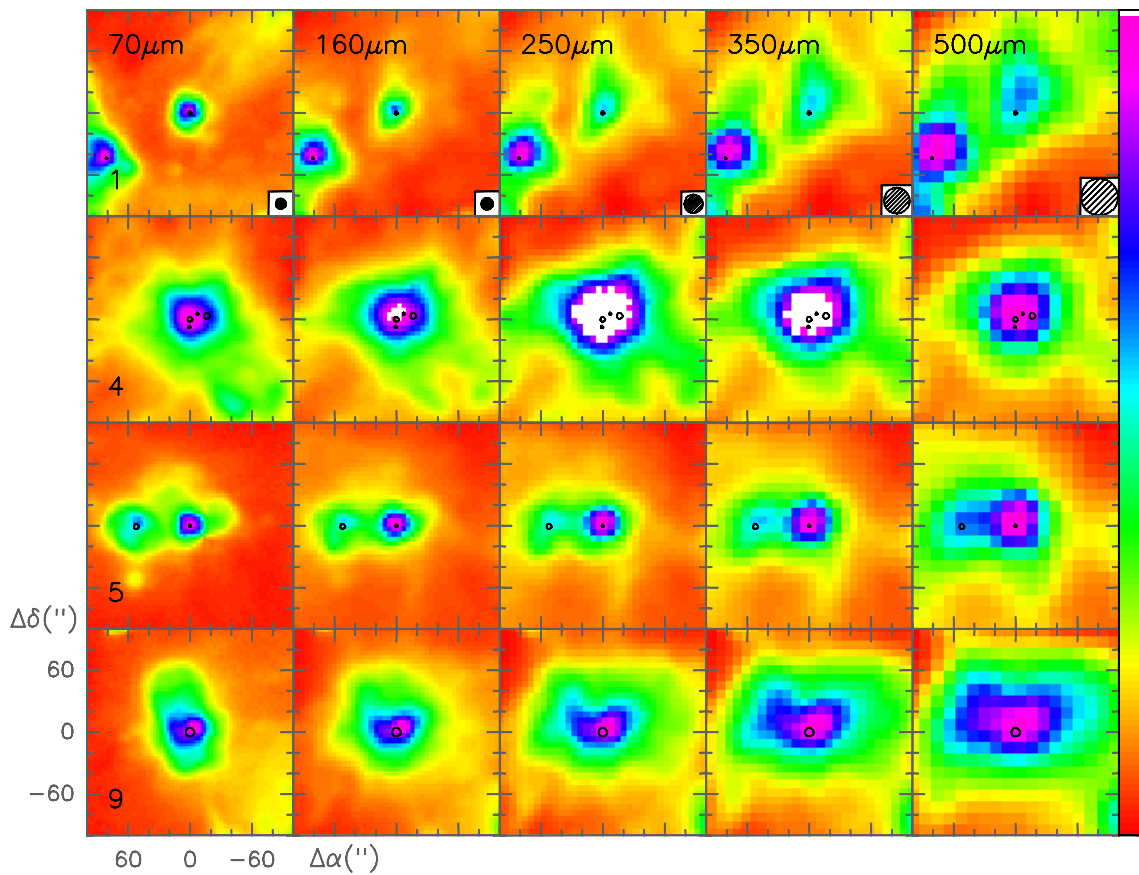


Fig. A.4. Same as Fig. A.2 for the sources lying inside the cluster region (hatched area) in Fig. 5.

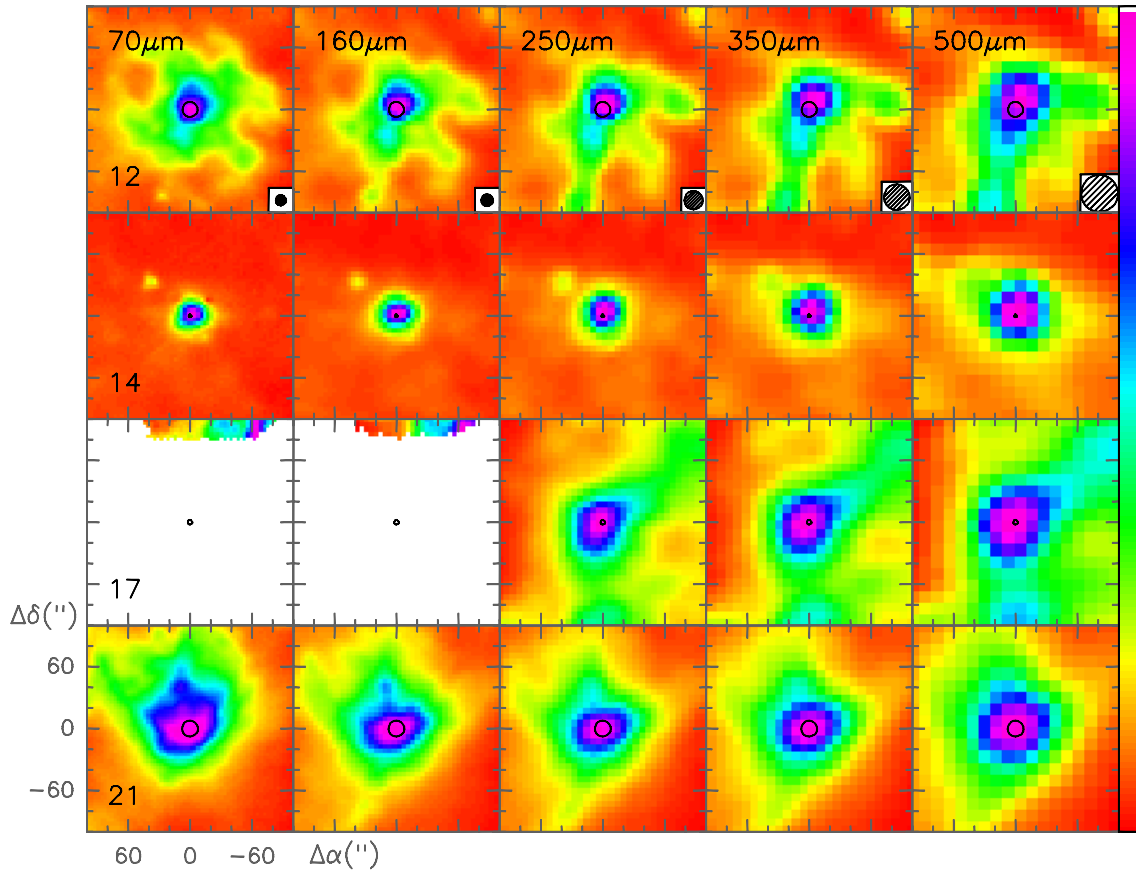


Fig. A.4. continued.

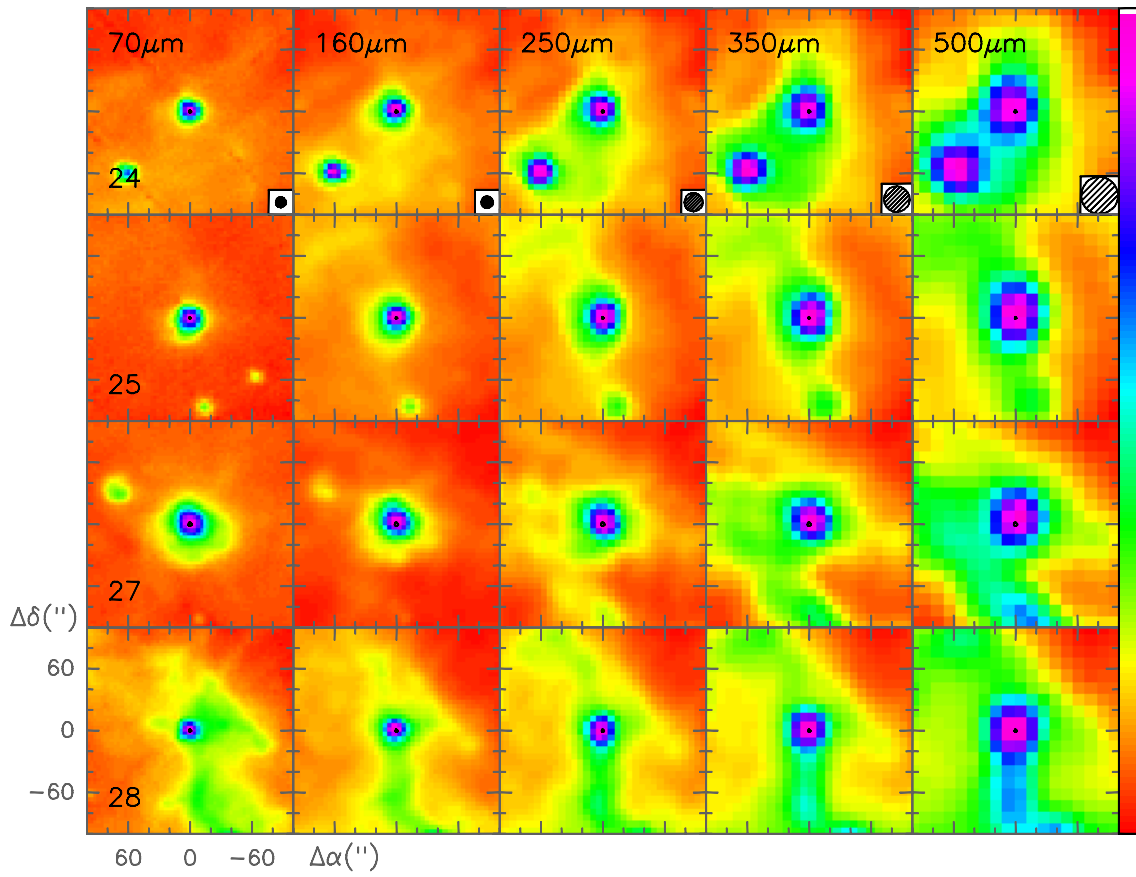


Fig. A.4. continued.

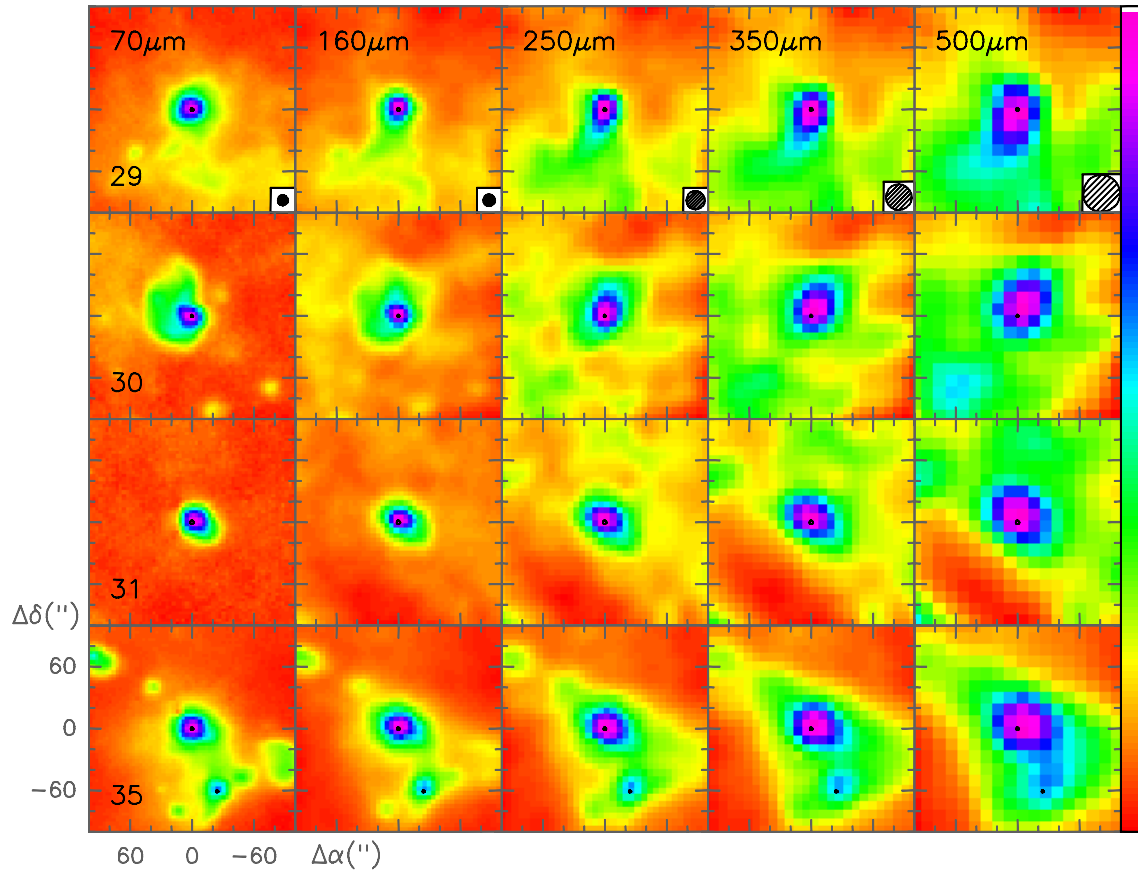


Fig. A.4. continued.

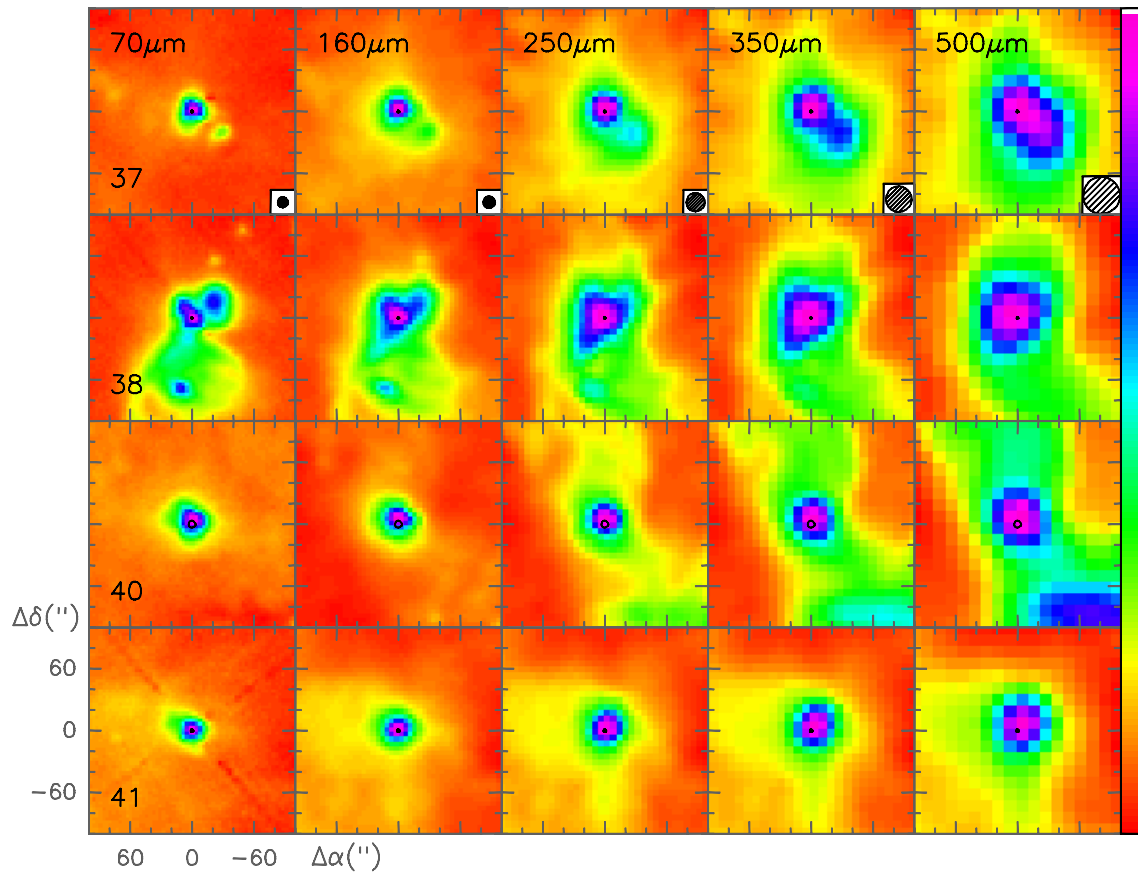


Fig. A.4. continued.

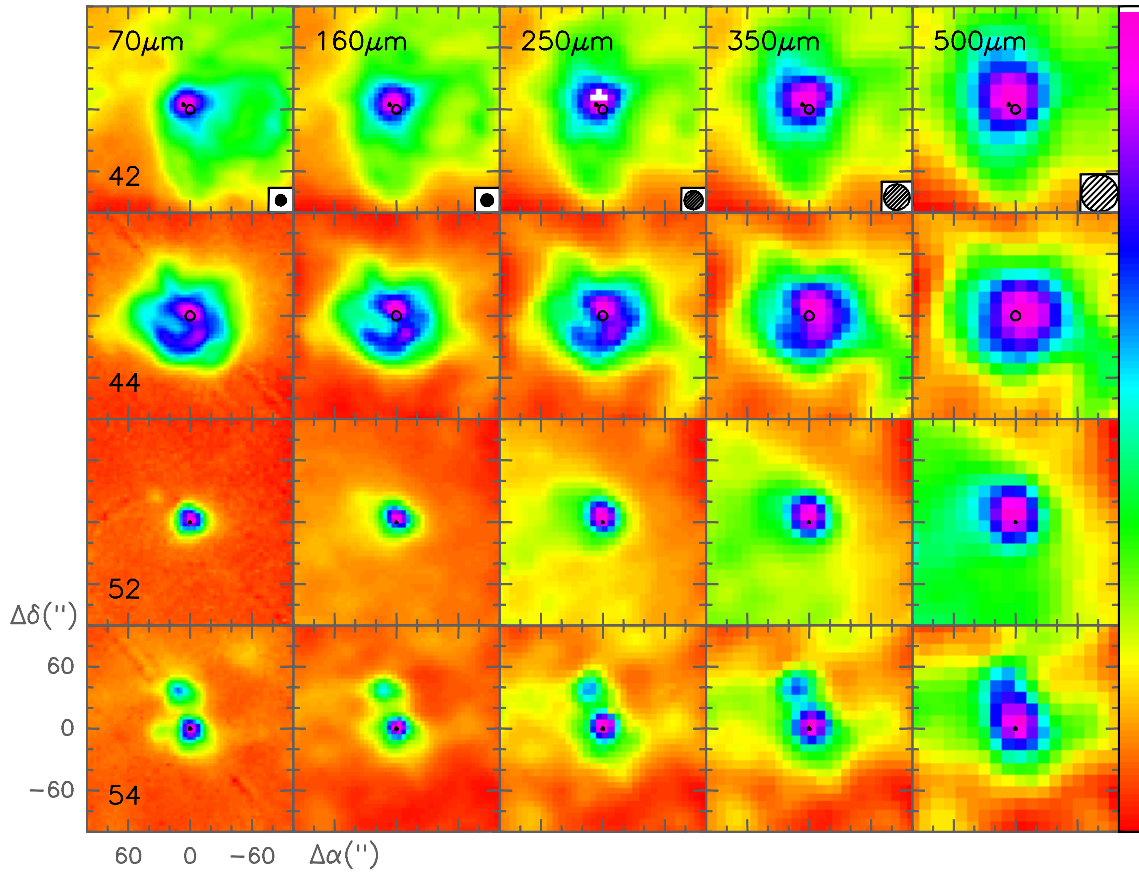


Fig. A.4. continued.

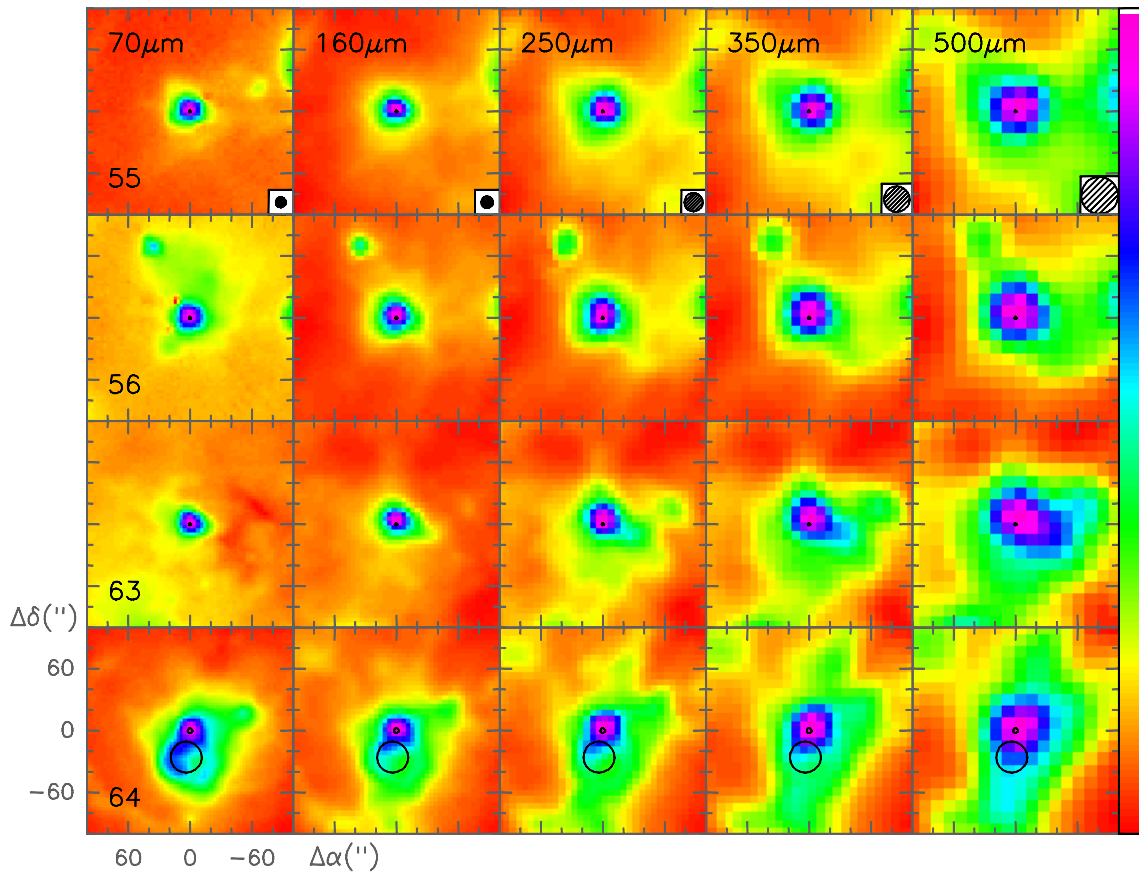


Fig. A.4. continued.

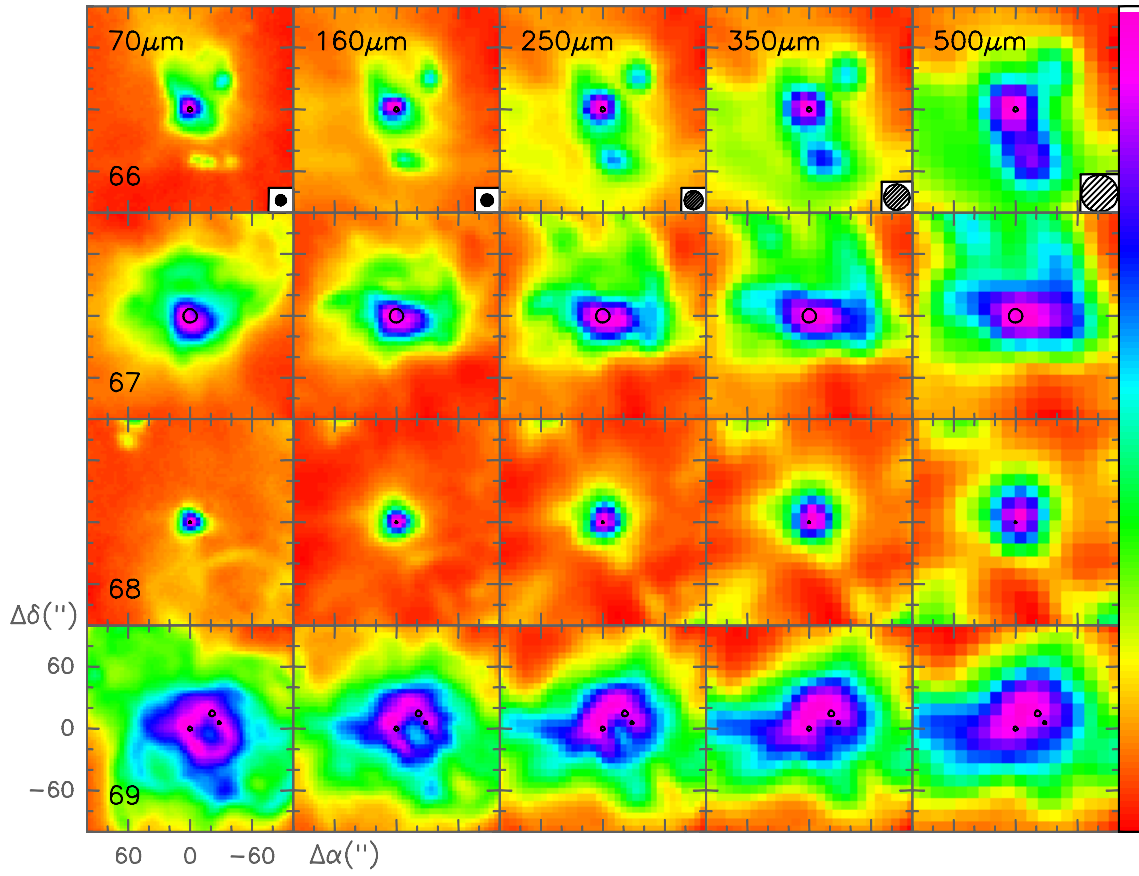


Fig. A.4. continued.

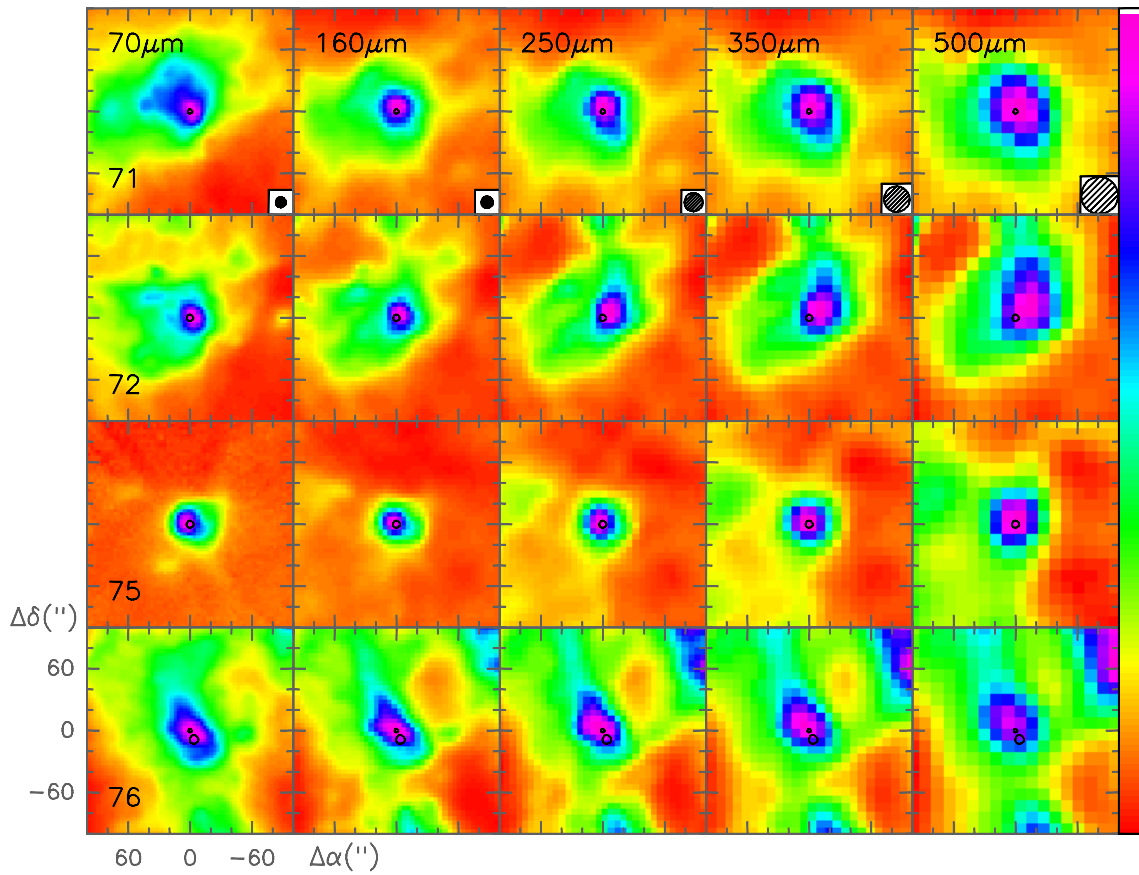


Fig. A.4. continued.

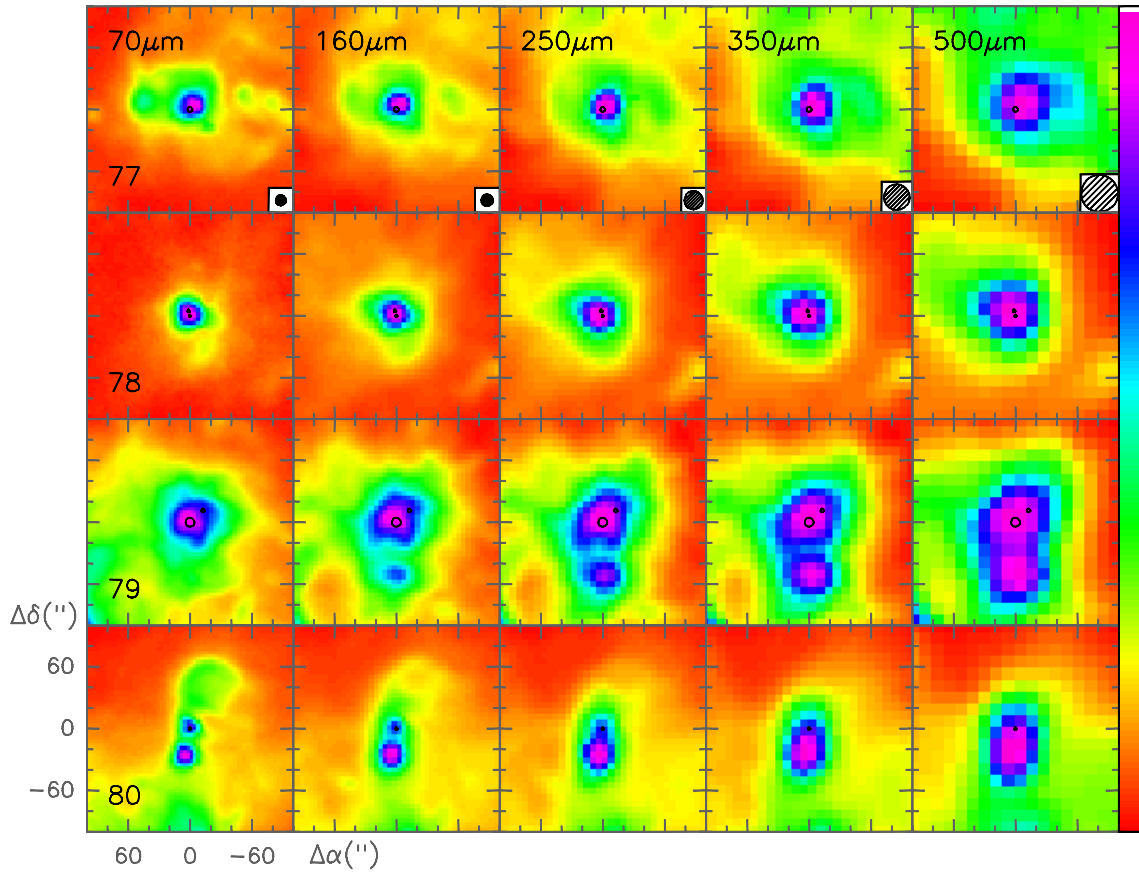


Fig. A.4. continued.

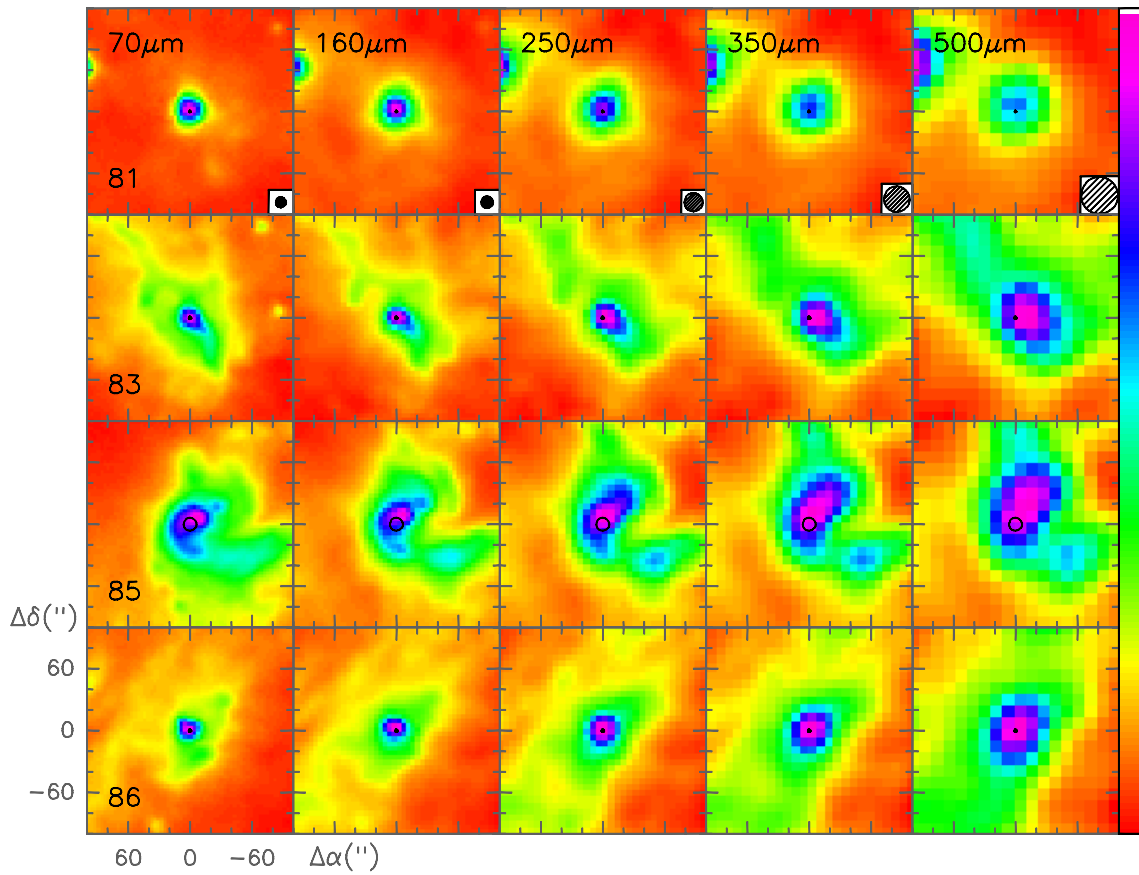


Fig. A.4. continued.

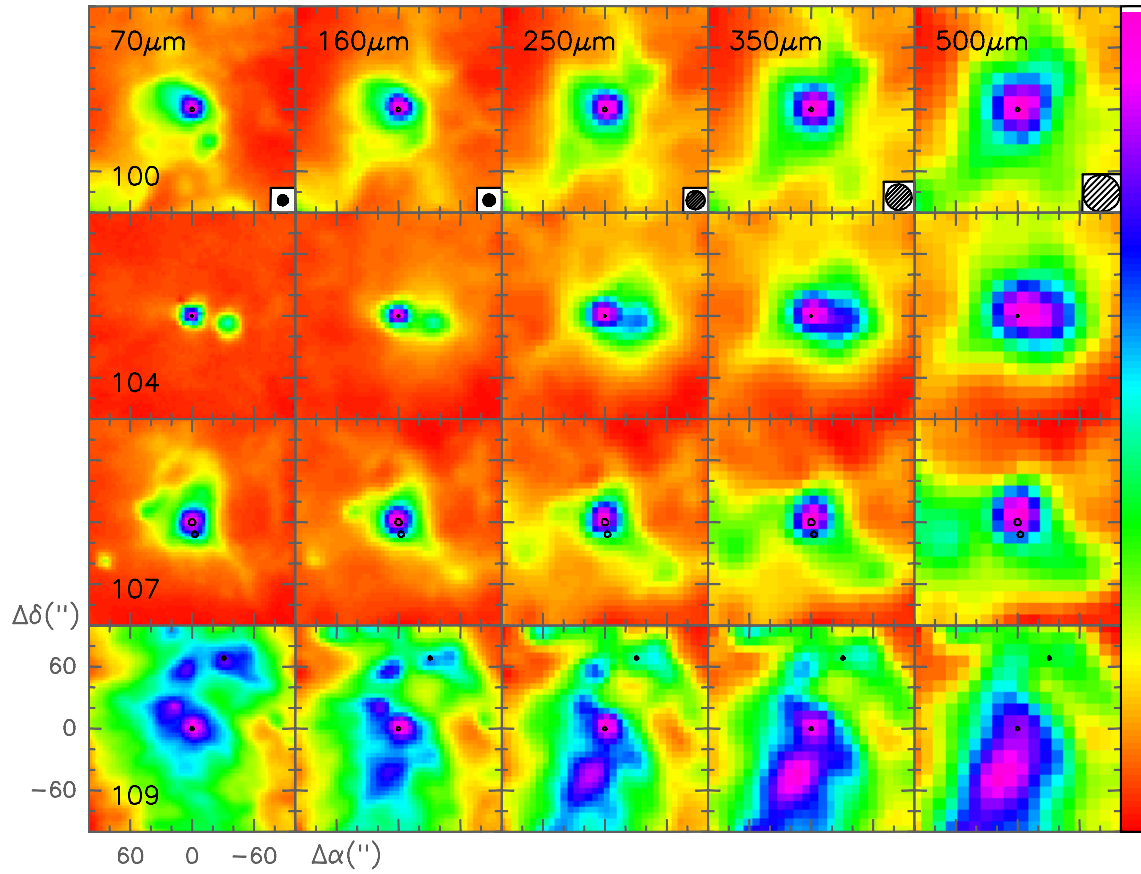


Fig. A.4. continued.

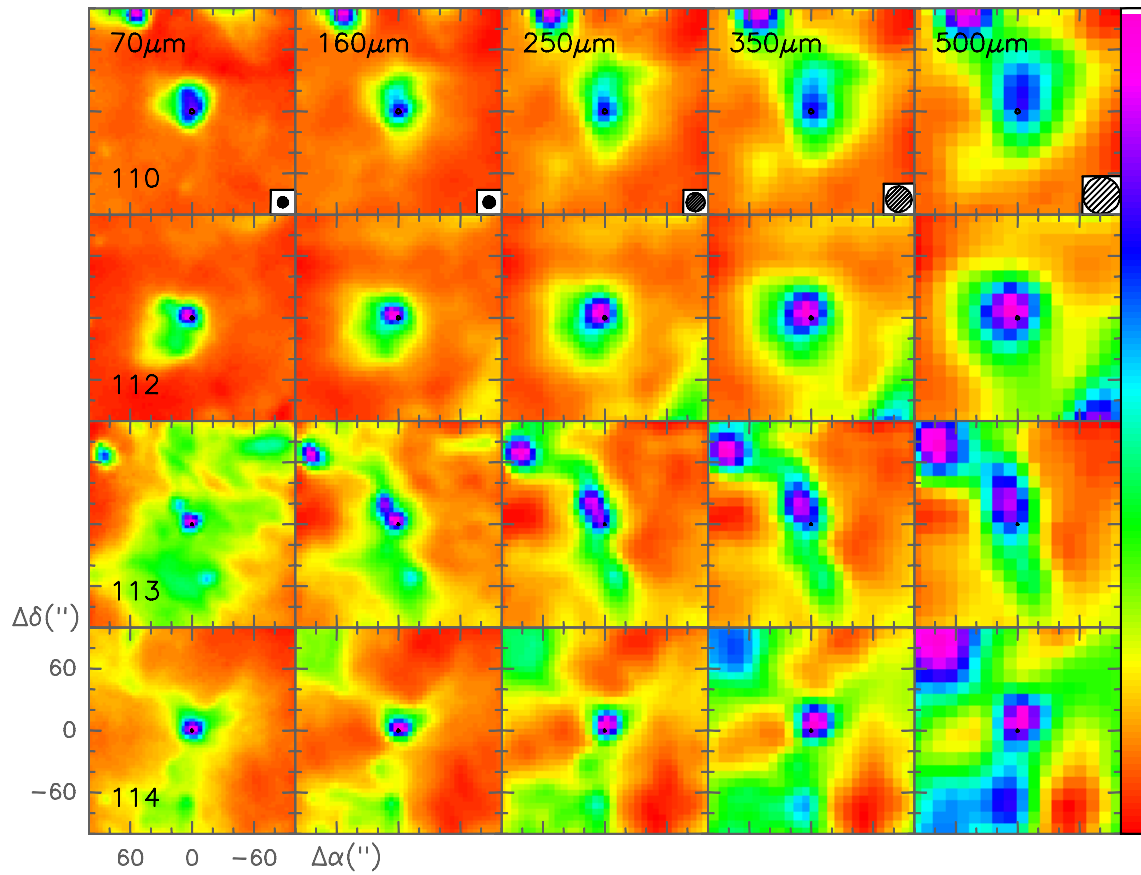


Fig. A.4. continued.

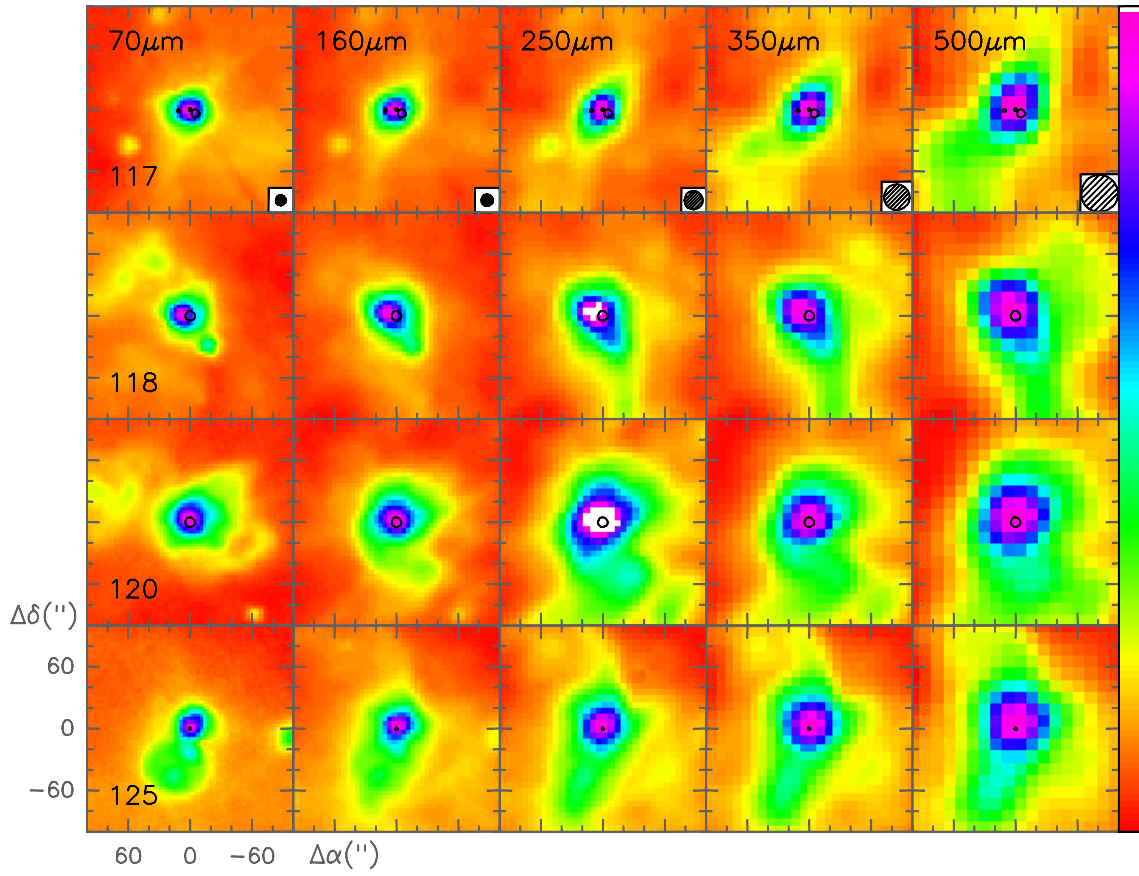


Fig. A.4. continued.

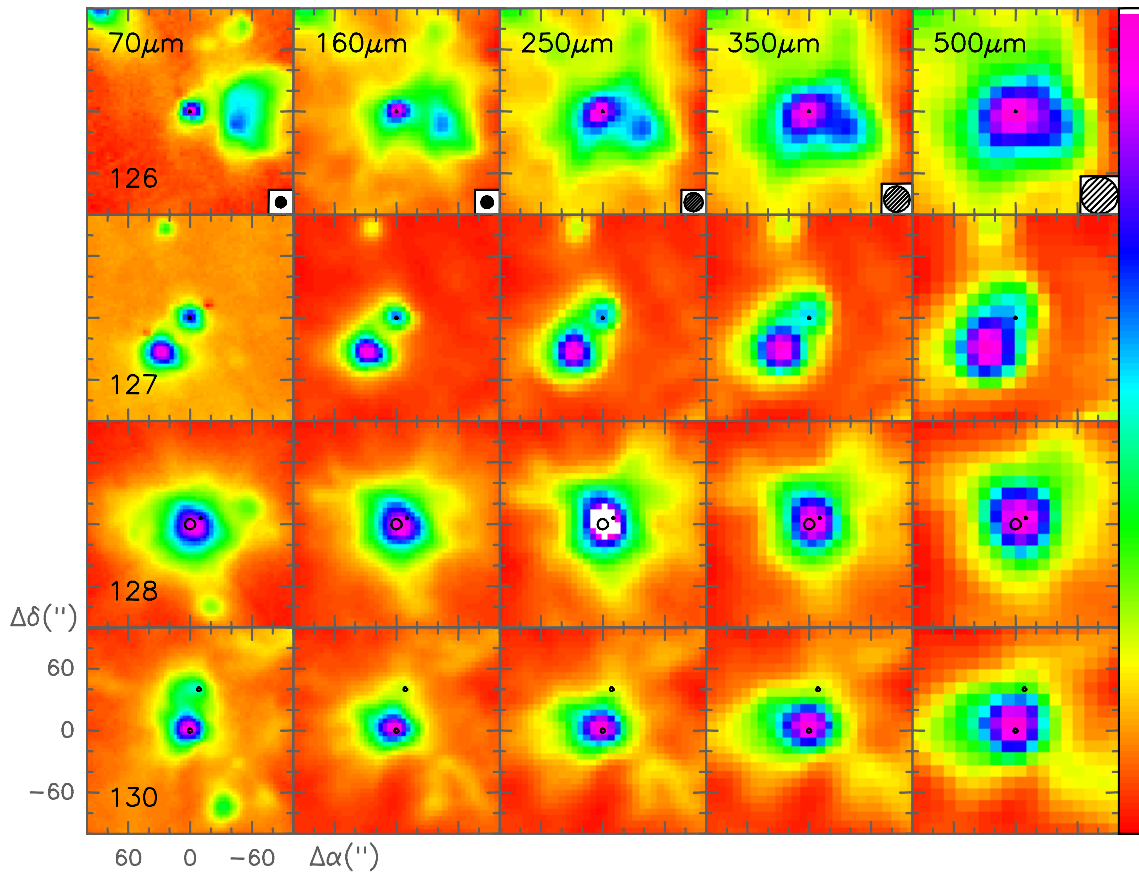


Fig. A.4. continued.

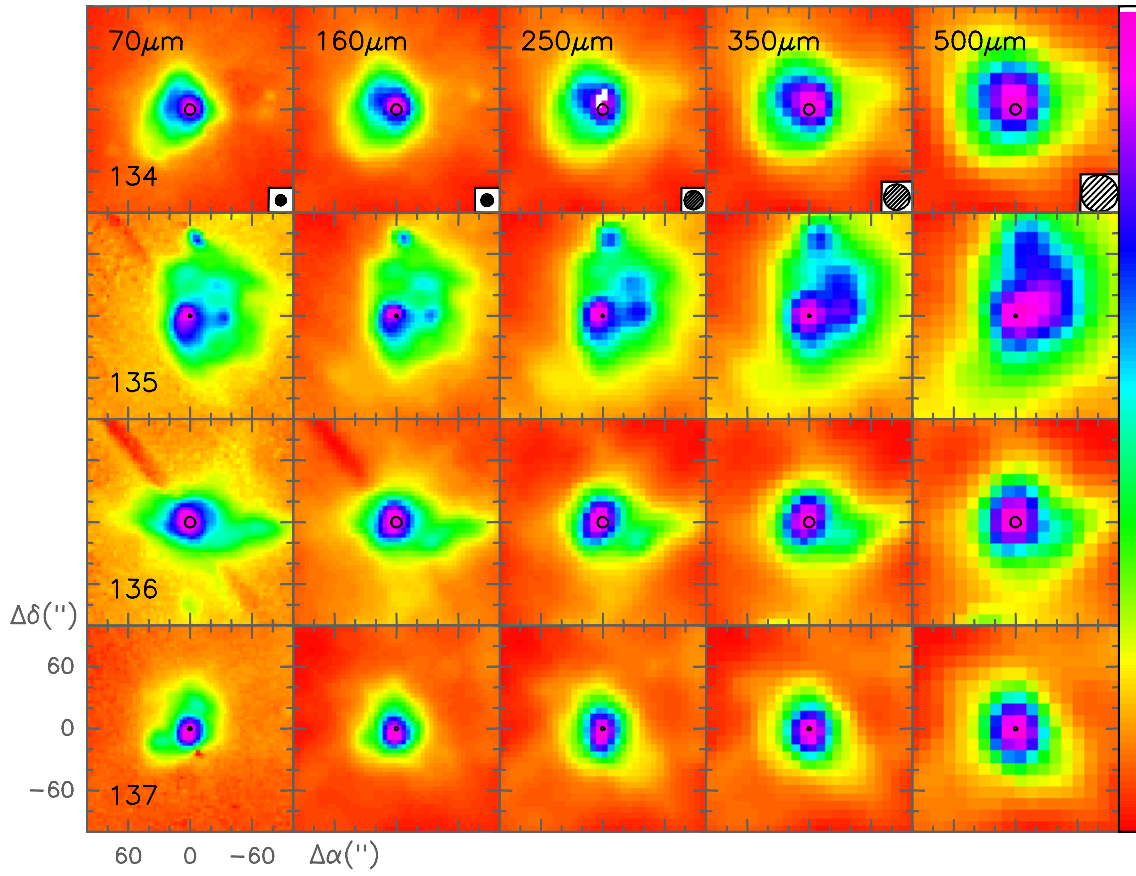


Fig. A.4. continued.

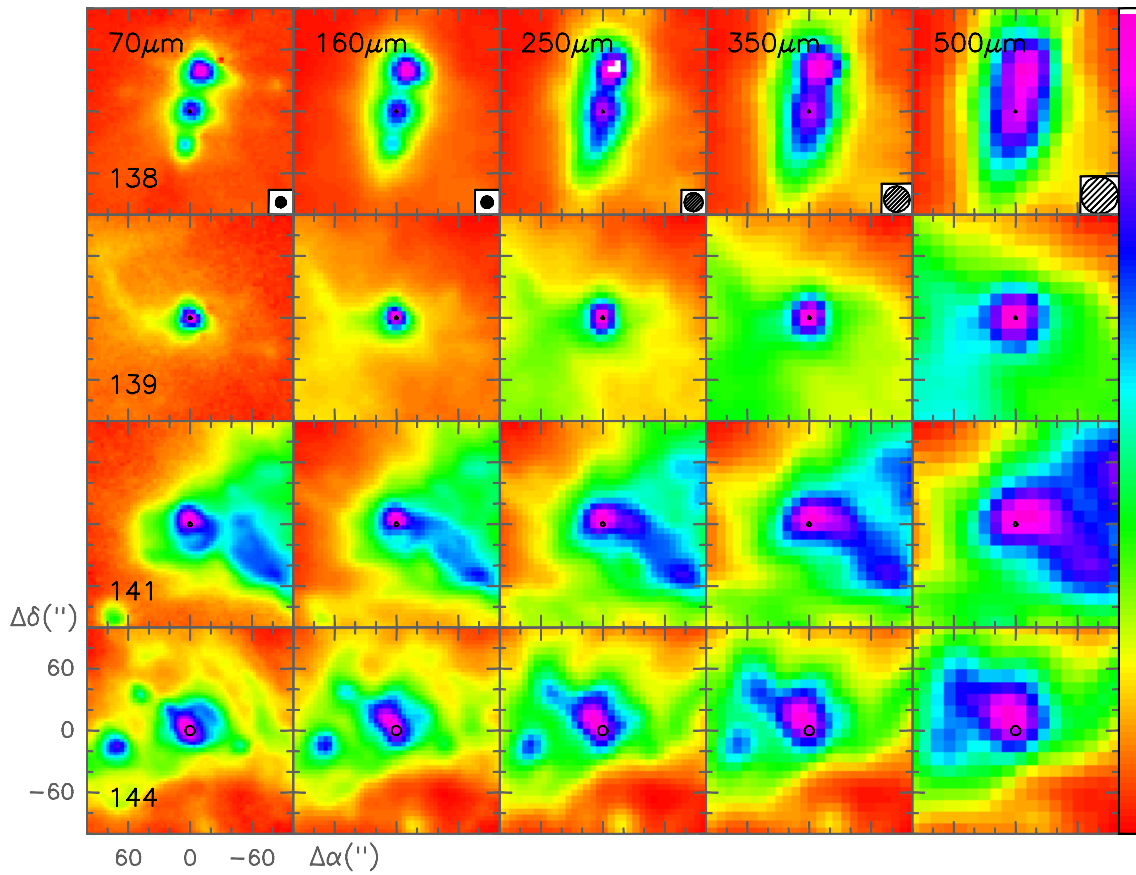


Fig. A.4. continued.

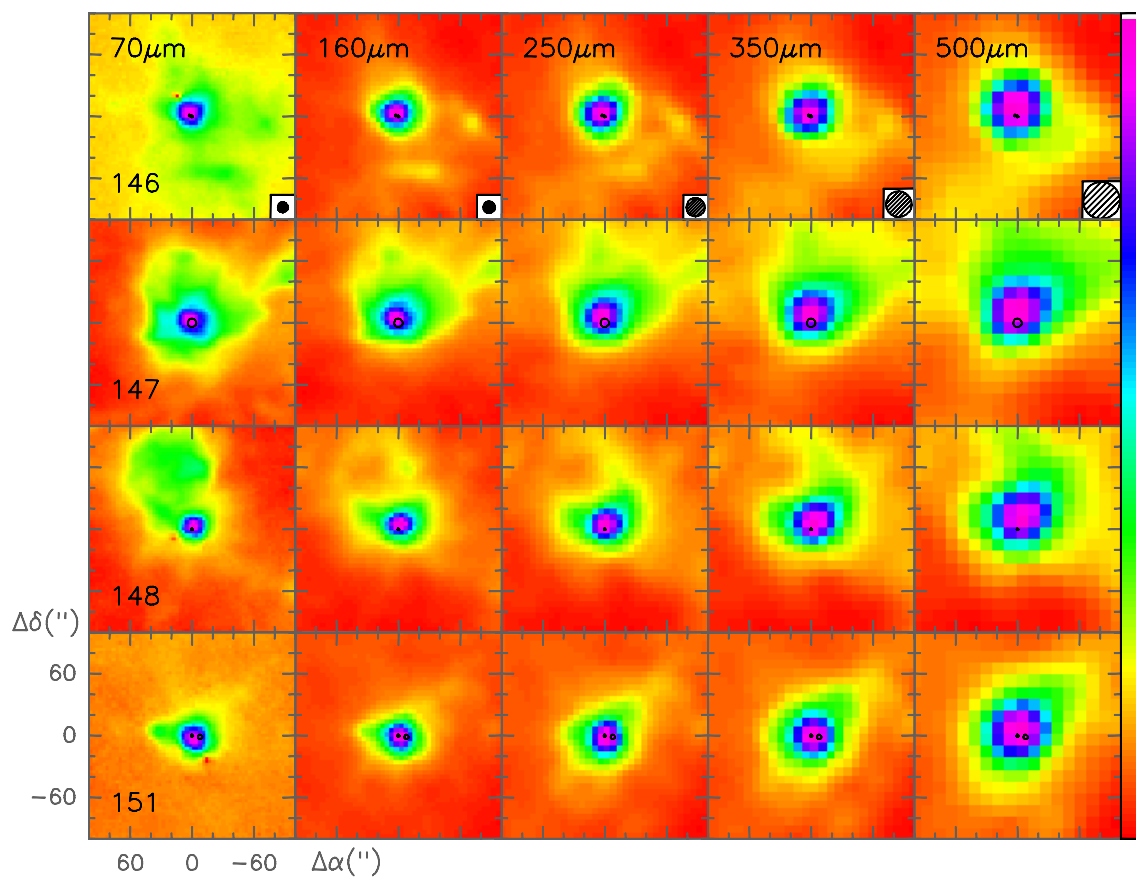


Fig. A.4. continued.

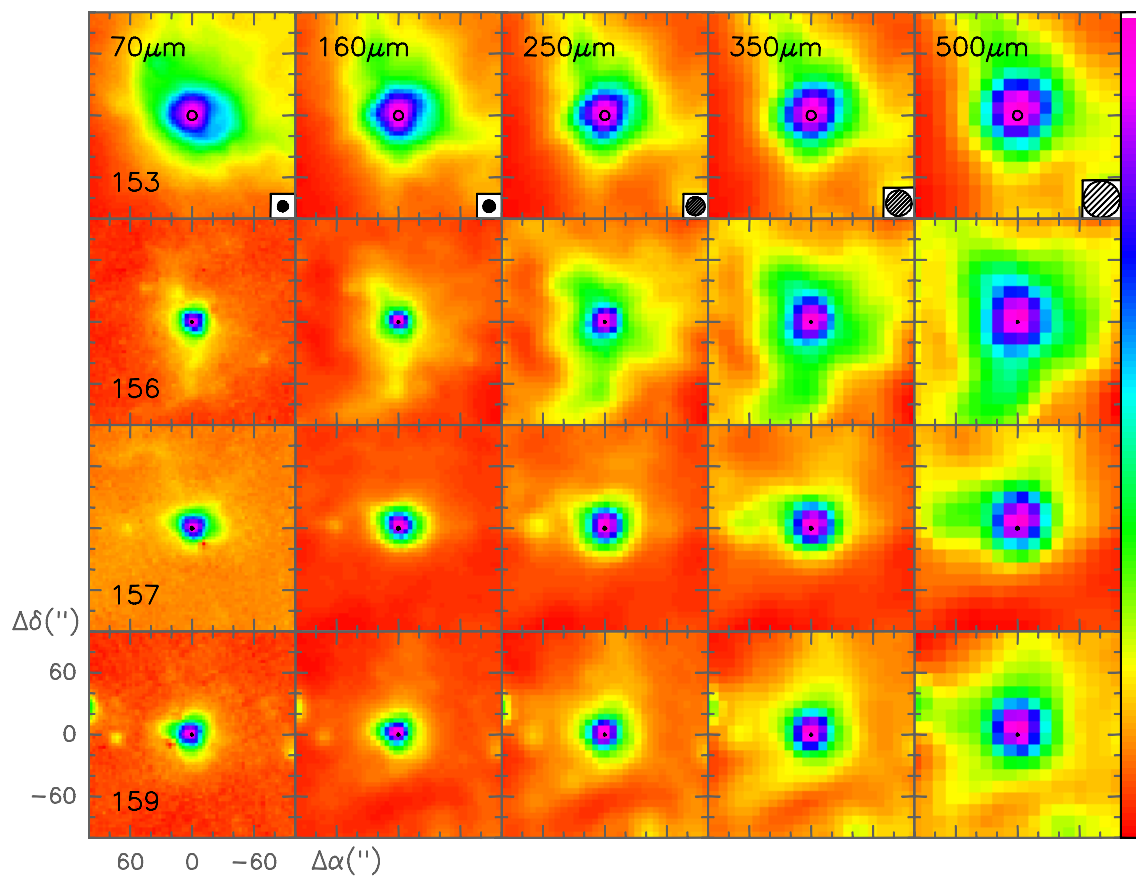


Fig. A.4. continued.

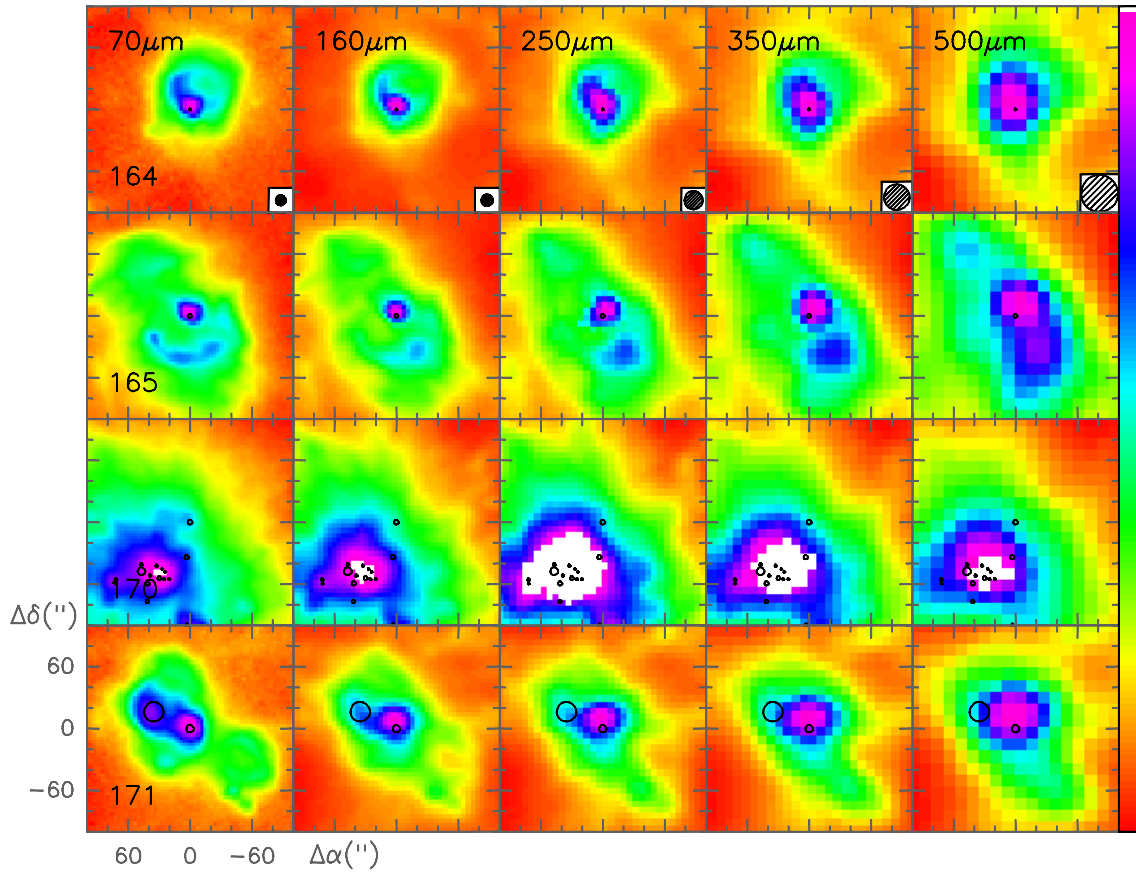


Fig. A.4. continued.

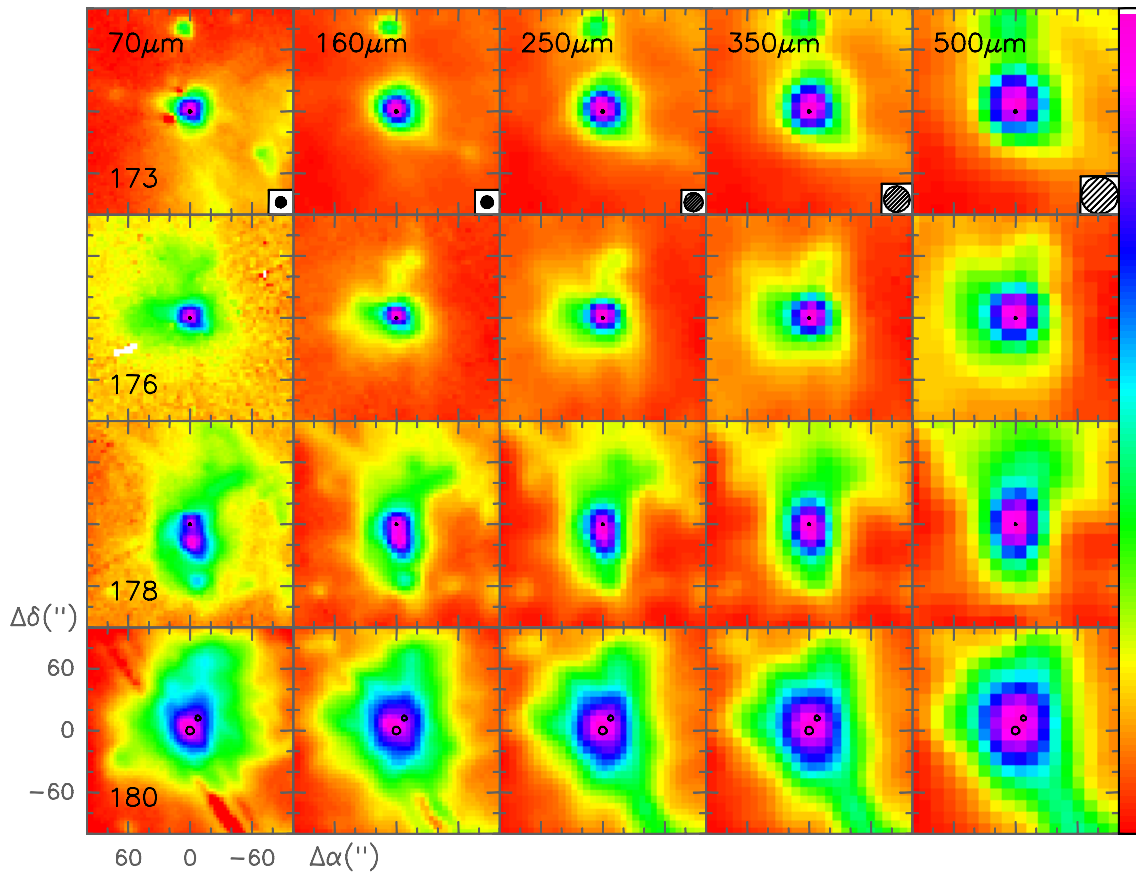


Fig. A.4. continued.

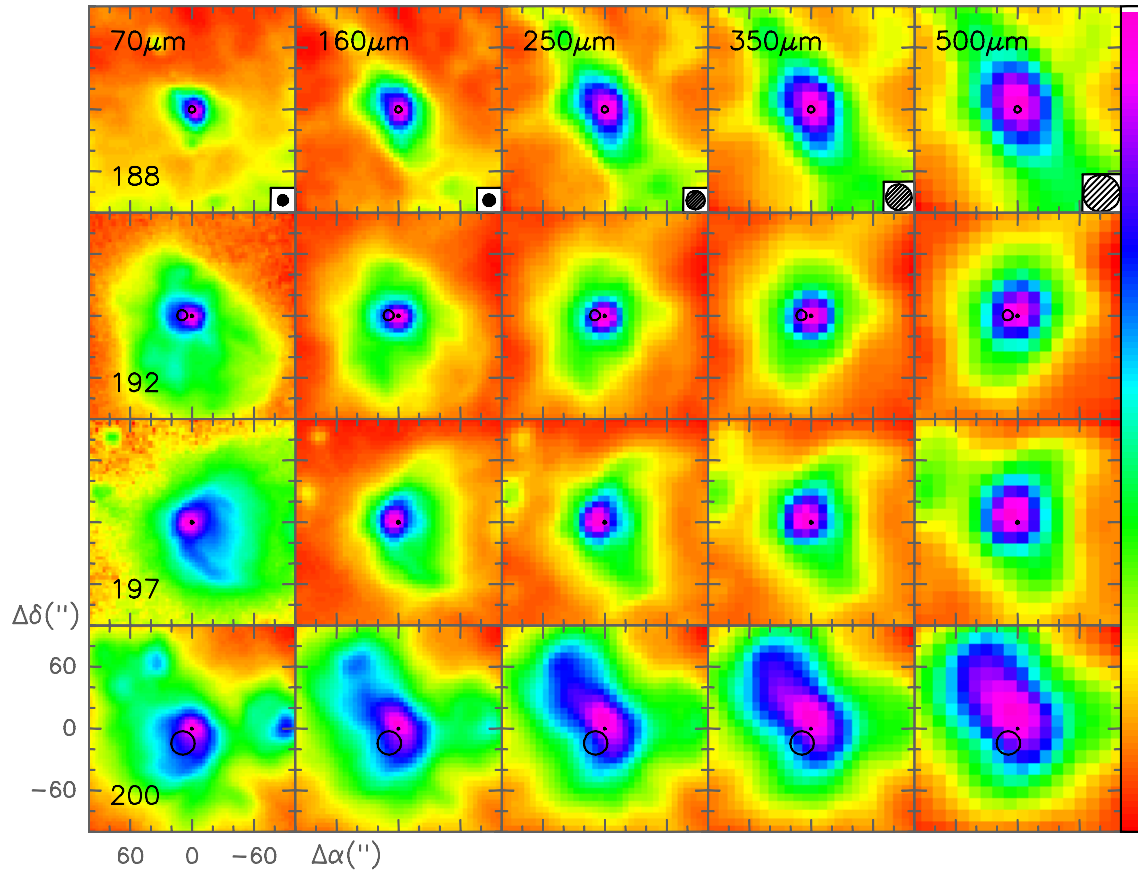


Fig. A.4. continued.

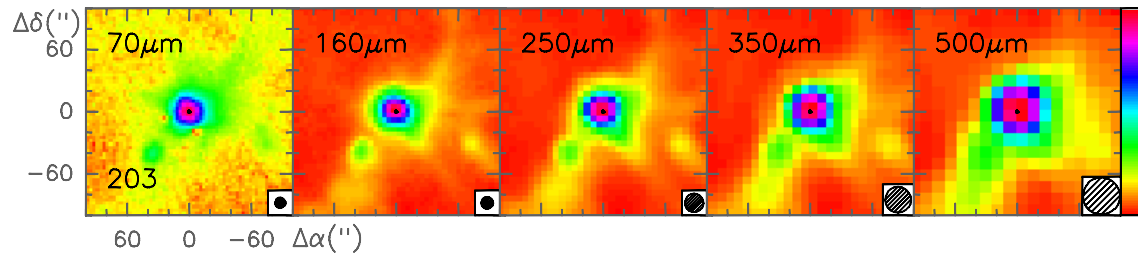


Fig. A.4. continued.

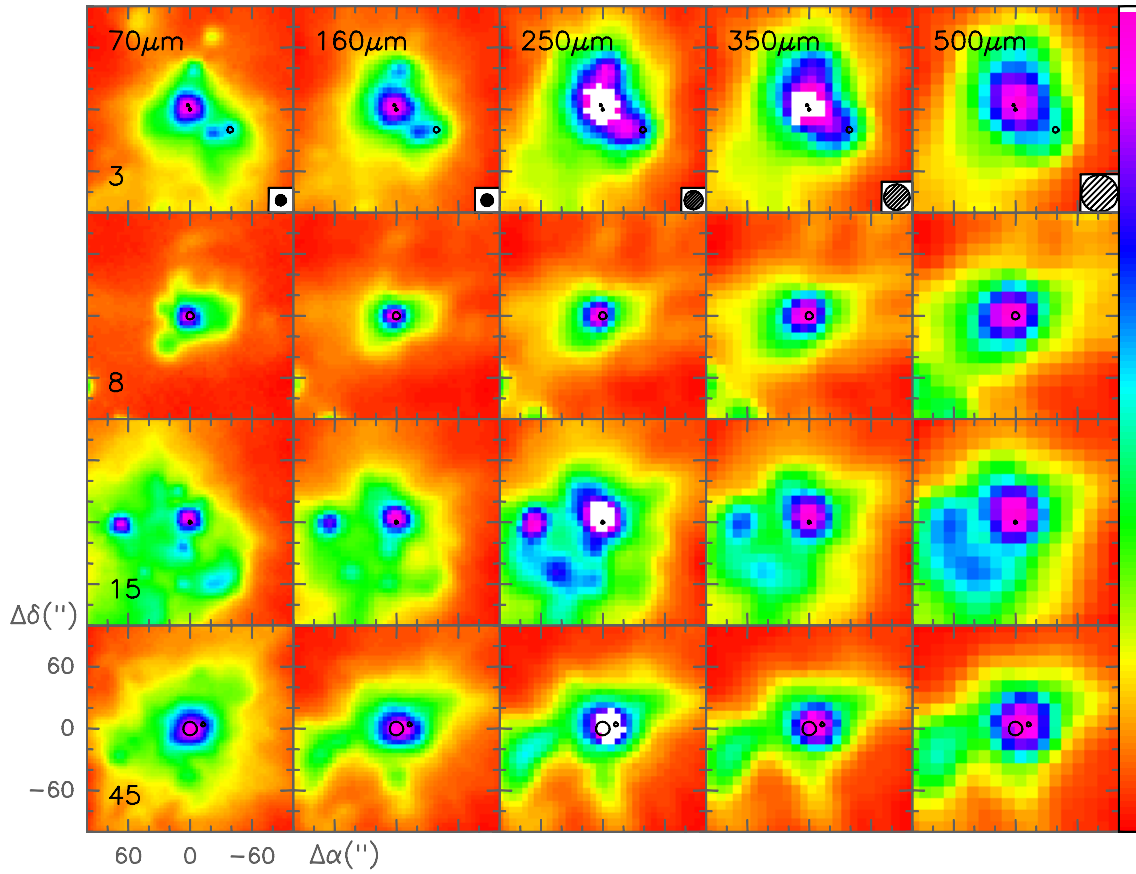


Fig. A.5. Same as Fig. A.2 for the sources lying below the cluster region in Fig. 5.

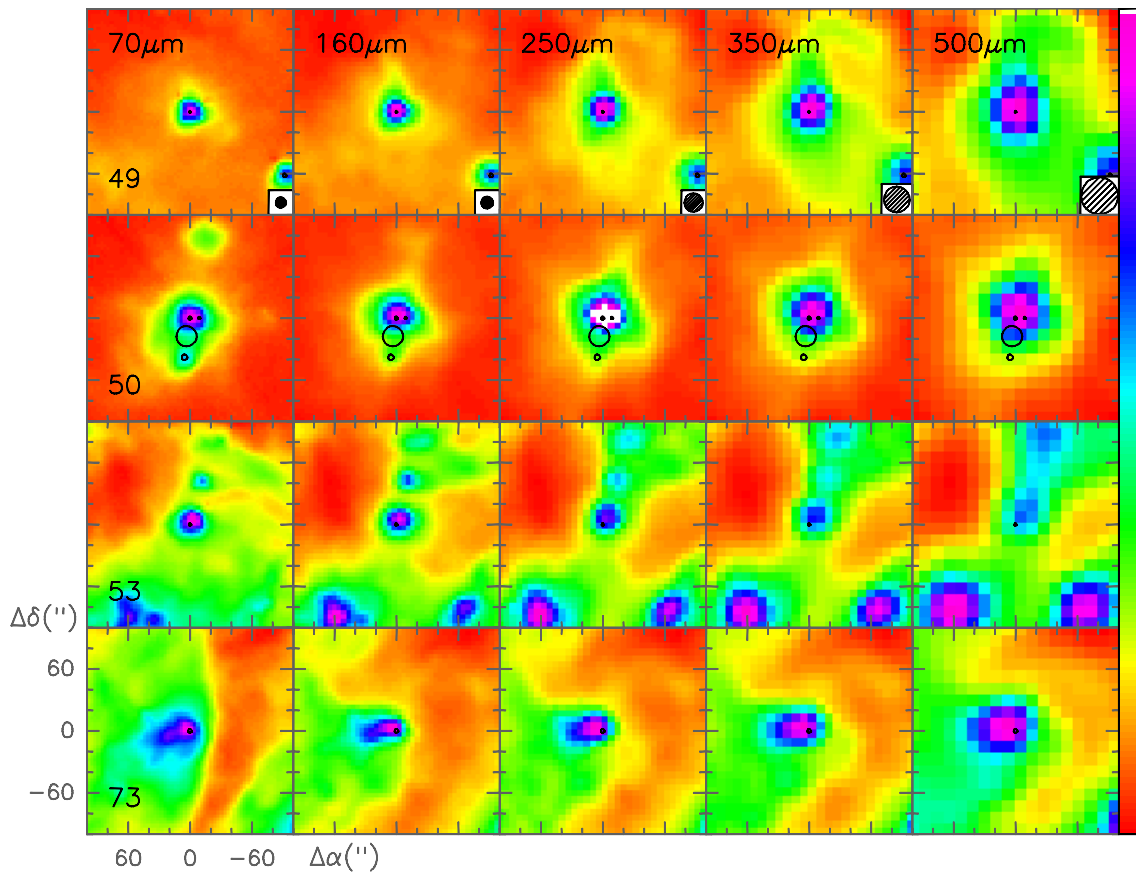


Fig. A.5. continued.

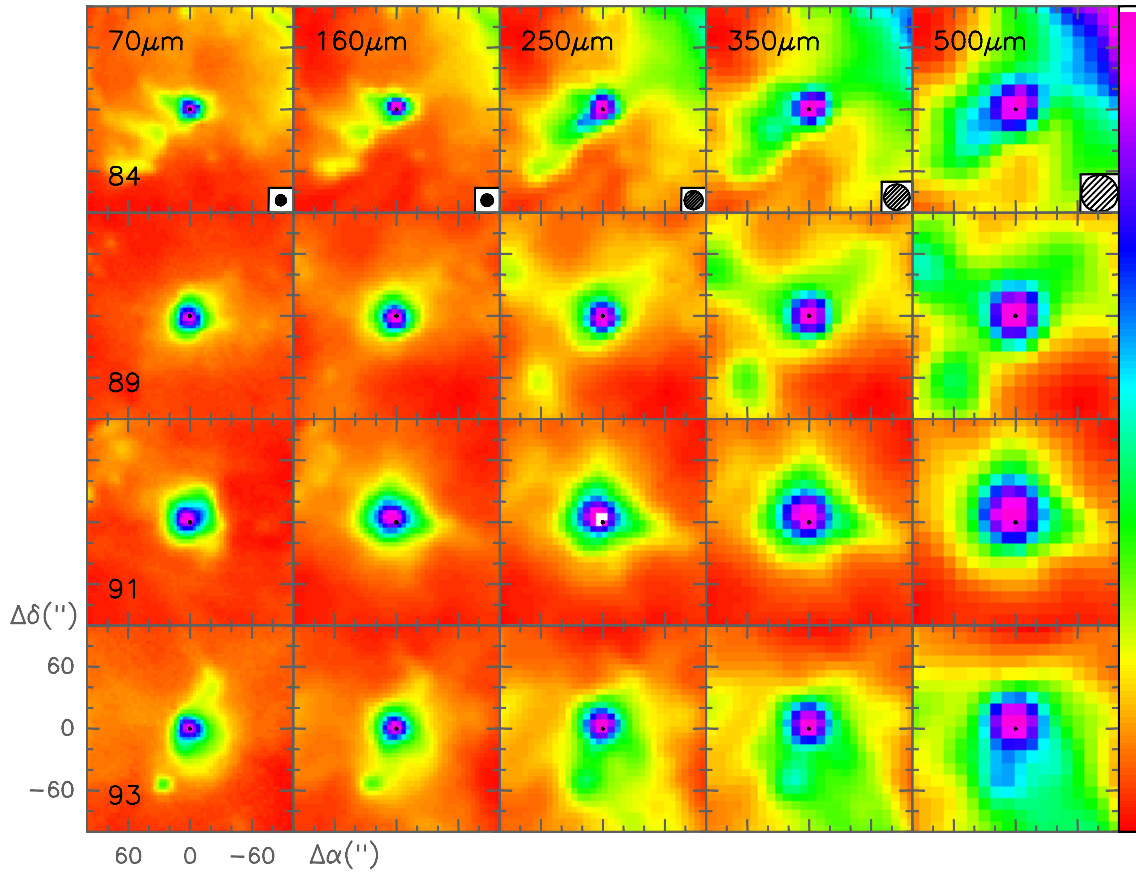


Fig. A.5. continued.

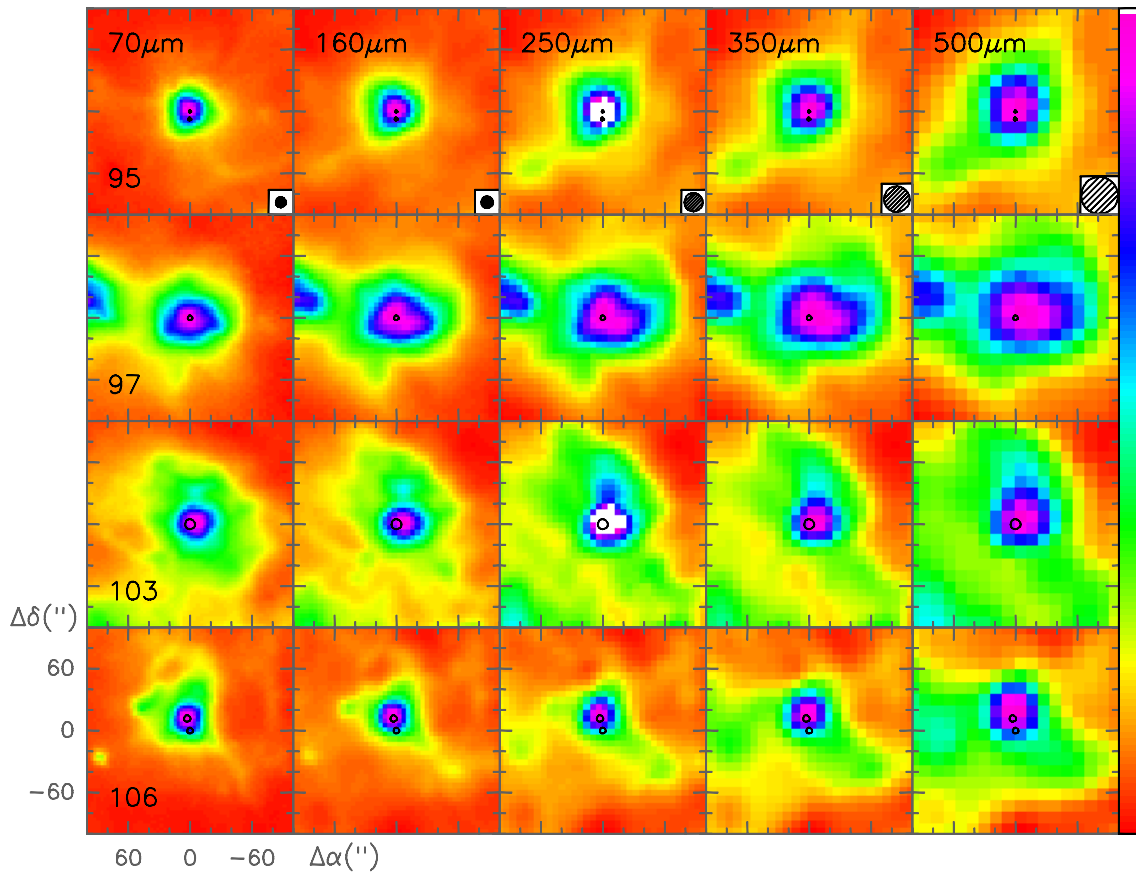


Fig. A.5. continued.

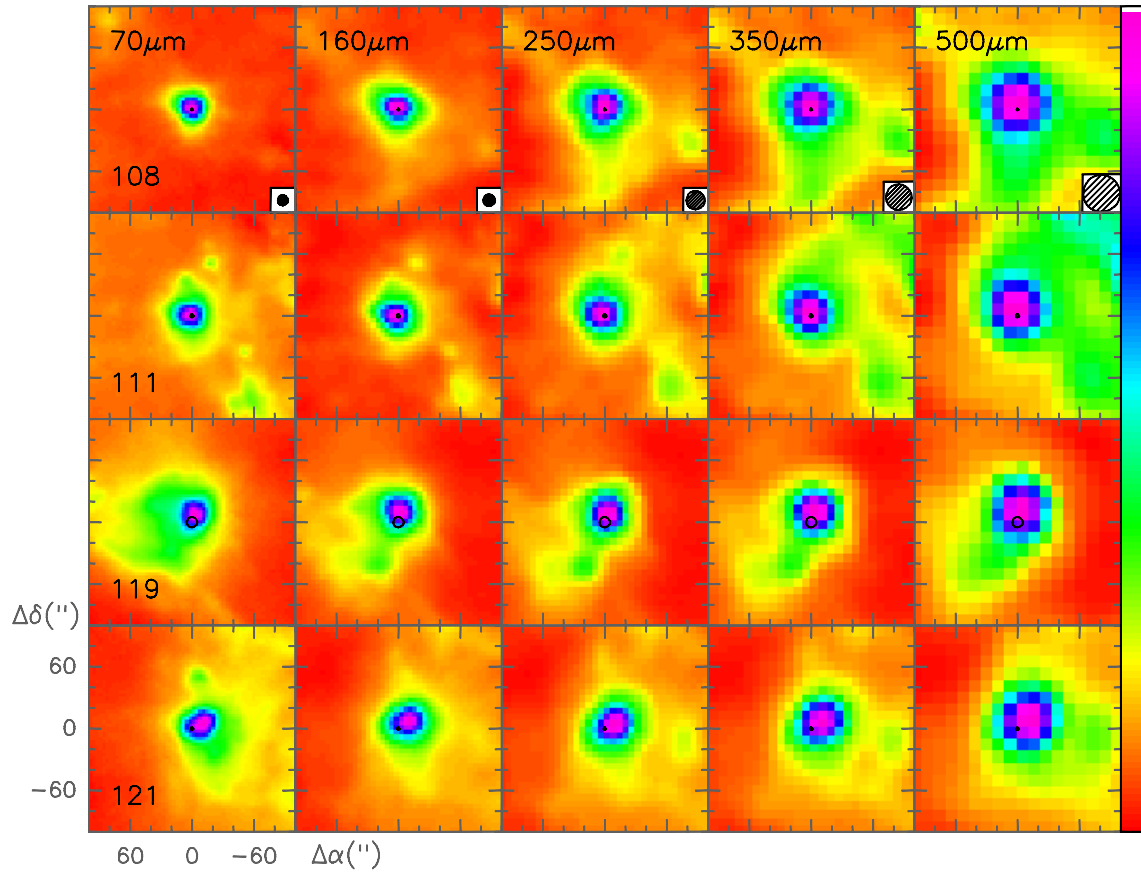


Fig. A.5. continued.

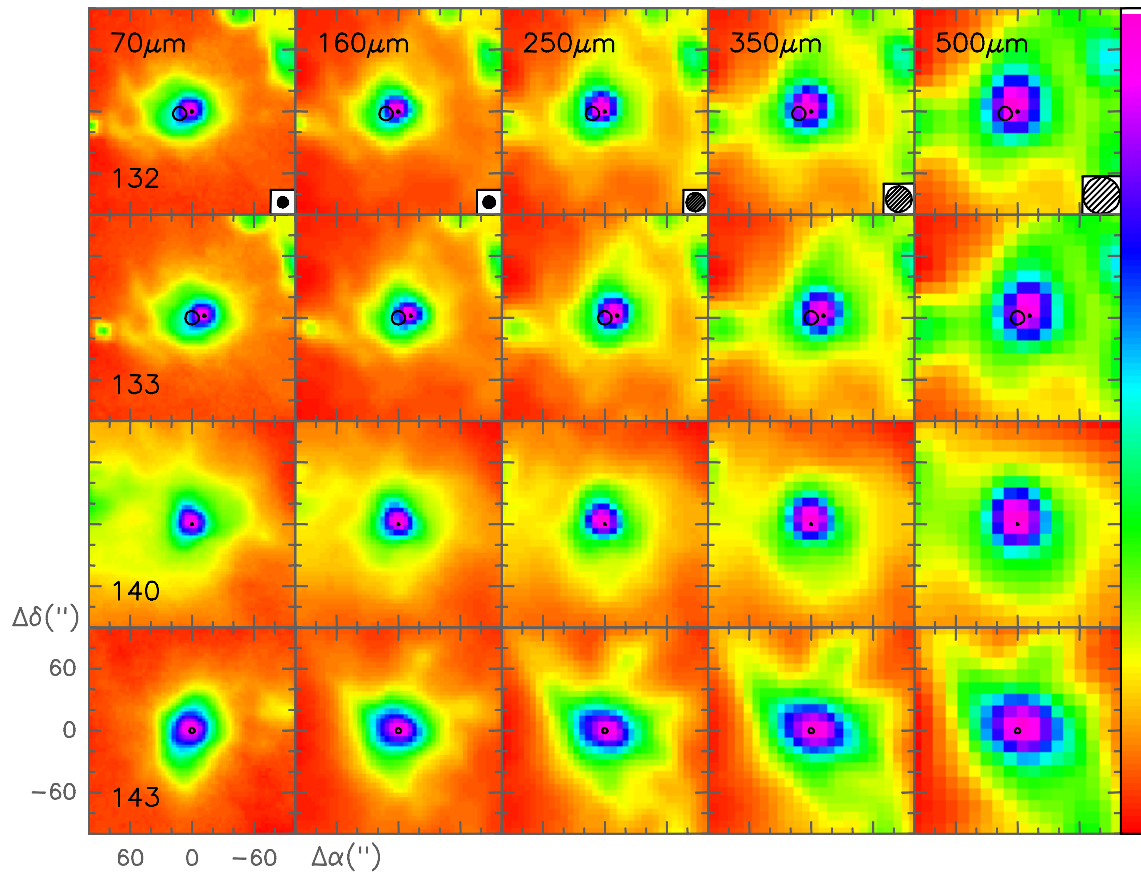


Fig. A.5. continued.

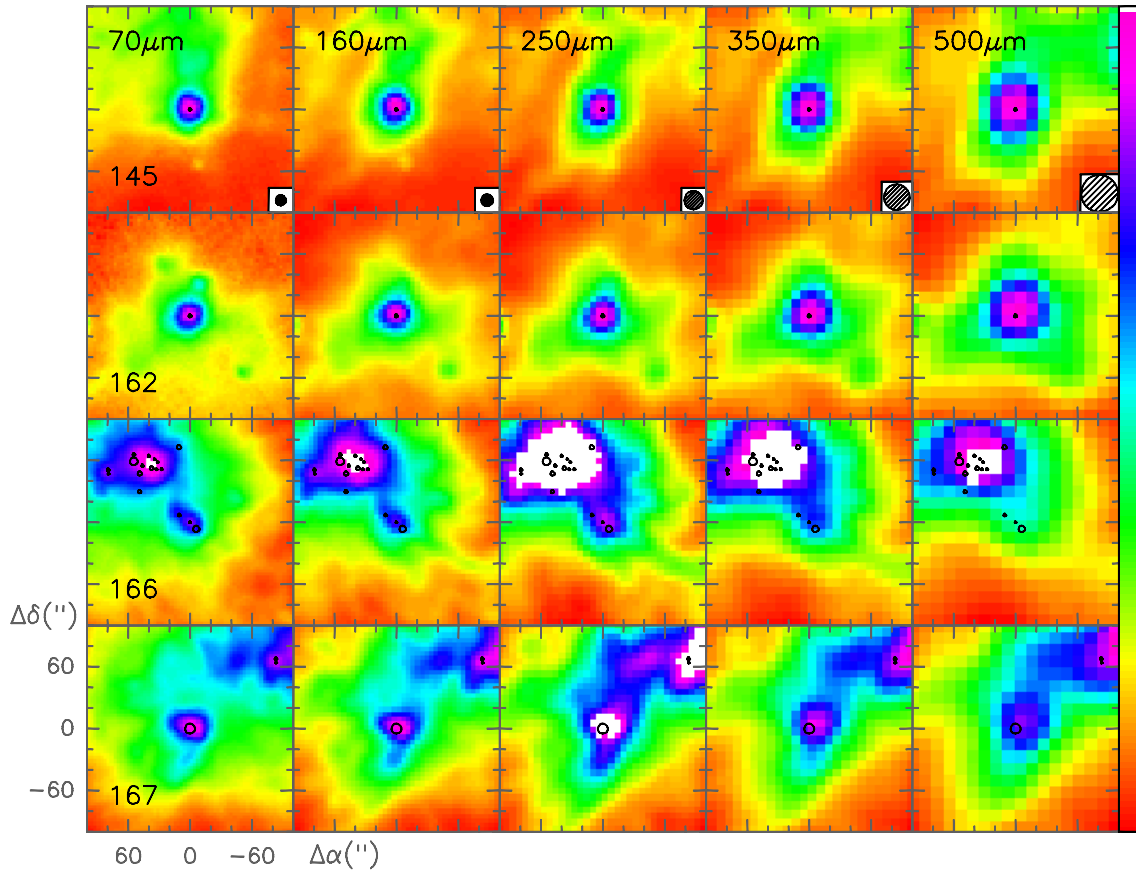


Fig. A.5. continued.

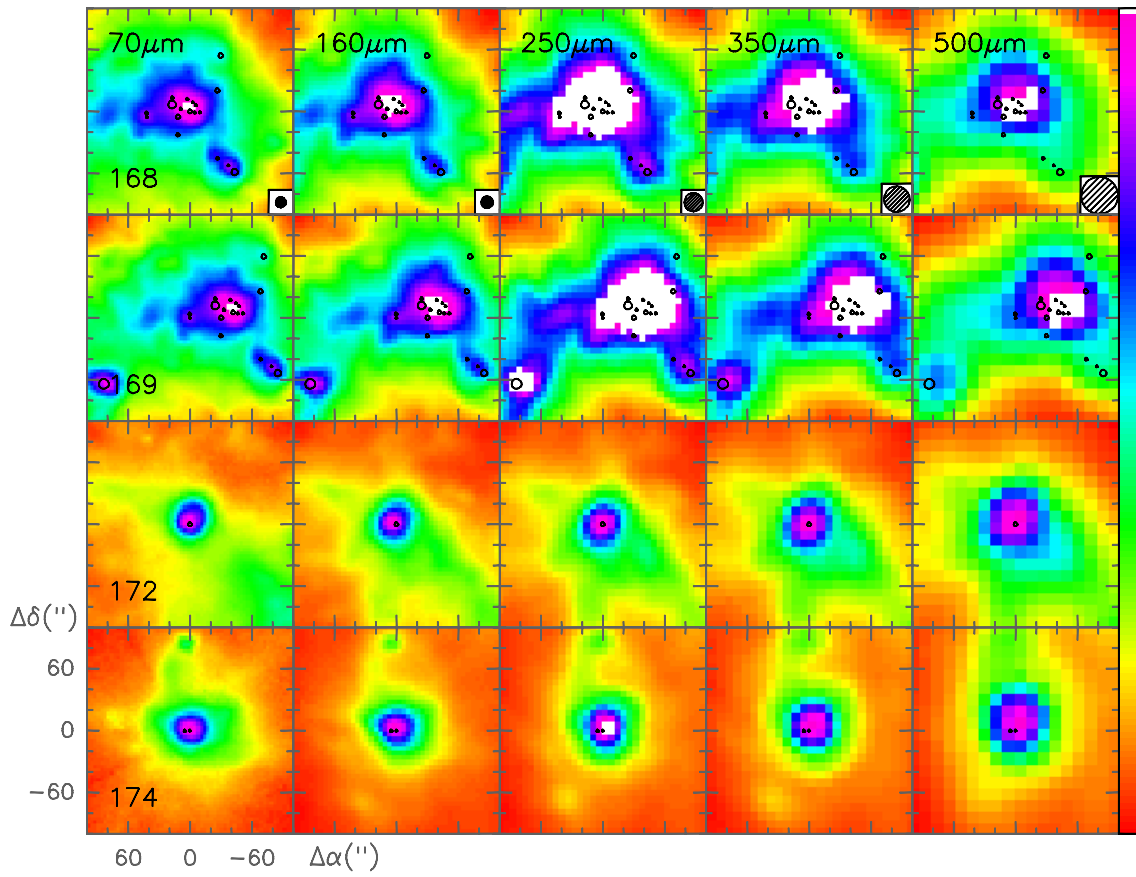


Fig. A.5. continued.

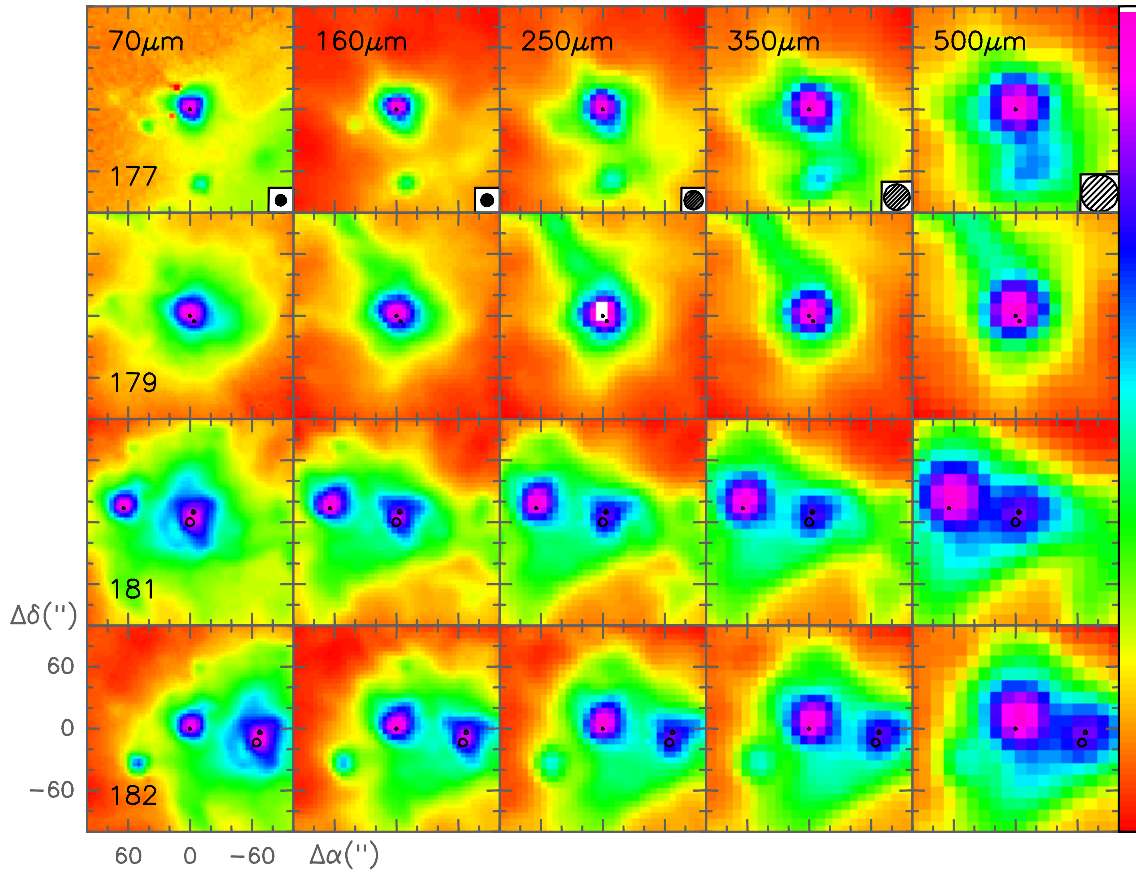


Fig. A.5. continued.

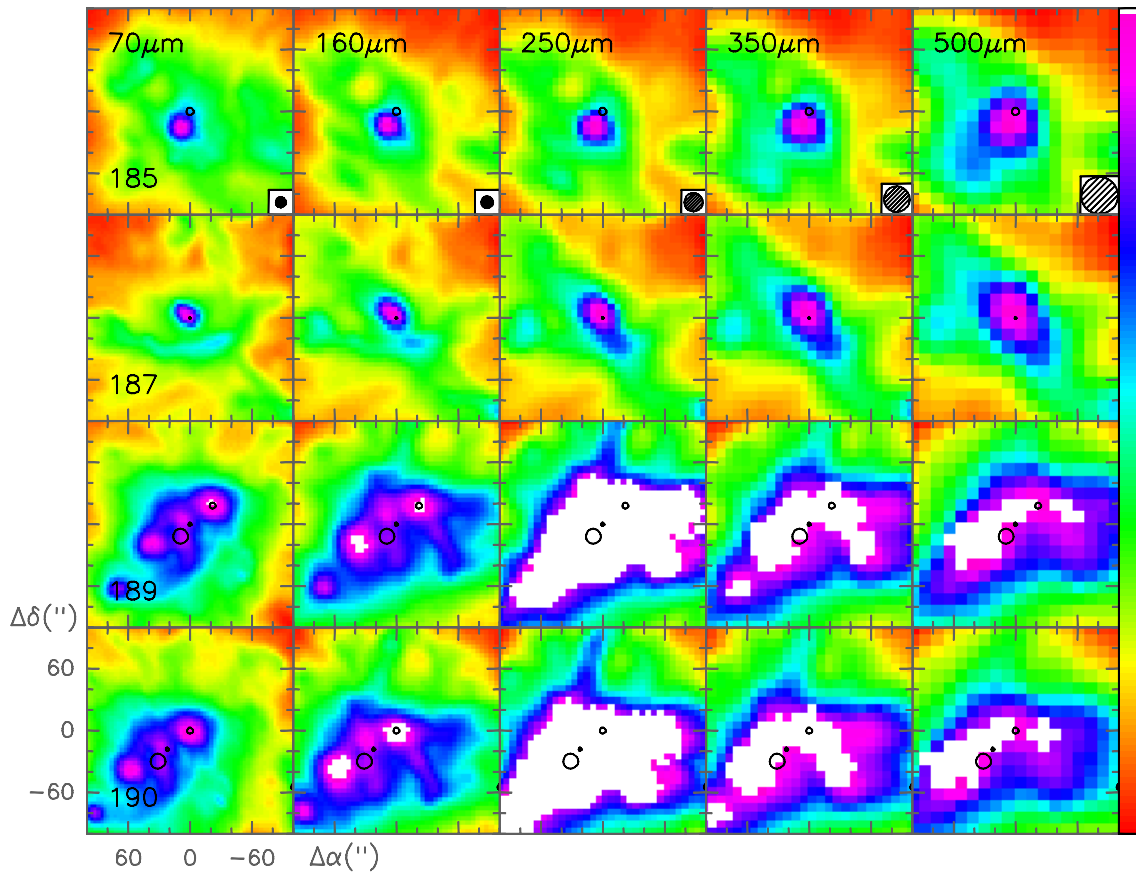


Fig. A.5. continued.

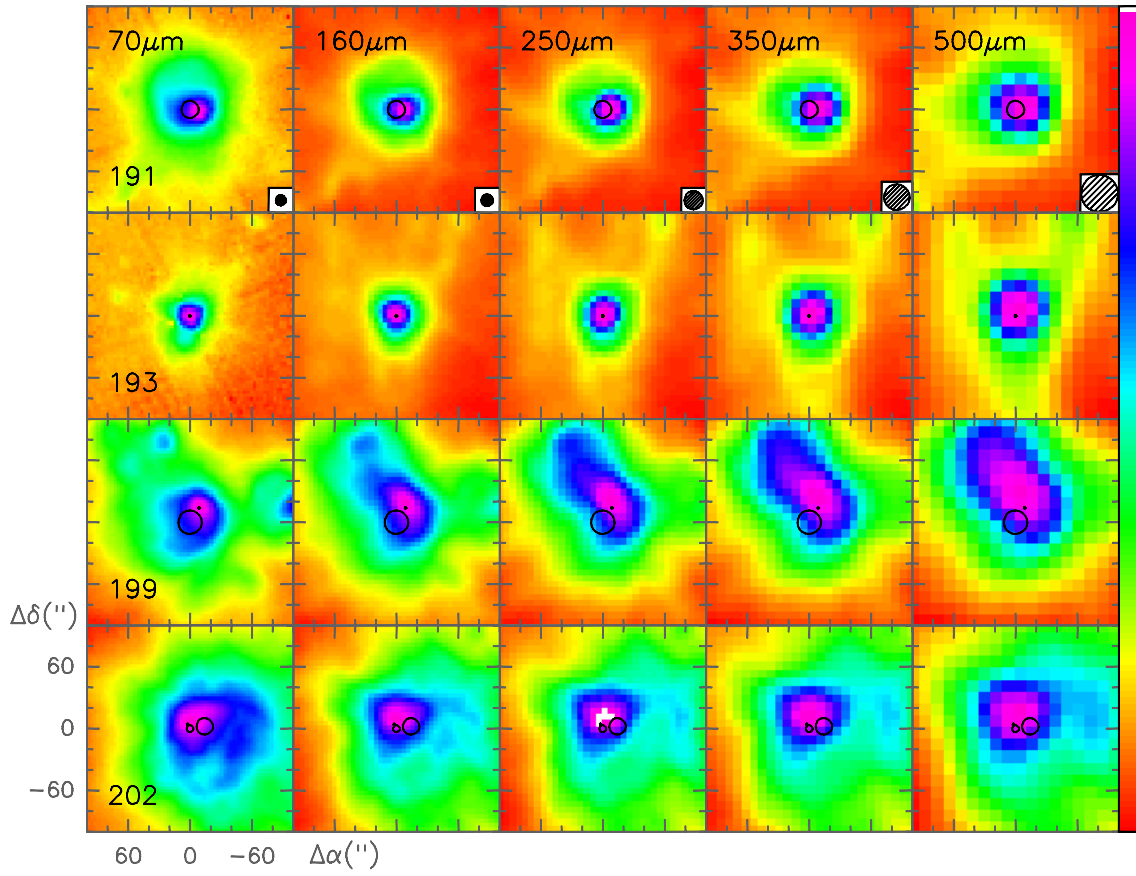


Fig. A.5. continued.

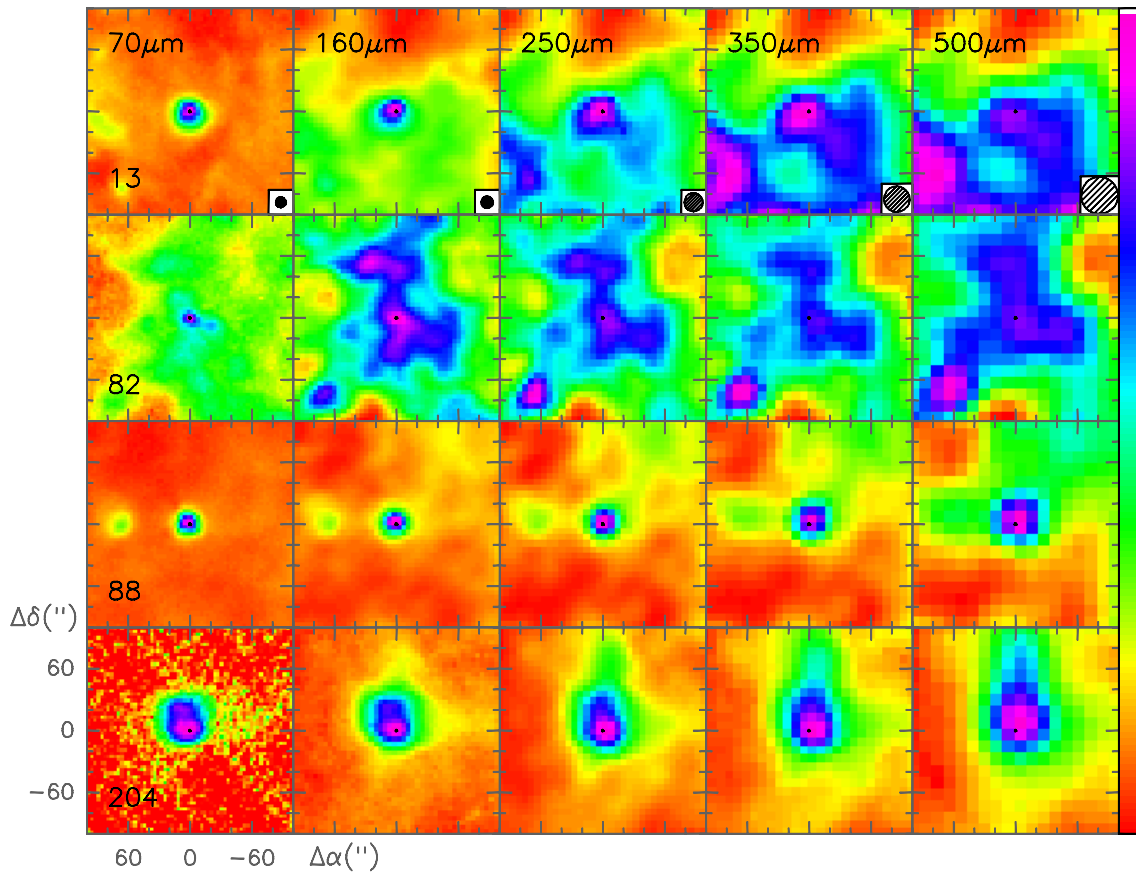


Fig. A.6. Same as Fig. A.2 for the sources without distance estimates.